UNIVERSITA' DEGLI STUDI DI FIRENZE
Dipartimento di Ingegneria Civile
Studi e Ricerche

3

Luca Solari

TOPICS IN FLUVIAL AND LAGOON MORPHODYNAMICS

Firenze University Press

UNIVERSITÀ DEGLI STUDI DI FIRENZE
Dipartimento di Ingegneria Civile
Studi e Ricerche

3

Luca Solari

TOPICS IN FLUVIAL AND LAGOON MORPHODYNAMICS

Firenze University Press

UNIVERSITÀ DEGLI STUDI DI FIRENZE
Dipartimento di Ingegneria Civile
Studi e Ricerche

3

Luca Solari

TOPICS IN FLUVIAL AND LAGOON MORPHODYNAMICS

Firenze University Press
2001

Topics in fluvial and lagoon morphodynamics / Luca Solari. – Dati e programmi per computer. - Firenze : Firenze university press, 2001.
(Studi e ricerche / Università degli studi di Firenze, Dipartimento di ingegneria civile, 3)
Modalità di accesso:
http://fulltext.casalini.it/is.asp?ISBN=8884530091 -
Tit. della schermata del titolo. – Pubbl. anche su supporto cartaceo.

ISBN 88-8453-009-1

551.4708 (ed. 20)

Firenze University Press
Borgo Albizi, 28
50122 Firenze
Italy
http://www.unifi.it/e-press
email: e-press@unifi.it

Contents

List of Figures

List of Tables

Ma prima farò alcuna esperienzia avanti ch'io più oltre proceda, perché mia intenzione è allegare prima l'esperienzia e poi colla ragione dimostrare perché tale esperienzia è costretta in tal modo ad operare. E questa è la vera regola come li speculatori delli effetti naturali hanno a procedere, e ancora che la natura cominci dalla ragione e termini nella sperienzia, a noi bisogna seguitare in contrario, cioè cominciando, come di sopra dissi, dalla sperienzia, e con quella investigare la ragione.

(Leonardo da Vinci)

Foreword

In the present book is collected the research activity I have carried out during my PhD at the Department of Environmental Engineering of the University of Genova under the supervision of prof. G. Seminara.

Abstract

The present work consists of two parts. Part one (chapters 1,2,3) concerns tidal morphodynamics, while part two (chapter 4) deals with a topic of fluvial morphodynamics.
In chapter 1 we outline the main morphological features and physical processes displayed by tide dominated estuaries and tidal channels.
In chapter 2 we develop a theoretical model devoted to investigate flow field pattern and bed topography in weakly meandering tidal channels. Such model will then be set at the basis of a planimetric instability analysis of the type developed for river meanders (Blondeaux & Seminara, 1985). Results will be discussed in the light of new observational evidence of meanders within different tidal environments.
In chapter 3 we present an experimental investigation on the hydrodynamic processes occurring during the propagation of a tidal wave in a tidal channel. Some preliminary observations regarding the interaction between the cohesionless bottom and the tidal current will also be presented. Results will be discussed and compared with the analysis recently developed by Lanzoni & Seminara (2000). We will also discuss scaling rules to insure similarity in mobile bed models of tidal flow over a cohesionless bottom. Such analysis leads to a set of similarity rules which will be applied to the present model.
In chapter 4 we present a theoretical model of bedload transport on arbitrarily sloping beds at low values of Shields parameter. Such problem is of great practical interest as most phenomena in river morphodynamics involve the motion of grains on non planar beds. The analysis will investigate the consequences of the constraint imposed by Bagnold's hypothesis when the bed is characterized by high gradient and will show that the Bagnold hypothesis cannot be valid. A new model of bedload transport will then be proposed based on experimental observations proposed by Fernandez Luque & van Beek (1976). The latter suggest that equilibrium of the bed interface occurs when the sediment entrained flux equals the deposited flux. Equilibrium of the bed is then achieved only through a dynamic sediment balance.

Part one

Topics in lagoon morphodynamics

Chapter 1

Introduction

The morphological characteristics of estuaries arise from a combination of hydrodynamic factors (tides, river inflow, estuarine circulation, waves) and sedimentological features. Estuaries can be classified according to many viewpoints; Pritchard (1960) proposed four groups: drowned rivers, fjords, bar-built estuaries and tectonic estuaries. Hayes (1975) defined three classes of estuaries based on tidal range: microtidal (tidal range < 2 m), mesotidal (tidal range 2-4 m), macrotidal (tidal range > 4 m). Dalrymple et al. (1992) indicated two fundamental groups of estuaries: wave-dominated estuaries and tide-dominated estuaries. The classification of Dalrymple et al. (1992) involves the relative role played by river outflow, waves and tides. Tides and waves may be significant at and near the mouth, but when tidal currents are much stronger than both wave currents and river discharge in the middle and upper estuary, then the estuary is said to be tide-dominated. Note that tidal dominance can also occur in micro-tidal coasts when the wave activity is negligible. Tide-dominated estuaries typically have a tidal prism at least an order of magnitude greater than river discharge; moreover the tidal wave provides the major mechanism controlling sediment dynamics. Hence a major aspect of tide-dominated estuaries is the way in which tide propagates upstream. Tide hydrodynamics is governed by the shallow water equations, hence estuarine tides deform during upstream propagation. As it has been pointed out by

Lanzoni & Seminara (1998), frictionally dominated estuaries display a flood dominated character. The main implications are twofold. Firstly, flood velocities will exceed ebb velocities, but the ebb phase will be of shorter duration. Secondly, the period of high-water slack will become longer than that for low-water slack. In many estuaries the degree of tidal asymmetry increases upstream, thereby magnifying the differences between ebb and flood velocities and slack-water durations. In response to the asymmetry of the temporal distribution of flow velocity, a net upstream sediment transport is observed in most tide-dominated systems (Wells, 1995). Net upstream transport continues to the point where tide is damped out by frictional attenuation and transport is controlled only by fluvial processes. Periods of slack water affect sedimentation by providing an opportunity for deposition of muds. Longer periods of slack water following flooding tides, as a result of tidal deformation, will favor deposition of sediment in the upstream reaches of an estuary. The ability of ebb tides to erode these deposits could be diminished by two factors referred to as settling lag and scour lag. The former lag indicates the temporal delay between the time at which the flooding current, slowing down, can no longer hold particles of a given size in suspension and the time at which they reach the bottom. The latter lag refers to the fact that once sand particles are set in motion they can be kept in motion at speeds below the threshold of initial motion. Consequently, between the threshold of erosion and the threshold of deposition, sediment is kept in motion, but no new erosion takes place.
Understanding the sediment dynamics is crucial to evaluate the net sediment flux which enters or leaves the system at any tidal cycle. The knowledge of the variation in time of such flux allows one to investigate the long term morphodynamic evolution of a tidal channel and search for a possible equilibrium configuration. Such question has been recently tackled by Lanzoni & Seminara (2000). They have shown, by numerically solving the one-dimensional de Saint Venant and Exner equations, that the bottom profile of flood dominated estuaries evolves asymptotically towards an equilibrium configuration on a time scale of the order of hundreds of years. Such configuration is characterized by a vanishing sediment flux over a tidal cycle at any cross section along the channel (see also chapter 3).

Tide-dominated estuaries are composed of sediments derived from both fluvial and offshore sources, in the latter case they are transported by the littoral current and are introduced into the estuary by tidal action or littoral

drift. The distribution of sediment inside the estuary is extremely variable, ranging from gravel to mud. Whereas finer sands and muds have fluvial origin, coarser sands are typically derived from the shelf or from erosion of the shoreline. Sediment can be transported by the tidal current in three different modes: wash load, suspension and bedload. Wash load comprises the finest fraction, and is normally composed of fine dispersed clay particles. The vertical profile of wash load concentration is homogeneous. Suspension occurs because of entrainment of sediment particles from the bed and the exchange of momentum with the grains driven by turbulence. The concentration profile of suspended sediment is maximum near the bottom and minimum at the free surface.

It may be of interest at this stage to mention some typical data from a morphological investigation performed in the Venice Lagoon (Danish Hydraulic Institute, 1990). They suggest that the peak of the depth averaged velocity ranges about (0.5-1) m/s, the mean sediment diameter falls in the range (50-100)μm and the mean flow depth is about 5 m in the main channels. The peak of Shields parameter then ranges between (0.6-2.4) having calculated the friction coefficient by means of van Rijn's (1984) formula which accounts for the presence of dunes (see chapter 1, section 6 for details). Furthermore, measurements of sediment concentration in suspension reveal that depth-averaged concentration ranges about (5-45) mg/l when the average speed is (0.1-0.7) m/s respectively and in the case of a non cohesive quartz grain characterized by a mean sediment diameter of about 100 μm. Note that suspension may represent the main component of sediment transport. In fact, for values of the peak depth average speed ranging (0.5-1) m/s, calculating the reference concentration by van Rijn's (1984) formula and bed load transport by Meyer-Peter Muller's formula, the ratio suspended/bed load attains values ranging between 2 and 13, if the mean sediment diameter is $100\mu m$ and the mean flow depth is $5m$.

The morphology of tide-dominated estuaries is characterized in plan view by a funnel-shaped geometry. The width/depth ratio of the channel attains relatively high value ranging from 10-100 in ria valleys to 1000 (e.g. Cheasapeake bay). The width of estuaries often decreases often at an exponential rate upstream. The tidally influenced distributary channels within the funnel shape usually have low sinuosity. Moving landward, the funnel shape

evolves towards a sinuous pattern upstream. The region of intense meandering usually occurs as the upper limit of tide influence is approached. Tidal flats occur along some stretches of coastline and within estuaries. They are often backed by salt-marsh areas and dissected by a network of tidal channels. Tidal flats are usually characterized by a weak landward slope and are composed predominantly of silt and clay. At the seaward boundary tidal flats are submerged for most of the tidal cycle, consequently the finest sediment part is kept in suspension under the action of wave motion. At the landward boundary tidal flats are submerged only at high tide when the current speed vanishes. Mud, which typically consists of clay with a variable silt content, is deposited during the slack water period to form mud-flats. Muds are cohesive, therefore they are relatively difficult to erode after deposition has occurred. Laboratory experiments using muds from Wadden Sea, indicated that a current of 0.4-0.5 m/s was required to bring into suspension muds that had been allowed to settle for 16 hours, whereas deposition occurred only when the speed was about 0.1-0.2 m/s (Brown et al., 1989). The deposition of the finest sediment is enhanced by the settling lag effect; during the period of high water slack such grains begin to settle from suspension until they are deposited at some distance inland from the point at which they begin to settle. As a consequence, during the ebb phase such sediments will not be resuspended until much later in the flow. Another factor increasing the depositional character of high tidal flats is represented by the colonization of land plants such as Salicornia and Spartinia. The growth of such plants leads to the formation of salt marshes normally flooded during high spring tides. The salt marsh gradually extends seawards while the older landward regions are flooded less frequently.

Channel bottom morphology consists of a wide variety of bedforms at scales ranging from centimeters to kilometers.
Tidal sand ridges with superimposed dunes are typical of tide-dominated estuaries and represent the most pronounced morphological features. They are oriented approximately parallel to the axis of main tidal flow. These bedforms form at the channel mouth and can reach lengths of kilometers and heights of the order of tens of meters (e.g. Ord Estuary).
Moving inward along the channel, smaller scale bedforms are present, sometimes called repetitive barforms (i.e. alternate, point and braid bars) (Dalrymble and Rhodes, 1995). The formation of bars in straight tidal channels has been recently studied by Seminara & Tubino (2000) who have shown that an

instability mechanism somewhat similar to that operating in the steady fluvial case acts also in the tidal environment. In the absence of a mean current tidal free bars migrate alternatively backward and forward in a symmetric fashion, hence they do not exhibit a net migration over a tidal cycle. For the set of parameter values typically observed in the main channels of the Venice Lagoon (mean sediment diameter of $100\mu m$, mean flow depth of 5m, peak of depth-averaged speed ranging between 0.5-1m/s) (Danish Hydraulic Institute, 1990), Seminara & Tubino (2000) predict that tidal alternate bars display a wavelength which is (8-40) times channel width when the ratio half width/flow depth ranges between (5-30).

Point bars are large scale bedforms also observed in meandering tidal channels. Unlike fluvial point bars, tidal point bars migrate back and forth around the bend apex with no net migration in a tidal cycle. Meandering channels (see chapter 2) are characterized by channel widths which may vary by two orders of magnitude moving upstream. Despite such variation, the morphological analysis developed by Lanzoni, Marani and Rinaldo (Solari et al., 2000) on three distinct tidal environments, shows that meander wavelength keeps remarkably constant ranging about 8-15 channel widths. The ratio half width/flow depth of the channel does not seem to exceed the value of 10, a value which is smaller than that observed in the fluvial case. The product of local curvature and half width may attain a large value (greater than 1), but in the average and for the cases reported in Solari et al. (2000) it takes a value ranging between 0.06 and 0.22. It is worth noting again that, despite channel width variation, the product of local curvature and channel width maintains a remarkably constant mean.

Smaller bedforms such as dunes are widespread in tide-dominated estuaries. Their presence affects flow dynamics, leading to higher values of the friction coefficient. As suggested by field measurements taken at a site in the Minas Basin in the Bay of Fundy (Rhodes, 1992) dunes scale with flow depth, displaying heights ranging between about 2% and 5% of the flow depth and wavelengths falling in the range (0.3-0.6) times the flow depth, respectively.

References

Brown, J., Colling, A., Park, D., Phillips, J., Rothery, D. & Wright, J., Waves, Tides and shallow-water processes, *G. Bearmann (Editor), The Open University*, Wheatons, Exeter, UK, 187 pp., 1997.

Dalrymple, R. W., Zaitlin, B. A. & Boyd, D. W., 1963, Estuaries, in: *M. N. Hill (Editor), The Sea*, Wiley-Interscience, New York, 2:306-324, 1992.

Dalrymple, R.W. & Rhodes, R.M., Estuarine dunes and bars, in: *G. M. E. Perillo (Editor), Geomorphology and Sedimentology of Estuaries, Development in Sedimentology, 53*, Elsevier Science, Amsterdam, 359-422, 1995.

Danish Hydraulic Institute, Venice Lagoon - Study C.2.3: Morphological Field Investigations, Intensive measurements, Final report, *Consorzio Venezia Nuova*, 1990.

Hayes, M. O., Morphology of sand accumulation in estuaries: an introduction to the symposium, in: *L. E. Cronin (Editor), Estuarine Research*, vol. II, Academic Press, New York, pp. 3-22, 1975.

Lanzoni, S. & Seminara, G., On tide propagation in convergent estuaries, *J. Geophys. Res.*, 103, C13, 793-812, 1998.

Lanzoni, S. & Seminara, G., Long term evolution and morphodynamic equilibrium of tidal channels, *J. Geophys. Res.*, submitted, 2000.

Wells, J. T., Tide-dominated estuaries and tidal rivers, in: *G. M. E. Perillo (Editor) Geomorphology and Sedimentology of Estuaries, Development in Sedimentology, 53*, Elsevier Science, Amsterdam, 179-205, 1995.

Pritchard, D. W., Lectures on estuarine oceanography, *B. Kinsman (Editor), J. Hopkins Univ.*, 154 pp., 1960.

Rhodes, R. N., Hydrodynamics and the morphology, migration and structure of subaqueous dunes, Minas Basin, Canada, M. Sc. thesis, Queen's Univ., Kingston, Ont., 250 pp.

Seminara, G. & Tubino, M., Sand bars in tidal channels. Part one: free bars, *J. Fluid. Mech.* (submitted), 2000.

Solari, L., Seminara, G., Lanzoni, S., Marani, M. & Rinaldo A., Sand bars in tidal

channels. Part two: Tidal meanders, *J. Fluid. Mech.* (submitted), 2000.

van Rijn, L.C., Sediment transport. Part II. Suspended load transport, *J. Hydraul. Eng. ASCE*, 110(11), 1613-1641, 1984.

Chapter 2

Tidal meandering channels

2.1 Introduction

The subject of flow and bed topography in meandering channels has been widely investigated in the fluvial case (e.g. Ikeda and Parker, 1989), but little attention has been devoted so far to meandering channels in tidal environments.

Meandering rivers are typically characterized by an alternate sequence of point bars and pools, with pools at the bend apexes, and low migration rates, of the order of meters per year. It has long been recognized that the mechanism responsible for this pattern is the interaction between secondary flow and particle dynamics. In a constant curvature channel, streamline curvature leads to an unbalance between transverse pressure gradient, practically uniform along the vertical, and centrifugal forces, which decrease form the free surface to the bottom. Such unbalance leads to a 'centrifugally driven' secondary circulation with zero mean, directed outwards at the free surface and inwards close to the bottom. If the channel bottom is erodible, a transverse slope is built up until a balance is achieved between two forces acting on each grain: on one hand the lateral bottom stress driven by the secondary flow tends to deviate the particle trajectory towards the inner bank, on the other hand the

downstream pull of gravity which acts in the opposite direction (Engelund, 1974; Kikkawa et al., 1976). In the case of longitudinal variations of channel curvature, continuity forces a further, 'topographically driven', component of secondary flow, characterized by non zero depth average, which transfers longitudinal momentum from each pool to the next one. Furthermore, sediment continuity leads to a transverse component of sediment transport which gives rise to an additional contribution to lateral slope. Note that the latter is out of phase relative to curvature, thus leading to some delay of bed topography with respect to curvature (Gottlieb, 1976; Seminara & Tubino, 1986). The presence of a significant fraction of sediments transported in suspension adds further contributions to the above balance as both the centrifugal and the topographical components of the secondary flow advect suspended sediments giving rise to additional lateral sediment fluxes. However the resulting bar - pool pattern does not change qualitatively.
In the present work we wish to extend the above framework to the tidal environment. More precisely we intend to determine flow pattern and bed topography in tidal meandering channels. The distinct novel feature of such problem is the unsteady periodic character of the basic flow which reverses its direction at each half cycle. As a result of unsteadiness, it will appear that the bar - pool pattern also oscillates in time. The analysis will be carried out for regularly meandering channels where the meander wavelength is much smaller than the tidal wavelength, a condition typical of both estuarine and lagoon environments. Under these conditions, the basic state is slowly varying in space at the bar scale and a local analysis is appropriate at the leading order of approximation. Moreover, provided local inertia is small enough, a self similar solution exists which is only parametrically dependent on time (as illustrated in section 2.4).

The knowledge of flow and bed topography in meandering channels can then be employed to investigate the problem of meander formation in tidal channels. In the river case, two main theories have been elaborated in the recent literature: they are known as bar theory and bend theory of river meandering. The former approach, whose origin may be traced back to Leopold & Wolman (1957), essentially assumes that alternate bars, i.e. free migrating waves arising from bottom instability, are precursors of meanders: in other words the presence of alternate bars in the originally straight channel would be the triggering mechanism forcing bank erosion, hence meanders and alternate

bars would display the same wavelength. On the contrary the bend approach, proposed by Ikeda et al. (1981), assumes that bank erosion originates from steady curvature induced flow perturbations, i.e. from forced modes rather than from migrating free alternate modes, hence the wavelength selected by the process of meandering initiation should be such to maximize curvature induced flow and topography perturbations. The relationship between bar and bend theories have been clarified by Blondeaux & Seminara (1985); the bend theory selects a particular free mode which does neither grow nor migrate, i.e. the bend approach may be then considered as a particular case of the bar approach. Moreover, it turns out that, for given sediment characteristics, a couple of values for width to depth ratio and meander wavenumber exists such that curvature forces a natural solution of the flow-cohesionless bed system leading to the occurrence of resonance. When resonant condition are met the system displays a peak, which is infinite in the present linearized theory, in the response of flow and bed topography. In practice exact resonance never occurs, but the wavenumber selected by bend theory is clearly related to the occurrence of quasi-resonant conditions.

In tidal environments free modes do not exhibit a net migration in a tidal cycle (see Seminara & Tubino, 2000). Hence free modes might be the triggering perturbations forcing the planimetric evolution of the channel. On the other hand, an extension of the theory of Blondeaux & Seminara (1985) to the present tidal configuration suggests that a bend instability mechanism may also operate selecting wavenumbers which are significantly smaller than the wavenumbers of free bars. Furthermore the bend theory shows that the wavenumbers of free bars fall in the stable range of bend perturbations, hence the free bar mechanism does not seem to explain the meander formation process. A comparison between the wavenumbers predicted by the present theory and the field evidence collected from topographic maps through automatic methods (Fagherazzi et al, 1999; Rinaldo et al., 1999a,b) suggests that the theory captures the correct order of magnitude of meander wavenumber, but it overpredicts systematically meander wavelengths.

The procedure employed in the rest of the paper is as follows. After a section on new field evidence we formulate the problem mathematically. In section 2.4 we show the governing equations and the solution for the basic flow and concentration field. In section 2.5 we linearize the governing equations and we derive a linear solution for flow and bed topography in meandering channels whose results are presented in section 2.6. In section 2.7 we employ

the previous findings to test the performance of a bend theory to the problem of tidal meandering initiation. Conclusions and future developments are reported in section 2.8

2.2 Field evidence

In this section we report the results of a morphological analysis of meandering patterns observed in different tidal environments, recently elaborated by Lanzoni, Marani & Rinaldo and reported in Solari et al. (2000). Data regarding widths, wavelengths and sinuousities are extracted through automatic methods (Fagherazzi et al., 1999; Rinaldo et al., 1999 a,b) from detailed maps of the Barnstable lagoon (MA, USA), the Palude Pagliaga (northern lagoon of Venice) and the Petaluma estuary of the bay of San Francisco (CA, USA). An example of an automatic channel identification from topographic data of the Palude Pagliaga in the Venice lagoon is reported in fig. 2.1 (below). The figure also shows a picture of the same area from a remotely sensed image (above). It appears that the automatic method successfully predicts the tidal network.

The variation along the longitudinal coordinate s^* [1] (taken to coincide with the channel axis) of width ($2B^*$), local curvature ($1/r^*$), wavelength (L_s^*) and channel sinuosity are shown in fig. 2.2 for a meander sequence within the Pagliaga region.

Channel sinuosity is defined as the ratio between the intrinsic (L_s^*) and the Cartesian wavelengths (L_x^*) of meanders. It is interesting to observe that widths grow dramatically along the channel, taking values which range from few meters to one hundred meters.

The dimensionless meander wavelength ($2\pi B^*/L_s^*$) is plotted in fig. 2.3 as a function of the intrinsic distance $s = s^*/s_{max}^*$ from the meander origin (s_{max}^* being the maximum distance from source to outlet for each meander) for channels within three different tidal environments. Despite almost two orders of magnitude of width growth and within rather different tidal environments, the dimensionless wavelength falls in a quite narrow range of 0.2-0.4. The same figure also shows the value taken by the parameter β, defined as the ratio between the half width of the channel and the flow depth, for few cases indicated by the legend. Notice that β does not seem to exceed the value of

[1] Hereafter a star will denote a dimensional quantity subsequently made dimensionless.

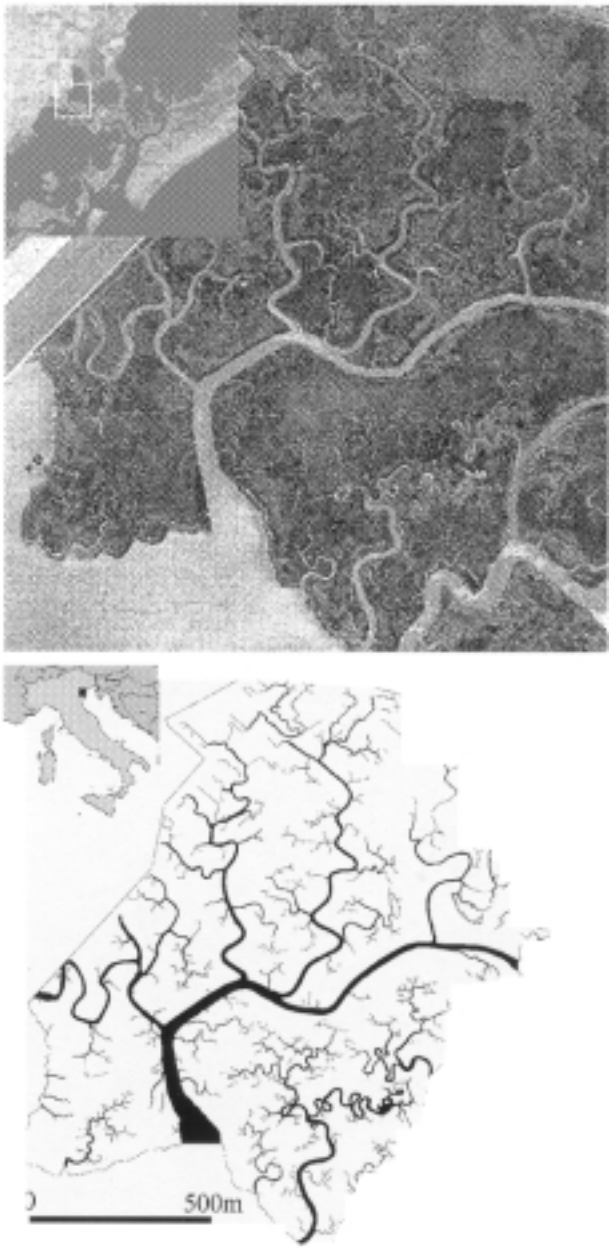

Figure 2.1: *Tidal meanders in the Palude Pagliaga in the northern lagoon of Venice as from a remotely sensed image (above) and from automatic channel identification methods of digital terrain maps (below) proposed by Fagherazzi et al. (1999).*

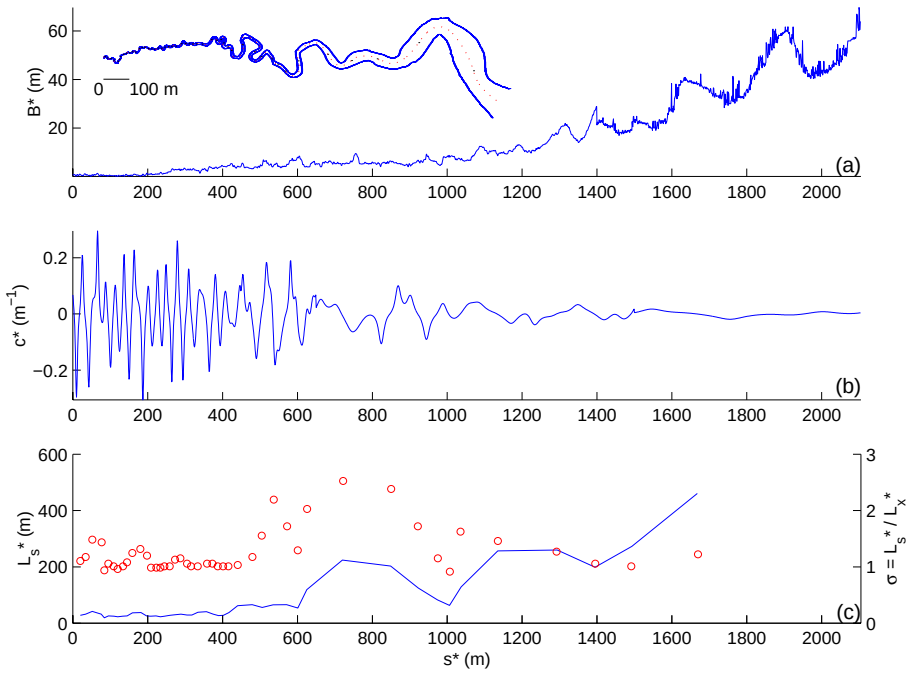

Figure 2.2: *The variation of channel width (a), of local curvature (b) and of intrinsic wavelength (c) along the channel centerline for a meander within the Palude Pagliaga.*

ten.

Figure 2.4 shows the variation along the intrinsic distance s of the dimensionless curvature (B^*/r^*) for three tidal meanders of different size and geographic location: (a) Barnstable; (b) Petaluma, full set; (c) Petaluma, detailed subset. The dotted line shows the overall average: $< r^{*-1}B^* >$ =0.22 (a); =0.14 (b); =0.06 (c). It is worth noting that the product local curvature X half width maintains a remarkably constant mean despite the large width variations illustrated in fig. 2.2.

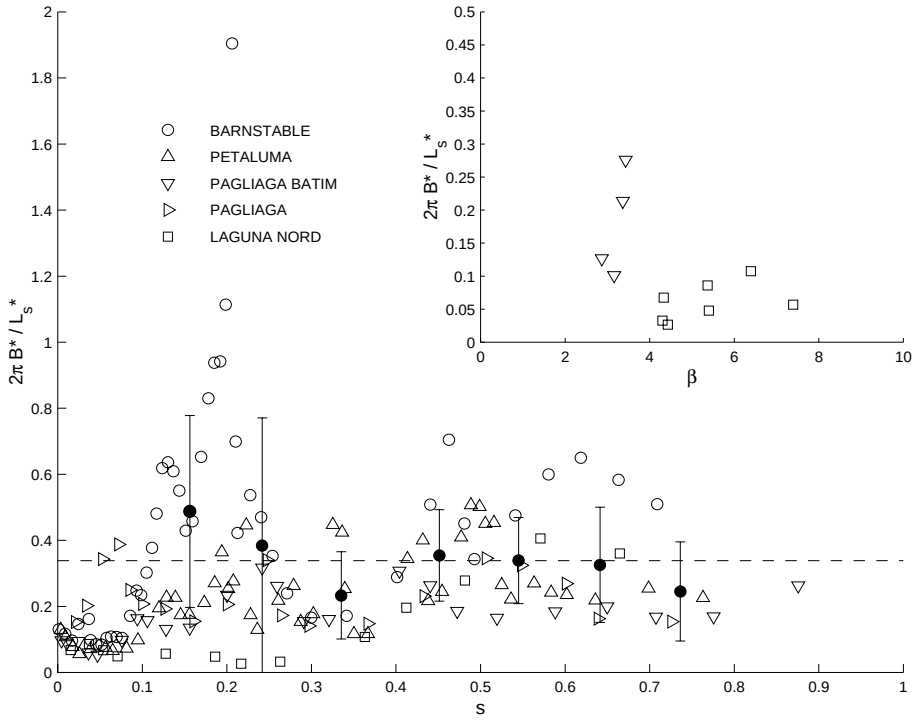

Figure 2.3: *The dimensionless wavelength as a function of the intrinsic distance from meander origin is plotted for meanders within three different tidal environments. In the inset, the ratio width to depth is plotted against the relevant dimensionless wavelengths in the few cases indicated by the legend.*

2.3 Formulation of the problem

Let us consider a long meandering channel connected at some initial cross section with a tidal sea (fig. 2.5). The channel is assumed to have a rectangular cross section of constant width $2B^*$; as it is illustrated in fig. 2.3 meander wavelength scales with the local channel width, therefore, at the scale of meander wavelength, width variations may be neglected. The bed is cohesionless, the sediment being uniform and the grain diameter d_s^* small enough for particles to be suspended by the turbulence generated by the propagation of the tidal wave throughout most of the tidal cycle. For the moment we assume the banks to be non erodible, an assumption that will be relaxed in section 2.7. Moreover, for the sake of simplicity, we assume that the curvature of

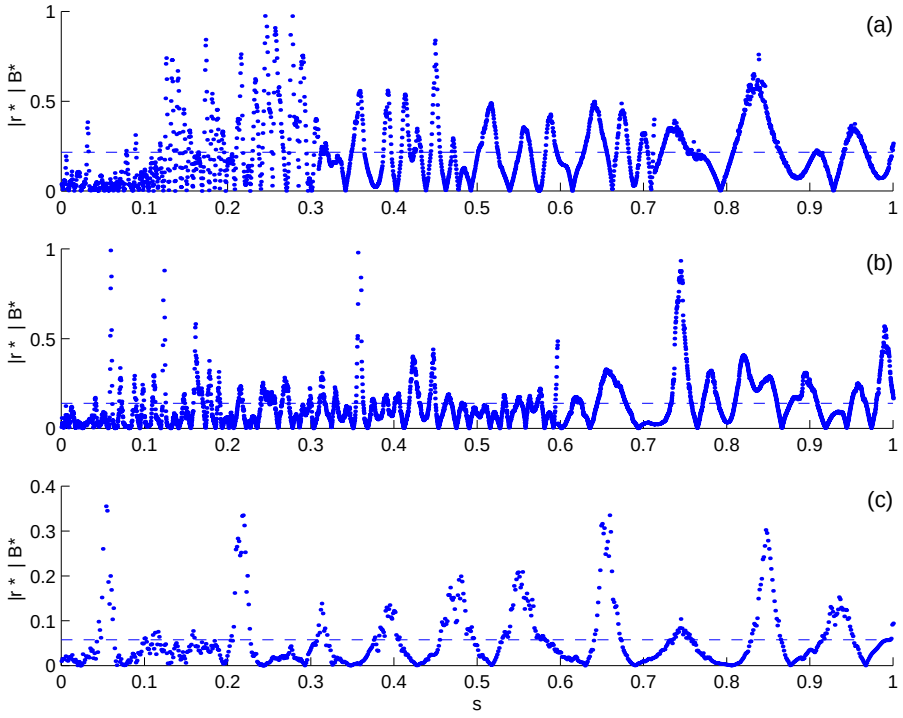

Figure 2.4: *The dimensionless curvature as a function of the intrinsic distance from meander origin is plotted for three tidal meanders: (a) Barnstable; (b) Petaluma, full set; (c) Petaluma, detailed subset.*

channel axis follows periodic oscillations described by the classical Langbein and Leopold's (1964) so called sine generated curve. Such assumption is by no means crucial, the theory developed herein being amenable to a relative straightforward generalization to an arbitrary, albeit slowly varying, curvature distribution. Hence we assume:

$$r^{*-1} = R_0^{*-1}(\exp i\lambda^* s^* + c.c.)\ , \tag{2.1}$$

where $r^*(s^*)$ is the local radius of curvature of the channel axis, R_0^* is twice the radius of curvature at the bend apex, λ^* is meander wavenumber and s^* is the longitudinal coordinate taken to coincide with the coordinate of the channel axis. As it has been illustrated in section 2.2 (fig. 2.4) and it will showed in table 2.1 of section 2.5 the ratio of channel width to the local curvature

radius of channel axis is typically fairly small in lagoon environments, such that it is convenient to introduce the small parameter:

$$\nu = \frac{B^*}{R_0^*} \,, \tag{2.2}$$

which will be set at the basis of a perturbation expansion of the solution derived in the section 2.5. It is appropriate to refer flow and bed topography to the orthogonal curvilinear coordinate system (s^*, n^*, z^*) where s^* is the longitudinal coordinate defined previously, n^* is the coordinate of the transverse horizontal axis orthogonal to s^* and z^* is the usual vertical coordinate. Furthermore, let a_0^* be a scale for the amplitude of free surface oscillations about the mean water level defined by the difference between the water surface elevation H_0^* and a reference flow depth D_0^*. We assume that, as it is typical of many tidal environments, we can write

$$\epsilon = \frac{a_0^*}{D_0^*} \ll 1 \,, \qquad\qquad \beta = \frac{B^*}{D_0^*} \gg 1 \,. \tag{2.3a, b}$$

Typical values of ϵ in tidal channels of Venice lagoon vary widely ranging from values around 0.05 typical of the deeper channels up to values of order one characteristic of very shallow channels. Tidal channels are somewhat narrower than fluvial channels exhibiting values of β which typically do not exceed 10 (see fig. 2.3).

We then make the relevant physical quantities dimensionless as follows:

$$(s^*, n^*) = B^*(s, n) \,, \qquad (z^*, H^*, D^*) = D_0^*(z, H, D) \,,$$

$$(U^*, V^*, W^*) = V_0^* \left(U, V, \frac{W}{\beta} \right) \,, \qquad P^* = \varrho V_0^{2*} P \,,$$

$$t = \omega t^* \,, \qquad (\nu_T^*, \psi^*) = V_0^* D_0^* \sqrt{C_{f0}} (\nu_T, \psi) \,, \tag{2.4$a - f$}$$

having employed the following notations (see also figure 2.5):

H^* : local free surface elevation;
D^* : local flow depth;
(U^*, V^*, W^*) : longitudinal, transverse and vertical components of the mean local velocity;
P^* : mean pressure;

t^* : time;
ν_T^* : eddy viscosity;
ψ^* : eddy diffusivity of suspended particles;
ϱ : density of water;
V_0^* : characteristic flow speed;
ω : angular frequency of the tide;
C_{f0} : reference friction coefficient.

Typical values of the reference speed V_0^* range about (0.5 - 1) m/s. The reference friction coefficient C_{f0} attains typical values about $(2-5)\cdot 10^{-3}$. Note that the vertical velocity is $O(\beta)$ smaller than the lateral velocity. Using the

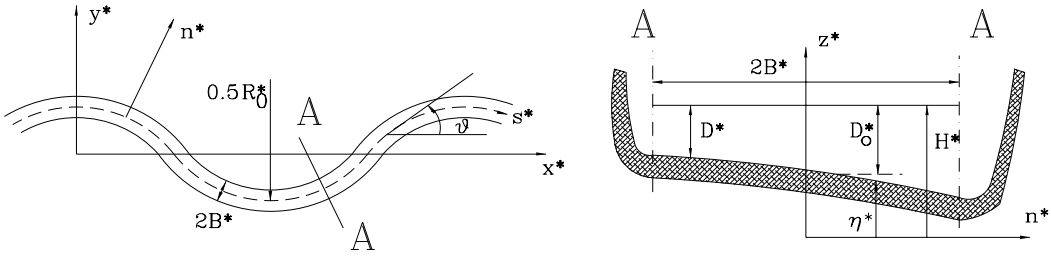

Figure 2.5: *Sketch and notations.*

above dimensionless variables and a Boussinesq closure, Reynolds equations read

$$\mathcal{L}U = - N\frac{\partial P}{\partial s} + \beta\sqrt{C_{f0}}\frac{\partial}{\partial z}\left[\nu_T\frac{\partial U}{\partial z}\right] - \nu c(s)NUV \,, \tag{2.5}$$

$$\mathcal{L}V = - \frac{\partial P}{\partial y} + \beta\sqrt{C_{f0}}\frac{\partial}{\partial z}\left[\nu_T\frac{\partial V}{\partial z}\right] + \nu c(s)NU^2 \,, \tag{2.6}$$

$$0 = - \frac{\partial P}{\partial z} - \frac{1}{\mathcal{F}^2} \,, \tag{2.7}$$

$$N\frac{\partial U}{\partial s} + \left[\frac{\partial}{\partial n} + \nu N c(s)\right]V + \frac{\partial W}{\partial z} = 0 \,, \tag{2.8}$$

with $\mathcal{L}$ the following differential operator

$$\mathcal{L} \equiv \sigma_0\frac{\partial}{\partial t} + NU\frac{\partial}{\partial s} + V\frac{\partial}{\partial y} + W\frac{\partial}{\partial z} \,, \tag{2.9}$$

N^{-1} being the dimensionless form of the longitudinal metric coefficient which reads:

$$N^{-1} = [1 + \nu n c(s)] \ , \tag{2.10}$$

having denoted by $c(s)$ the function defining the longitudinal variation of the dimensionless curvature B^*/r^*. The dimensionless parameters σ_0 and $\mathcal{F}^2$ read

$$\sigma_0 = \frac{\omega B^*}{V_0^*} \ , \qquad \mathcal{F}^2 = \frac{V_0^{2*}}{\mathrm{g} D_0^*} \ , \tag{2.11a, b}$$

where g is gravity. Note that in (2.5-2.6) we have retained only the dominant components of the Reynolds stress tensor as we concentrate our study in the central region of the flow field, therefore the side wall boundary layers, associated with the presence of the channel banks, are excluded from the present analysis. This is known from the fluvial literature to be a convenient approximation for wide cross sections with gently sloping banks. Equation (2.7) simply states, in dimensionless form, that the mean pressure is hydrostatically distributed.

Notice that σ_0 represents the ratio between the time required for the flow to travel along a reach of length B^* and the tidal period. With typical values of B^* of the order of tens or hundreds of meters and V_0^* ranging about 1 m/s, the value of σ_0 for a semidiurnal tide ($\omega = 1.4 \cdot 10^{-4} s^{-1}$) falls roughly in the range (10^{-3} - 10^{-2}). This suggests that inertial effects play a negligible role on flow processes occurring at the spatial scale of channel widths. Also note that in (2.5-2.7) we have neglected the effect of Coriolis forces which turn out to scale with the inverse of the Rossby number $V_0^*/(\Omega B^*)$, where Ω is the angular frequency associated with earth rotation. Since Ω is comparable with ω, it turns out that the effect of Coriolis acceleration is as small as inertial effects in tidal channels.

The boundary conditions to be associated with equations (2.5- 2.8) impose no slip at the bed, the requirement that the free surface must be a material surface and vanishing stresses at the free surface. They read

$$U = V = W = 0 \qquad (z = H - D + z_o D) \ , \tag{2.12a, b}$$

$$\left(\sigma_0 \frac{\partial}{\partial t} + NU \frac{\partial}{\partial s} + V \frac{\partial}{\partial n} \right) H - W = 0 \qquad (z = H) \ , \tag{2.13}$$

$$P = 0 \qquad (z = H) \ , \tag{2.14}$$

$$\frac{\partial V}{\partial z} = 0 \qquad (z = H) \,, \tag{2.15}$$

$$\frac{\partial U}{\partial z} = 0 \qquad (z = H) \,, \tag{2.16}$$

with z_0 dimensionless value of the conventional reference level for no-slip under uniform flow conditions. Notice that, in writing (2.14-2.16), we have taken into account the nearly horizontal character of the free surface.

At the channel banks, following the classical approach employed in the fluvial literature, (which ignores the side wall boundary layers, Engelund (1974), Seminara & Tubino (1986)) we impose the condition of vanishing transverse component of the water flux. This condition will be further clarified in the next section where the transverse component of the mean velocity will be decomposed into a centrifugally induced contribution characterized by vanishing depth average and a topographically induced contribution with non vanishing depth average. As a consequence of the boundary condition at the channel banks, the latter component of the secondary flow must vanish. Hence

$$V = 0 \qquad\qquad n = \pm 1 \,. \tag{2.17}$$

A closure assumption for the eddy viscosity ν_T may be obtained assuming that the slow time variation of the flow field leads to a quasi-steady sequence of equilibrium states. Hence we write

$$\nu_T = \mathcal{N}(Z) u_* D \,, \tag{2.18}$$

where $\mathcal{N}(Z)$ is the distribution of eddy viscosity at equilibrium, with Z normalized vertical coordinate which reads

$$Z = \frac{z - (H - D)}{D} \,. \tag{2.19}$$

Moreover u_* is a characteristic instantaneous value of a dimensionless friction velocity defined as $\sqrt{|\boldsymbol{\tau}^*|/(\varrho V_0^{*2} C_{f0})}$, with $\boldsymbol{\tau}^*$ local and instantaneous component of the stress vector acting on a plane locally tangent to the bottom.

Mass balance of sediment transported as suspended load leads to a convection-diffusion equation for the volumetric sediment concentration $\mathcal{C}$ which reads

$$\mathcal{L}\mathcal{C} - \beta W_s \frac{\partial \mathcal{C}}{\partial z} = \beta \sqrt{C_{f0}} \frac{\partial}{\partial z} \left[\psi \frac{\partial \mathcal{C}}{\partial z} \right] \,, \tag{2.20}$$

with W_s dimensionless value of the particle fall velocity defined in the form:

$$W_s = \frac{W_s^*}{V_0^*} \,. \tag{2.21}$$

In equation (2.20) we have neglected lateral and longitudinal diffusion which are $O(\beta^2)$ smaller than the vertical diffusion term at least in the central region of the flow, as narrow channels and the side wall boundary layers are excluded from the present analysis. The typical size of sediments in tidal environments ranges about 0.1 mm, corresponding to a dimensional value of the settling speed about 1 cm/s. Hence its dimensionless value (2.21) ranges about 10^{-2}.

We point out that (2.20) is based on the assumption that the size and concentration of sediment particles are small enough for sediment to play an essentially passive role, being transported by the fluid except for the tendency of particles to settle (Lumley, 1976).

The boundary conditions associated with (2.20) impose vanishing sediment flux at the side walls and at the free surface. Furthermore at the bed we impose the so called 'gradient boundary condition', such condition assumes the net sediment flux proportional to the difference between the actual local instantaneous concentration and the value that concentration would attain at equilibrium with the local and instantaneous flow conditions. The proportionality constant is taken as usual to be equal to the particle velocity normal to the bed. The resulting form of the boundary conditions reads:

$$\boldsymbol{\nabla}\mathcal{C} \cdot \mathbf{n_b} = 0 \qquad (n = \pm 1) \,, \tag{2.22}$$

$$[W_s \mathbf{k}\mathcal{C} + \sqrt{C_{fo}}\psi \boldsymbol{\nabla}\mathcal{C}] \cdot \mathbf{n} = 0 \qquad (z = H) \,, \tag{2.23}$$

$$[W_s \mathbf{k}\mathcal{C}_e + \sqrt{C_{fo}}\psi \boldsymbol{\nabla}\mathcal{C}] \cdot \mathbf{n} = 0 \qquad (z = H - D + a_r D) \,, \tag{2.24}$$

where $\boldsymbol{\nabla}$ is the dimensionless form of the gradient vector, namely $(1/\beta\partial/\partial s, 1/\beta\partial/\partial n, \partial/\partial z)$, $\mathbf{k}$ is the unit vector in the z direction, $\mathbf{n}$ is the unit vector in the direction normal to the surface, $\mathbf{n_b}$ is the unit vector in the direction normal to the channel banks, $\mathcal{C}_e$ is the equilibrium value of bed concentration and $a_r = a_r^*/D_0^*$ is the conventional dimensionless value of the reference elevation at which the boundary condition is imposed under uniform conditions.

Several empirical expressions for $\mathcal{C}_e$ and a_r are available in the literature. They correlate $\mathcal{C}_e$ with a dimensionless measure of bottom stress, in the form

of the so called Shields parameter θ, and with particle Reynolds number R_p, which read

$$\theta = \frac{|\boldsymbol{\tau}^*|}{(\varrho_s - \varrho)\mathrm{g}d_s^*} , \qquad R_p = \frac{\sqrt{(s-1)\mathrm{g}d_s^{*3}}}{\nu} , \qquad (2.25a, b)$$

where ϱ_s is the density of sediment particles, $s = \varrho_s/\varrho$ and ν is kinematic viscosity. In tidal environments θ might typically reach peaks up to (1-2).

A closure assumption for the eddy diffusivity ψ is also required. A line of reasoning similar to that which leads to (2.18) allows us to write

$$\psi = \Psi(Z) u_* D , \qquad (2.26)$$

where $\Psi(Z)$ is the vertical distribution of eddy diffusivity at equilibrium.

The mathematical problem is finally closed imposing the continuity equation for the sediment which governs the development of bottom elevation. It may be written in the following dimensionless form

$$\frac{\sigma_0}{\beta}\frac{\partial}{\partial t}\left[\mathcal{C}_M(H-D) + \int_{a_r}^{D} \mathcal{C} dz\right] + N\frac{\partial Q_s}{\partial s} + \left[\frac{\partial}{\partial n} + \nu c(s) N\right] Q_n = 0 , \qquad (2.27)$$

where $\mathcal{C}_M$ is the packing concentration of the granular bed ranging about 0.6, while Q_s and Q_n are the longitudinal and transverse components of the total sediment flux, defined in the form:

$$(Q_s, Q_n) = Q_0 (Q_{bs}, Q_{bn}) + \int_{a_r}^{H} (U, V) \mathcal{C} dz . \qquad (2.28)$$

Note that the bed load vector $\mathbf{Q}_b \equiv (Q_{bs}, Q_{bn})$ has been made dimensionless by means of the classical Einstein's scale and Q_0 is the dimensionless parameter $[(\sqrt{(s-1)\mathrm{g}d_s^{*3}})/V_0^* B^*]$. The latter equation requires a closure relationship for $\mathbf{Q}_b$ able to account for the influence of the sloping bed on particle trajectories. In fact, it is well known from the fluvial literature that on a sloping bottom bedload deviates from the direction of bottom stress due to effect of the lateral component of gravity. In a linear context, like the one developed in section 2.5, it is fairly established (see Kovacs & Parker (1994) and Talmon et al. (1995)) that one may write:

$$\mathbf{Q}_b = \phi_b \left\{ \frac{\boldsymbol{\tau}}{|\boldsymbol{\tau}|} - \frac{r}{\beta\theta^m}\frac{\partial(H-D)}{\partial y} \right\} , \qquad (2.29)$$

where $\phi_b(\theta)$ is the intensity of bed load transport under equilibrium conditions; r and m are parameters estimated on the basis of experimental observations. We follow Talmon et al. (1995) and take $r = 0.56$, $m = 1/2$.

The effect of longitudinal slope on bed load intensity is accounted for by introducing a corrected value $\hat{\theta}_c$ of the critical Shields stress in the form

$$\hat{\theta}_c = \theta_c - \frac{r_1}{\beta}\frac{\partial(H-D)}{\partial x} \ , \tag{2.30}$$

with r_1 empirical constant which ranges about 0.1.

The system (2.5-2.30) forms a closed set of equations which may be solved once expressions for $\mathcal{N}(Z)$, $\Psi(Z), C_{f0}$ and ϕ_b are known.

It will prove convenient in the following to employ the vertical coordinate Z scaled by the local flow depth, defined by (2.19). We then write:

$$\left(\frac{\partial}{\partial t}, \frac{\partial}{\partial s}, \frac{\partial}{\partial n}, \frac{\partial}{\partial z}\right) = \left(q_t, q_s, q_n, \frac{1}{D}\frac{\partial}{\partial Z}\right) \ , \tag{2.31}$$

having defined the operator $q_j (j = t, s, n)$ in the form:

$$q_j = \frac{\partial}{\partial j} - \left[\frac{Z}{D}\frac{\partial D}{\partial j} + \frac{1}{D}\frac{\partial(H-D)}{\partial j}\right]\frac{\partial}{\partial Z} \ . \tag{2.32}$$

The momentum equation (2.7) with the boundary condition (2.14) is then readily solved to give the hydrostatic distribution for P:

$$P = \frac{D}{\mathcal{F}^2}(1-Z) \ . \tag{2.33}$$

Hence:

$$q_s P = \frac{\partial P}{\partial s} + \frac{1-Z}{D}\frac{\partial D}{\partial s}\frac{\partial P}{\partial Z} - \frac{1}{D}\frac{\partial H}{\partial s}\frac{\partial P}{\partial Z} = \frac{1}{\mathcal{F}^2}\frac{\partial H}{\partial s} \ , \tag{2.34}$$

and

$$q_n P = \frac{1}{\mathcal{F}^2}\frac{\partial H}{\partial n} \ . \tag{2.35}$$

The momentum and continuity equations (2.5, 2.6, 2.8) are then readily given the following form:

$$LU = -\frac{N}{\mathcal{F}^2}\frac{\partial H}{\partial s} + \frac{\beta\sqrt{C_{f0}}}{D^2}\frac{\partial}{\partial Z}\left[\nu_T\frac{\partial U}{\partial Z}\right] - \nu c(s) NUV \ , \tag{2.36}$$

$$LV = -\frac{1}{\mathcal{F}^2}\frac{\partial H}{\partial n} + \frac{\beta\sqrt{C_{f0}}}{D^2}\frac{\partial}{\partial Z}\left[\nu_T\frac{\partial V}{\partial Z}\right] + \nu c(s) N U^2 \,, \tag{2.37}$$

$$N q_s U + \left[q_n + \nu N c(s)\right] V + \frac{1}{D}\frac{\partial W}{\partial Z} = 0 \,, \tag{2.38}$$

where L is the following partial differential operator:

$$L \equiv \sigma_0 q_t + N U q_s + V q_n + \frac{W}{D}\frac{\partial}{\partial Z} \,. \tag{2.39}$$

The boundary conditions (2.12-2.16) become:

$$U = V = W = 0 \qquad (Z = Z_0) \,, \tag{2.40}$$

$$\left[\sigma_0 q_t + N U q_s + V q_n\right] H - W = 0 \qquad (Z = 1) \,, \tag{2.41}$$

$$\frac{\partial V}{\partial Z} = \frac{\partial U}{\partial Z} = 0 \qquad (Z = 1) \,, \tag{2.42}$$

The convection-diffusion equation (2.20) takes the form:

$$L\mathcal{C} - \beta\frac{W_s}{D}\frac{\partial \mathcal{C}}{\partial Z} = \frac{\beta\sqrt{C_{f0}}}{D^2}\frac{\partial}{\partial Z}\left(\psi\frac{\partial \mathcal{C}}{\partial Z}\right) \,, \tag{2.43}$$

The latter equation must be solved with the boundary conditions (2.23-2.24) where the gradient operator $\boldsymbol{\nabla}$ now reads:

$$\boldsymbol{\nabla} = \left(\frac{N}{\beta}q_s, \frac{1}{\beta}q_n, \frac{1}{D}\frac{\partial}{\partial Z}\right) \,. \tag{2.44}$$

Finally the bottom evolution equation in the present coordinate system reads:

$$\frac{\sigma_0}{\beta}\frac{\partial}{\partial t}\left[\mathcal{C}_M(H - D) + D\int_{a_r}^{1}\mathcal{C}dZ\right] + N\frac{\partial Q_s}{\partial s} + \left[\frac{\partial}{\partial n} + \nu c(s) N\right] Q_n = 0 \,, \tag{2.45}$$

where the total sediment flux now takes the form:

$$(Q_s, Q_n) = Q_0(Q_{bs}, Q_{bn}) + D\int_{a_r}^{1}(U, V)\mathcal{C}dZ \,. \tag{2.46}$$

In the following we will consider the periodic distribution (2.1) which is equivalent to the following form of the function $c(s)$:

$$c(s) = \exp(i\lambda s) + c.c. \,, \tag{2.47}$$

where λ is the meander wavenumber scaled by B^{*-1}. As a result of such a choice, the end conditions will be simply replaced by periodicity conditions in space while initial conditions are replaced by periodicity conditions in time.

2.4 The basic flow and concentration fields

The basic flow essentially consists of a tidal wave propagating in a long rectangular channel with slowly varying width. This is a subject which has recently received a considerable attention (see in particular the recent contribution of Lanzoni & Seminara, 1998). In the present work, the scale of a single meander wavelength (ranging about $8 - 15$ channel widths) is orders of magnitude smaller than the wavelength of the tidal wave therefore the local basic state can be regarded as an unsteady uniform flow. In other words, bars feel the tide propagation as an oscillatory, longitudinally uniform, flow associated with a horizontal configuration of the free surface, which simply oscillates in time. The temporal dependence of the basic velocity field and of the free surface oscillations is the solution of the one dimensional problem of tide propagation in the whole channel, a problem which is completely independent (decoupled) from the problem investigated in the present chapter. Hence, we do not need to solve the former problem and simply assume any temporal dependence for the basic velocity field. In order to derive the local structure of the basic flow we define a suitable dimensionless longitudinal coordinate ξ

$$\xi = \gamma s \, , \tag{2.48}$$

where

$$\gamma \equiv \frac{B^*}{L^*} \ll 1 \, , \tag{2.49}$$

and L^* is the spatial scale of the tidal wave. Note that we ignore any further slow spatial dependence associated with channel convergence and restrict ourselves to a leading order representation of the basic flow ignoring the lateral component of the basic velocity field. Since

$$\frac{\partial}{\partial s} = \gamma \frac{\partial}{\partial \xi} \, , \tag{2.50}$$

the balance expressed by the continuity equation (2.38) implies that:

$$W \sim O(\gamma) \, . \tag{2.51}$$

The appropriate choice for the velocity scale V_0^* then arises from the dominant balance imposed by the kinematic condition at the free surface (2.41). Since

$$\frac{\sigma_0}{U} \frac{\partial H / \partial t}{\partial H / \partial s} \sim O\left(\frac{\sigma_0}{\gamma}\right) = \frac{\omega L^*}{V_0^*} \tag{2.52}$$

and the flow speed V_0^* is typically much smaller than the tidal wavespeed (ωL^*), it follows that the terms balancing in (2.41) are W and $\sigma_0 \partial H/\partial t$. Hence we require that

$$\sigma_0 \frac{a_0^*}{D_0^*} = \gamma \ . \tag{2.53}$$

Recalling the definition of the parameter σ_0 (2.11a), the condition (2.53) leads to the following expression for V_0^*

$$V_0^* = \omega L^* \epsilon \ . \tag{2.54}$$

Based on (2.51) we then rescale U and W in the form

$$U = U_0 \ , \qquad W = \gamma W_0 \ , \tag{2.55a, b}$$

where U_0 and W_0 are functions of ξ, t and Z, and we rewrite the governing equations (2.36-2.38) in a form appropriate for the analysis of the basic flow:

$$L_0 U_0 \quad = \quad -\frac{\gamma}{\mathcal{F}^2}\frac{\partial H}{\partial \xi} + \frac{\beta\sqrt{C_{f0}}}{D^2}\frac{\partial}{\partial Z}\left(\nu_T \frac{\partial U_0}{\partial Z}\right) \ , \tag{2.56}$$

$$\frac{1}{D}\frac{\partial W_0}{\partial Z} = -q_\xi U_0 \ , \tag{2.57}$$

where D is an $O(1)$ quantity, N takes the value 1 and L_0 is the following linear partial differential operator:

$$L_0 \equiv \frac{\gamma}{\epsilon} q_t + \gamma U_0 q_\xi + \gamma \frac{W_0}{D}\frac{\partial}{\partial Z} \ . \tag{2.58}$$

Similarly the boundary conditions (2.40-2.42) take the following form:

$$U_0 = W_0 = 0 \qquad (Z = Z_0) \ , \tag{2.59a, b}$$

$$\frac{\partial U_0}{\partial Z} = 0 \qquad (Z = 1) \ , \tag{2.60}$$

$$\frac{1}{\epsilon}\frac{\partial H}{\partial t} + U_0 \frac{\partial H}{\partial \xi} - W_0 = 0 \qquad (Z = 1) \ . \tag{2.61}$$

We now assume that the dominant balance in the longitudinal momentum equation (2.56) involves friction and gravity. Since perturbations of free surface elevation relative to the still water level are $O(\epsilon)$, we set:

$$\frac{\gamma\epsilon}{\mathcal{F}^2} = \beta C_{f0} \ . \tag{2.62}$$

The conditions (2.53, 2.62) determine the velocity scale V_0^* in the form:

$$V_0^* = \left(\frac{g a_0^{*2} \omega}{C_{f0}} \right)^{1/3} . \tag{2.63}$$

The length scale L^* is then readily obtained from (2.54). We also assume that local inertia is negligible at leading order. Comparison between the orders of magnitude of gravity and local inertia in the momentum equation (2.56) shows that this assumption is valid provided the following condition is satisfied:

$$\mathcal{F}^2 \ll \epsilon^2 . \tag{2.64}$$

As discussed by Lanzoni & Seminara (1998) the latter condition is approximately satisfied by strongly dissipative estuaries. Under the above hypotheses the system (2.56-2.57) admits of the simplest lowest order solution:

$$U_0 = \bar{\mathrm{U}}_0(t,\xi) F_0(Z) , \tag{2.65}$$

$$W_0 = \bar{\mathrm{U}}_0(t,\xi) G_0(Z) , \tag{2.66}$$

$$(H, D) = [H_0, D_0] + \epsilon \left[H_1(\xi,t), D_1(\xi,t) \right] , \tag{2.67}$$

$$\nu_T = \mathcal{N}(Z) |\bar{\mathrm{U}}_0(\xi,t)| D_0 . \tag{2.68}$$

Substituting from (2.65-2.68) into (2.56), where inertial terms are neglected, at the lowest order of approximation we obtain:

$$\bar{\mathrm{U}}_0 |\bar{\mathrm{U}}_0| \frac{d}{dZ} \left[\mathcal{N}(Z) \frac{dF_0}{dZ} \right] = \left(\frac{\gamma \epsilon}{\mathcal{F}^2 \beta \sqrt{C_{f0}}} \right) D_0 \frac{\partial H_1}{\partial \xi} = \sqrt{C_{f0}} D_0 \frac{\partial H_1}{\partial \xi} . \tag{2.69}$$

Recalling the boundary condition (2.60), equation (2.69) can be integrated once to give:

$$-\bar{\mathrm{U}}_0 |\bar{\mathrm{U}}_0| \left(\mathcal{N}(Z) \frac{dF_0}{dZ} \right) \Big|_{Z_0} = D_0 \frac{\partial H_1}{\partial \xi} \sqrt{C_{f0}} . \tag{2.70}$$

Recalling that, by definition, $(\mathcal{N}(Z) dF_0/dZ)|_{Z_0}$ is equal to $\sqrt{C_{f0}}$, from (2.70) we find:

$$D_0 \frac{\partial H_1}{\partial \xi} + \bar{\mathrm{U}}_0 |\bar{\mathrm{U}}_0| = 0 . \tag{2.71}$$

The latter equation is the lowest order approximation of the one dimensional formulation of the momentum equation arising in the present framework.

The continuity equation (2.57) at lowest order reads

$$\frac{\partial U_0}{\partial \xi} + \frac{(1-Z)}{D_0}\frac{\partial D_0}{\partial \xi}\frac{\partial U_0}{\partial Z} + \frac{1}{D_0}\frac{\partial W_0}{\partial Z} = 0 \ , \tag{2.72}$$

which may be integrated at once, with the boundary condition (2.59b), to give:

$$W_0|_{Z=1} + \frac{\partial}{\partial \xi}(\bar{\mathrm{U}}_0 D_0) = 0 \ . \tag{2.73}$$

The quantity $W_0|_{Z=1}$ is obtained from the lowest order approximation of the boundary condition (2.61) and is equal to $\partial H_1/\partial t$; hence (2.73) reduces to the classical one-dimensional form of the continuity equation

$$\frac{\partial H_1}{\partial t} + \frac{\partial}{\partial \xi}(\bar{\mathrm{U}}_0 D_0) = 0 \ . \tag{2.74}$$

The vertical structure of W_0, i.e. the function $G_0(Z)$, is then obtained by integrating (2.72).

The system of equations (2.71, 2.74) can be readily solved (Lanzoni & Seminara, 1998) in the fully nonlinear case. However note that at the lowest order of approximation the basic flow 'felt' by a meander wavelength is spatially uniform, i.e. purely time dependent. More precisely the quantity H_1 does not enter the analysis. We may choose the local average flow depth as reference depth, hence, employing the average bottom elevation as reference elevation in the reach under consideration, we may write

$$D_0 = 1 \ , \tag{2.75}$$

$$H_0 = 1 \ , \tag{2.76}$$

and expand:

$$\bar{\mathrm{U}}_0 = \bar{\mathrm{U}}_0(t)[1 + O(\gamma)] \ . \tag{2.77}$$

Finally, using (2.45), one can show that, at leading order, bottom elevation follows periodic oscillations around a flat equilibrium state with dimensionless amplitudes of order $(W_s^* \mathcal{C}/\omega D_0^*)$ which may attain values ranging about 10^{-4}, small enough to be safely ignored.

The differential problem for F_0 is readily found employing (2.70, 2.71, 2.59a, 2.60). We find:

$$\frac{d}{dZ}\left[\mathcal{N}(Z)\frac{dF_0}{dZ}\right] = -\sqrt{C_{f0}} \ , \tag{2.78}$$

$$F_0 = 0 \qquad (Z = Z_0)\,, \tag{2.79}$$

$$\frac{dF_0}{dZ} = 0 \qquad (Z = 1)\,. \tag{2.80}$$

Using Dean's (1974) structure for $\mathcal{N}(Z)$

$$\mathcal{N}(Z) = \frac{kZ(1-Z)}{1 + 2AZ^2 + 3BZ^3}\,, \qquad A = 1.84\,, \qquad B = -1.56\,, \tag{2.81a-c}$$

with k von Karman constant, we can integrate (2.78), with the boundary conditions (2.79-2.80), to obtain

$$F_0(Z) = \frac{\sqrt{C_{f0}}}{k}\left[\ln\frac{Z}{Z_0} + AZ^2 + BZ^3\right] \tag{2.82}$$

where Z_0 is found by imposing $\int_{Z_0}^{1} F_0(Z)dZ = 1$. It follows:

$$Z_0 = \exp\left(-\frac{k}{\sqrt{C_{f0}}} - 0.777\right)\,. \tag{2.83}$$

Note that the reference friction coefficient C_{f0} refers to the time when $\bar{\mathrm{U}}_0$ equals 1.

We point out that the self similar structure of the solution for U_0 is only valid provided local inertia in the momentum equation is negligible at the leading order of approximation. Otherwise, the vertical distribution F_0 is itself time-dependent. The role played by the non self-similar structure of the basic velocity field observed in real estuaries seems to be fairly weak. Therefore the present analysis is not likely to be significantly affected by such additional effect. A complete analysis will be required in order to conclusively substantiate the latter statement.

Also note that, in principle, any time dependence of the basic flow can be incorporated in the analysis through the function $\bar{\mathrm{U}}_0(t)$. In particular one could readily account for the effect of overtides. For the sake of simplicity the analysis presented in the next section will be developed for the simple case

$$\bar{\mathrm{U}}_0 = \cos(t) \tag{2.84}$$

At the lowest order of approximation considered herein the structure of the basic concentration field $\mathcal{C}_0$ is readily obtained from (2.43) and (2.23-2.24). Recalling (2.26) we find:

$$\psi = \psi_0 = \Psi(Z)|\bar{\mathrm{U}}_0(t)|\,. \tag{2.85}$$

Hence, the following differential problem for $\mathcal{C}_0$ is obtained

$$\left[\frac{\partial}{\partial Z}\left(\Psi(Z)\frac{\partial}{\partial Z}\right) + G(t)\frac{\partial}{\partial Z}\right]\mathcal{C}_0 = 0\ , \tag{2.86}$$

$$\Psi(Z)\frac{\partial \mathcal{C}_0}{\partial Z} + G(t)\mathcal{C}_{e0} = 0 \qquad (Z = a_r)\ , \tag{2.87}$$

$$\Psi(Z)\frac{\partial \mathcal{C}_0}{\partial Z} + G(t)\mathcal{C}_0 = 0 \qquad (Z = 1)\ , \tag{2.88}$$

where $\mathcal{C}_{e0} = \mathcal{C}_e\,|_{\theta=\theta_0}$, with

$$\theta_0 = \bar{\mathrm{U}}_0^2 \frac{C_{f0} V_0^{*2}}{(s-1)\mathrm{g}d_s^*}\ , \tag{2.89}$$

and

$$G(t) = \frac{W_s}{|\bar{\mathrm{U}}_0|\sqrt{C_{f0}}}\ . \tag{2.90}$$

The solution of the latter system is obtained in the form

$$\mathcal{C}_0 = \mathcal{C}_{e0}\exp\left[-\int_{a_r}^{Z}\frac{G(t)}{\Psi(Z)}dZ\right] \tag{2.91}$$

and describes a Rouse type distribution parametrically dependent on time.

2.5 Linear solution

The solutions for the flow field and the bottom topography is sought in the case of weakly meandering channel, therefore we set:

$$\nu \ll 1\ . \tag{2.92}$$

Note that such condition is appropriate to describe the typical meandering configurations observed in nature.

In fact table 1 shows the values of ν calculated for each bend of the sequences corresponding to the tidal channels depicted in Fig. 2 (Barnstable 1, Petaluma 1, Pagliaga 1) and of some tributary channels (Barnstable 2 and 3, Petaluma 2, Pagliaga 2, 3) corresponding to different tidal environments. It

	Bar. 1	Bar. 2	Bar. 3	Pet. 1	Pet. 2	Pag. 1	Pag. 2	Pag. 3
Mean of ν	0.01	0.06	0.03	0.16	0.17	0.12	0.19	0.18
Max of ν	0.05	0.30	0.23	0.64	1.14	1.05	1.27	1.26

Table 2.1: The mean and the maximum values of ν for tidal meanders located in three distinct environments (Barnstable (MA, USA), Petaluma (CA, USA) and Pagliaga (Venezia, Italy))

appears that the average value of ν ranges between 0.01 and 0.19. A linear theory of the type developed herein is then generally appropriate to investigate fully developed natural meanders. Besides, it may be set as the basis for an investigation of the mechanism of formation of tidal meanders, based on a linear analysis of the planimetric instability of tidal channels, as discussed in section 2.7.

Taking advantage of such assumption, we expand the solution in powers of the small parameter ν in a neighborhood of the basic state as follows:

$$\begin{aligned}(U,V,W,H,D) &= (\bar{\mathrm{U}}_0(t)F_0(Z),0,0,H_0(s),H_0(s)) \\ &+ \nu(u,v,w,\mathcal{F}^2h,d)+O(\nu^2)\ , \end{aligned} \tag{2.93}$$

where $H_0(s)$ is the free surface elevation associated with the basic tidal wave described in sect. 2.4. Moreover the perturbations u, v, w, h, d are functions of the independent variables s, n, Z, t and are also parametrically dependent on the slow spatial variable ξ describing the spatial distribution of the basic tidal motion (sect. 2.4), though the latter dependence will not be considered herein. Note that we have assumed the reference level for the vertical coordinate to coincide with the average bottom elevation within the meander reach under investigation.
Similarly we expand the operators q_s, q_n, L and the eddy viscosity ν_T in powers of ν in the form:

$$(q_s,q_n,L,\nu_T)=(q_{s0},q_{n0},\mathcal{L}_0,\nu_{T0})+\nu(q_{s1},q_{n1},\mathcal{L}_1,\nu_{T1})+O(\nu^2)\ , \tag{2.94}$$

where

$$q_{s0}=\frac{\partial}{\partial s}\ ,\ q_{n0}=\frac{\partial}{\partial n}\ ,\mathcal{L}_0=U_0\frac{\partial}{\partial s}\ ,\ \nu_{T0}=|\bar{\mathrm{U}}_0(t)|\mathcal{N}(Z)\ , \qquad (2.95a-d)$$

$$q_{s1} = \left[(1-Z)\frac{\partial d}{\partial s} - \mathcal{F}^2\frac{\partial h}{\partial s}\right]\frac{\partial}{\partial Z}\,, \tag{2.96}$$

$$q_{n1} = \left[(1-Z)\frac{\partial d}{\partial n} - \mathcal{F}^2\frac{\partial h}{\partial n}\right]\frac{\partial}{\partial Z}\,, \tag{2.97}$$

$$\mathcal{L}_1 = U_0 q_{s1} + (u - nc(s)U_0)q_{s0} + w\frac{\partial}{\partial Z} + v\frac{\partial}{\partial n}\,, \tag{2.98}$$

$$\nu_{T1} = \nu_{T0}\left(d + \left.\frac{\frac{\partial u}{\partial Z}}{\frac{\partial U_0}{\partial Z}}\right|_{Z_0}\right)\,. \tag{2.99}$$

Note that in equation (2.95c) local inertial effects have been neglected. Such assumption is justified by the smallness of the parameter σ_0 (see discussion reported in section 2.4). The derivation of the expansion (2.99) is given in 2.5.1. By substituting from (2.94-2.99) into the governing hydrodynamic equations (2.36-2.38) and the associated boundary conditions (2.40-2.42) and equating terms proportional to ν^o we recover the governing equation for the basic longitudinal velocity already discussed in section 2.4.

Proceeding to $O(\nu)$ we derive the linearized form of the differential problem governing the dynamics of flow perturbations. It reads:

$$\beta\sqrt{C_{f0}}\frac{\partial\left(\nu_{T0}\frac{\partial u}{\partial Z}\right)}{\partial Z} - U_0\frac{\partial u}{\partial s} - \beta\sqrt{C_{f0}}\mathcal{N}(Z_0)|\bar{\mathrm{U}}_0(t)|\frac{\partial u}{\partial Z}|_{Z_0} =$$

$$= \frac{\partial h}{\partial s} - \frac{n}{\mathcal{F}^2}\frac{\partial H_0}{\partial s} + \frac{\partial U_0}{\partial Z}w - \beta C_{f0}\bar{\mathrm{U}}_0(t)|\bar{\mathrm{U}}_0(t)|d + U_0\frac{\partial U_0}{\partial Z}(1-Z)\frac{\partial d}{\partial s}\,, \tag{2.100}$$

$$\beta\sqrt{C_{f0}}\frac{\partial(\nu_{T0}\frac{\partial v}{\partial Z})}{\partial Z} - U_0\frac{\partial v}{\partial s} = \frac{\partial h}{\partial n} - c(s)U_0^2\,, \tag{2.101}$$

$$\frac{\partial u}{\partial s} + \frac{\partial v}{\partial n} + \frac{\partial w}{\partial Z} = -(1-Z)\frac{\partial U_0}{\partial Z}\frac{\partial d}{\partial s}\,, \tag{2.102}$$

$$u = v = w = 0 \qquad (Z = Z_0)\,, \tag{2.103a-c}$$

$$\frac{\partial u}{\partial Z} = \frac{\partial v}{\partial Z} = w = 0 \qquad (Z = 1)\,, \tag{2.104a-c}$$

having neglected terms of order $\mathcal{F}^2$ with respect to $O(1)$ terms. Also note that the bed of tidal channels is typically dune covered, hence variations of the friction coefficient are dominantly associated with variations of the Shields

parameter (recall the discussion at the beginning of section 2.6). Variations of the friction coefficient due to the effect of the small perturbation of flow depth, though formally of order ν, are fairly small and have been neglected in eq. (2.100, 2.101).
The latter differential system can be solved by setting the following expansions:

$$(u, w, h, d) = \left\{ \left(0, 0, \overline{h}n, \overline{d}n\right) + \right.$$
$$\left. + \sum_{m=1}^{\infty} \left[u_m(Z,t), w_m(Z,t), h_m(t), d_m(t)\right] \sin(Mn) \right\} \exp(i\lambda s) + c.c. , \qquad (2.105)$$

$$v = \left\{ v_0(Z,t) + \left[\sum_{m=1}^{\infty} v_m(Z,t) \cos(Mn) \right] \right\} \exp(i\lambda s) + c.c. , \qquad (2.106)$$

where $\overline{h}$ and $\overline{d}$ are parameters to be determined and M is the following parameter:

$$M \equiv \frac{\pi}{2}(2m-1) \qquad\qquad (m = 1, 2, 3....) . \qquad (2.107)$$

The structure of the above expansions arise as follows. If the channel had constant curvature and the flow were fully developed, only the zero depth-average contribution (*centrifugal contribution*) would arise in (2.105, 2.106): in this case no derivative in s appears in equations (2.100- 2.102) and the secondary flow arises from the need to balance the difference between centrifugal forces (increasing in the vertical direction) and lateral pressure gradient (constant in the vertical direction). In a linear context this leads to lateral distributions of both flow depth and free surface elevation which are linear in the lateral coordinate n and to a lateral component of velocity which is independent of n (except for the side wall boundary layers ignored in this analysis) and has vanishing depth average. This is the case treated in the fluvial environment by Engelund, 1974 and later by several authors, including Kalkwijk and de Vriend, 1980.

In the presence of longitudinal variations of channel curvature, a centrifugal contribution to secondary flow still exists, of course, but it cannot be self balanced, unless the meander wavenumber is so small that the flow can be considered as fully developed at any cross section. This is the first term appearing in (2.105, 2.106). However, a *topographic* component of the secondary flow with non vanishing depth average now arises (the series in

(2.105, 2.106)) to balance the equations. In fact the centrifugal term satisfies the n- component of the momentum equation exactly but it leaves the flow continuity equation and the s- momentum equation unbalanced (a topographic effect), hence the term ($\overline{d}nexp(i\lambda s)$) becomes a forcing term for both equations. The decomposition is useful, both *mathematically* because subtracting the centrifugal component leaves us with homogeneous conditions at the side walls (hence allowing the Fourier expansion of the remaining topographic component), and *physically* because it allows to distinguish the two mechanisms (centrifugal versus topographic) controlling the establishment of a secondary flow and of the perturbed bottom topography.

Note that such a decomposition is similar to that proposed originally by Kalkwijk and de Vriend (1980) in the fluvial case, though the latter authors assumed a vertical structure of the topographic component of the secondary flow, which is not assumed but formally derived here.
The problem for v_0 is readily solved in the form:

$$v_0 = |\bar{\mathrm{U}}_0(t)| \quad \mathcal{G}(Z;I)\,, \tag{2.108}$$

$$\overline{h} = \bar{\mathrm{U}}_0^2(t) \quad \mathcal{H}\,, \tag{2.109}$$

where I reads:

$$I = \frac{\bar{\mathrm{U}}_0}{|\bar{\mathrm{U}}_0|}\,, \tag{2.110}$$

and the function $\mathcal{G}$ is the solution of the ordinary differential problem:

$$L_1\mathcal{G} = -\frac{1}{\beta\sqrt{C_{f0}}}[-\mathcal{H} + F_0^2(Z)]\,, \tag{2.111}$$

$$\mathcal{G} = 0 \qquad (Z = Z_0)\,, \tag{2.112}$$

$$\frac{\partial\mathcal{G}}{\partial Z} = 0 \qquad (Z = 1)\,. \tag{2.113}$$

Moreover the differential operator L_1 reads

$$L_1 \equiv \frac{\partial}{\partial Z}\left(\mathcal{N}\frac{\partial}{\partial Z}\right) - \Lambda I F_0\,, \tag{2.114}$$

and

$$\Lambda = \frac{i\lambda}{\beta_0\sqrt{C_{f0}}}\,, \tag{2.115}$$

while the constant $\mathcal{H}$ is obtained by requiring that the solution for $\mathcal{G}$ satisfies the following integral condition:

$$\int_{Z_0}^{1} \mathcal{G}(Z) dZ = 0 \ . \tag{2.116}$$

Such condition reinforces the constraint of vanishing flux through the side walls. Note that (2.108) suggests that the centrifugally induced component of the secondary flow is identical in the flood and ebb phases. This is not surprising as the symmetry of the geometric configuration and of the basic longitudinal flow implies that the driving forces are perfectly symmetrical both in space and in time. The non linearity of the temporal dependence of the driving force is responsible for the generation of a non linear response of the secondary flow which emerges both in (2.108) and in (2.109). Residual terms are associated with such non linear character and may be interpreted as though the response to the oscillatory basic state includes a steady component of 'fluvial' type. The system (2.111-2.113) is readily solved by shooting techniques. In particular the function $\mathcal{G}$ can be written in the form:

$$\beta \sqrt{C_{f0}} \mathcal{G} = \mathcal{H} \left[\frac{g_2'|_1}{g_1'|_1} g_1(Z) - g_2(Z) \right] + g_3(Z) - \frac{g_3'|_1}{g_1'|_1} g_1(Z) \tag{2.117}$$

where $g_j(Z) (j = 1, 2, 3)$ are the solutions of the following initial value problems:

$$L_1 g_j = b_j \qquad (j = 1, 2, 3) \ , \tag{2.118}$$

$$g_j = 0 \quad (Z = Z_0) \qquad (j = 1, 2, 3) \ , \tag{2.119}$$

$$g_j' = 1 \quad (Z = Z_0) \qquad (j = 1, 2, 3) \ , \tag{2.120}$$

with

$$b_1 = 0, \qquad b_2 = 1, \qquad b_3 = -F_0^2(Z) \ . \tag{2.121}$$

and L_1 is the differential operator obtained from (2.114) replacing $\partial/\partial Z$ by d/dZ (hereinafter the latter derivative is denoted with an apex). The latter problems are readily solved numerically.
The constant $\mathcal{H}$ is obtained from the integral constraint (2.116) and reads:

$$\mathcal{H} = \frac{g_3'|_1 \Im_{g_1} - g_1'|_1 \Im_{g_3}}{g_2'|_1 \Im_{g_1} - g_1'|_1 \Im_{g_2}} \tag{2.122}$$

with $\Im$ the integral operator defined as follows:

$$\Im = \int_{Z_0}^{1} f(\tau) d\tau \ . \tag{2.123}$$

Similarly the problem for $(v_m, h_m; m = 1, 2, 3, ...)$ is solved in the form:

$$h_m = |\bar{\mathrm{U}}_0(t)| \mathcal{H}_m \ , \tag{2.124}$$

$$v_m = \mu \mathcal{H}_m \mathcal{G}_m(Z; I) \ , \tag{2.125}$$

with $\mathcal{H}_m$ functions of time to be determined and the functions $\mathcal{G}_m (m = 1, 2, 3, ...)$ are solutions of the following ordinary differential problem (parametrically dependent on time):

$$L_1 \mathcal{G}_m = 1 \ , \tag{2.126}$$

$$\mathcal{G}_m = 0 \qquad (Z = Z_0) \ , \tag{2.127}$$

$$\frac{\partial \mathcal{G}_m}{\partial Z} = 0 \qquad (Z = 1) \ , \tag{2.128}$$

with

$$\mu = \frac{M}{\beta_0 \sqrt{C_{f0}}} \ . \tag{2.129}$$

Such solutions are straightforward and read:

$$v_m = -\mu \mathcal{H}_m \left[\frac{g_2'|_1}{g_1'|_1} g_1(Z) - g_2(Z) \right] \tag{2.130}$$

Having determined v_0 and v_m we can proceed to express w_m in terms of u_m and v_m using the continuity equation (2.102). We find:

$$w_m = M \int_{Z_0}^{Z} v_m(\xi) d\xi - i\lambda \int_{Z_0}^{Z} u_m(\xi) d\xi +$$

$$-(A_m \overline{d} + d_m) i\lambda \bar{\mathrm{U}}_0(t) \left[F_0(1 - Z) + \int_{Z_0}^{Z} F_0(\xi) d\xi \right] \ , \tag{2.131}$$

where $A_m (m = 1, 2, 3, ...)$ are constants which read:

$$A_m = -(-1)^m \frac{2}{M^2} \ . \tag{2.132}$$

We may then derive the differential equation for u_m by substituting from (2.105, 2.106) into (2.100) and using the structure of the solution obtained for the secondary flow. With the help of some algebraic manipulations and of the following definition:

$$f = \int_{Z_0}^{Z} u_m d\xi \,, \tag{2.133}$$

we eventually derive the following structure of the solution for the function f:

$$f = \sum_{j=1}^{3} \varphi_j \phi_j \,, \tag{2.134}$$

with

$$\phi_j = \left(f_j - \left. \frac{\frac{\partial^2 f_j}{\partial Z^2}}{\frac{\partial^2 f_0}{\partial Z^2}} \right|_{Z=1} f_0 \right) \qquad (j = 1, 2, 3) \,, \tag{2.135}$$

and the functions $\varphi_j (j = 1, 2, 3)$ read:

$$\begin{aligned} \varphi_1 &= \Lambda \left[A_m \mathcal{H} |\bar{\mathrm{U}}_0(t)| + \mathcal{H}_m \right] - \sqrt{C_{f0}} \bar{\mathrm{U}}_0(t) (A_m \overline{d} + d_m) + \\ &+ \sqrt{C_{f0}} \bar{\mathrm{U}}_0(t) A_m \,, & (2.136) \\ \varphi_2 &= -\Lambda |\bar{\mathrm{U}}_0(t)| (A_m \overline{d} + d_m) \,, & (2.137) \\ \varphi_3 &= \frac{M^2}{\beta_0 \sqrt{C_{f0}}} I \mathcal{H}_m \,. & (2.138) \end{aligned}$$

Moreover the functions $f_j (j = 0, 1, 2, 3)$ are solutions of the ordinary differential problems

$$\begin{aligned} L_2 f_j &= a_j & (j = 0, 1, 2) \,, & (2.139) \\ f_j = f_j' &= 0 & (Z = Z_0,\ j = 0, 1, 2) \,, & (2.140) \\ f_j'' &= 1 & (Z = Z_0,\ j = 0, 1, 2) \,, & (2.141) \end{aligned}$$

with

$$L_2 \equiv \frac{\partial}{\partial Z} \left(\mathcal{N} \frac{\partial^2}{\partial Z^2} \right) - \Lambda F_0 I \frac{\partial}{\partial Z} + \Lambda F_0' I - \left[\mathcal{N} \frac{\partial^2}{\partial Z^2} \right]_{Z_0} \,. \tag{2.142}$$

and $a_j (j = 0, 1, 2, 3)$ defined as follows

$$a_0 = 0 \,, \quad a_1 = 1 \,, \quad a_2 = F_0' \int_{Z_0}^{Z} F_0(\xi) d\xi, \quad a_3 = F_0' \Gamma \quad (2.143 a - d)$$

and

$$\Gamma = \int_{Z_0}^{Z} \mathcal{G}_m(\xi) d\xi \ . \tag{2.144}$$

We finally impose the kinematic condition at the free surface (2.104c) which, with the help of (2.125, 2.131, 2.133) and some algebraic manipulations, eventually leads to the following relationship between the quantities $\mathcal{H}_m$ and d_m for each m:

$$\mathcal{H}_m = \overline{h}_1 |\bar{\mathrm{U}}_0(t)| \mathcal{H} + \overline{h}_2 \bar{\mathrm{U}}_0(t)(A_m \overline{d} + d_m) + \overline{h}_3 \bar{\mathrm{U}}_0(t) A_m \ , \tag{2.145}$$

where $\overline{h}_1$, $\overline{h}_2$ and $\overline{h}_3$ read:

$$\overline{h}_1 = \Lambda^{\,2} \phi_1|_1 A_m \left[\Gamma \mu M - \Lambda^{\,2} \phi_1|_1 - \Lambda \mu M I \phi_3|_1 \right]^{-1} \ , \tag{2.146}$$

$$\overline{h}_2 = \overline{h}_1 \left[1 - \sqrt{C_{f0}} \phi_1|_1 - \Lambda I \phi_2|_1 \right] / (\Lambda \phi_1|_1 A_m) \ , \tag{2.147}$$

$$\overline{h}_3 = \overline{h}_1 \sqrt{C_{f0}} / (\Lambda A_m) \ , \tag{2.148}$$

having used the definitions (2.115, 2.110, 2.144) for Λ, I and Γ.

The reader will note that, through the relationship (2.145), the whole solution for the flow perturbations is linearly related to the quantity $(A_m \overline{d} + d_m)(m = 1, 2, 3, ...)$. It is then convenient to express the solution for the velocity perturbations in the form:

$$(u_m, v_m, w_m) = (\hat{u}_1, \hat{v}_1, \hat{w}_1) + (\hat{u}_2, \hat{v}_2, \hat{w}_2)(A_m \overline{d} + d_m) \quad (m = 1, 2, 3, ...) \ , \tag{2.149}$$

where $\hat{u}_i, \hat{v}_i, \hat{w}_i \quad (i = 1, 2)$ are functions of the independent variables Z and t. The structure (2.149) of the solution for (u_m, v_m, w_m) has a simple physical explanation. In fact, part of such solution $(\hat{u}_1, \hat{v}_1, \hat{w}_1)$ is independent of the development of bottom perturbations being driven by the forcing effect of centrifugally driven longitudinal slope of the free surface (term proportional to $\mathcal{H}$ in (2.136)) and by the metric variation of the longitudinal slope (second term in the right hand side of (2.100) which gives rise to the third term in the right hand side of (2.136)). Part of the solution of (2.149) is induced by perturbations of bottom topography, either centrifugally driven (terms proportional to $\overline{d}$ in (2.136) and (2.137)) or due to shoaling effects (terms proportional to d_m in (2.136, 2.137, 2.138)). The as yet unknown quantities $\overline{d}$ and d_m will be determined below by imposing the constraints required by sediment continuity. Also note that the relationship (2.145) does not exhibit any discontinuity at the instant of flow reversal.

Let us finally proceed to calculate the perturbation of the concentration field. Hence, we set the following expansion for the concentration $\mathcal{C}$ and the eddy diffusivity ψ in powers of the small parameter ν:

$$(\mathcal{C},\psi) = (\mathcal{C}_0,\psi_0) +$$

$$+\nu\left\{\left[\sum_{m=1}^{\infty}(\mathcal{C}_m(Z,t),\psi_m(Z,t))\sin(Mn)\right]\exp(i\lambda s)+c.c.\right\}\ , \qquad (2.150)$$

where $\mathcal{C}_0$ and ψ_0 are the basic concentration and diffusivity fields obtained in section 2.4. Note that the perturbation ψ_1 of eddy diffusivity is related to the perturbation of the flow field through the following relationship

$$\psi_1 = \psi_0\left(d + \left.\frac{\frac{\partial u}{\partial Z}}{\frac{\partial U_0}{\partial Z}}\right|_{Z_0}\right)\ . \qquad (2.151)$$

Expanding u and d according to (2.105) one readily derives from (2.151) expressions for the amplitude $\psi_m(Z,t)$ appearing in (2.150). By substituting from the expansion (2.150) into the convection-diffusion equation (2.43) and the boundary condition (2.23- 2.24), employing the expression (2.149) and equating terms $O(\nu)$ we find the following differential system:

$$L_3\mathcal{C}_m = \omega_{01}(Z,t) + \omega_{02}(Z,t)(A_m\overline{d} + d_m)\ , \qquad (2.152)$$

$$\left[\Psi C_{m,Z} + G\mathcal{C}_m\right]_{Z=1} = \omega_{11}(t) + \omega_{12}(t)(A_m\overline{d} + d_m)\ , \qquad (2.153)$$

$$\left[\Psi C_{m,Z}\right]_{Z=a_r} = \omega_{21}(t) + \omega_{22}(t)(A_m\overline{d} + d_m)\ . \qquad (2.154)$$

where L_3 is the following differential operator

$$L_3 \equiv \frac{\partial Z}{\partial}\left(\Psi\frac{\partial}{\partial Z}\right) - \Lambda I F_0 + G(t)\frac{\partial}{\partial Z} \qquad (2.155)$$

Note that Ψ is the function describing the vertical distribution of eddy diffusivity at equilibrium defined in (2.26) and (5.4 I). The functions $\omega_{0i}(Z,t)$ in (2.152) reads

$$\omega_{0i} = \left\{\frac{\hat{u}_i I}{\bar{\mathrm{U}}_0(t)\beta_0\sqrt{C_{f0}}} + \Lambda I F_0(1-Z) + G(\xi,t)\Gamma\right\}\frac{\partial\mathcal{C}_0}{\partial Z}\ , \qquad (2.156)$$

where

$$\Gamma = \left(\frac{\hat{u}_i'}{\bar{\mathrm{U}}_0(t) F_0'} \right)_{Z=Z_0} . \tag{2.157}$$

The functions $\omega_{1i}(t)$ in (2.153) are

$$\omega_{1i} = G \Gamma \mathcal{C}_0|_{Z=1} . \tag{2.158}$$

Moreover $\omega_{2i}(t)$ in (2.154) $(i = 1, 2)$ reads

$$\omega_{2i} = G \left[-2\theta_0 \left. \frac{d\mathcal{C}_e}{d\theta} \right|_{\theta_0,1} + \mathcal{C}_{e0} \right] \Gamma + I F_0|_{Z=a_r} \Lambda \mathcal{C}_{e0} +$$

$$+ I \frac{\hat{w}_i|_{Z=a_r}}{\bar{\mathrm{U}}_0(t) \beta \sqrt{C_{f0}}} \mathcal{C}_{e0} - G \left. \frac{d\mathcal{C}_e}{dD} \right|_{\theta_0,1} . \tag{2.159}$$

Note that the effect of the centrifugally induced secondary flow is only indirectly present through the forcing effect of $\overline{d}$ in the system (2.152- 2.154); no direct effect can be present as the term $v \frac{\partial \mathcal{C}}{\partial n}$ in the convection-diffusion equation only enters at $O(\nu^2)$. Also note that the boundary conditions (2.153, 2.154) account for the effect of perturbation of the reference concentration $\mathcal{C}_e$ due to perturbations of the Shields parameter θ and of the local flow depth D. Finally note that the decomposition (2.149) for the velocity field drives, through convective terms, an analogous decomposition of the forcing terms in (2.152-2.154) and, hence, of the solution, for $\mathcal{C}_m$. In fact the solution of the differential system (2.152-2.154) is readily obtained in the form:

$$\mathcal{C}_m = \hat{\mathcal{C}}_1(Z, t) + \hat{\mathcal{C}}_2(Z, t)(A_m \overline{d} + d_m) , \tag{2.160}$$

where

$$\hat{\mathcal{C}}_j = c_j k_{j1} + k_{j2} \qquad (j = 1, 2) , \tag{2.161}$$

The functions $k_{ij} (i = 1, 2; j = 1, 2)$ satisfy the following differential problem:

$$L_3 k_{ij} = r_{ij} \tag{2.162}$$

$$\Psi \frac{\partial k_{ij}}{\partial Z}|_{Z=a_r} = e_{ij} , \tag{2.163}$$

$$k_{ij}|_{Z=a_r} = \ell_{ij} , \tag{2.164}$$

where

$$r_{i1} = 0 \ , \ \ e_{i1} = 0 \ , \ \ \ell_{i1} = 1 \ \ (i = 1, 2) \ , \tag{2.165}$$

$$r_{i2} = \omega_{0i} \ , \ \ e_{i2} = \omega_{2i} \ , \ \ \ell_{i2} = 0 \ \ (i = 1, 2) \ , \tag{2.166}$$

Furthermore the constants $c_i (i = 1, 2)$ are found to read:

$$c_i = \frac{\omega_{1i} - [\Psi \frac{\partial k_{i2}}{\partial Z} + G k_{i2}]_{Z=1}}{[\Psi \frac{\partial k_{i1}}{\partial Z} + G K_{i1}]_{Z=1}} \ . \tag{2.167}$$

Let us then linearize and solve the sediment continuity equation along with the boundary condition of vanishing sediment flux through the side walls. To this aim we substitute from the expansions (2.105, 2.106, 2.150) and the expressions (2.149), (2.160) into the relationships (2.27, 2.28). Some tedious algebraic work eventually leads to the solution for the as yet unknown function $\overline{d}$ which reads:

$$\overline{d} = -\frac{\beta\sqrt{\theta}_0}{r Q_0 \phi_{b0}} \left[|\bar{\mathrm{U}}_0(t)| \int_{a_r}^1 \mathcal{C}_0 \mathcal{G} dZ + Q_0 \phi_{b0} \left. \frac{\frac{\partial \mathcal{G}}{\partial Z}}{F_0'} \right|_{Z_0} \right] \ . \tag{2.168}$$

Finally the functions $d_m (m = 1, 2, 3, ...)$ satisfy the following equations:

$$(s_1 - \frac{r M^2}{\beta\sqrt{\theta}_0}) d_m = -(s_2 + s_1 A_m \overline{d}) \ , \tag{2.169}$$

where

$$\begin{aligned} s_1 \ &= \ i\lambda \left[\frac{1}{Q_0 \phi_{b0}} \left(\bar{\mathrm{U}}_0(t) \int_{a_r}^1 \hat{\mathcal{C}}_2 F_0 dZ + \bar{\mathrm{U}}_0(t) \int_{a_r}^1 \mathcal{C}_0 F_0 dZ + \int_{a_r}^1 \mathcal{C}_0 \hat{u}_2 dZ \right) \right] + \\ &+ \ \left. \frac{2\phi_\theta \frac{\partial \hat{u}_2}{\partial Z}}{\bar{\mathrm{U}}_0(t) F_0'} \right|_{Z_0} + \frac{r M^2}{\beta\sqrt{\theta}_0} |\bar{\mathrm{U}}_0(t)| \bar{\mathrm{U}}_0(t) \overline{h}_2 + \\ &- \ \frac{M}{Q_0 \phi_{b0}} \int_{a_r}^1 \mathcal{C}_0 \hat{v}_2 dZ - \left. \frac{M \frac{\partial \hat{v}_2}{\partial Z}}{|\bar{\mathrm{U}}_0(t)| F_0'} \right|_{Z_0} \ , \end{aligned} \tag{2.170}$$

$$s_2 \ = \ i\lambda \left[\frac{1}{Q_0 \phi_{b0}} \left(\bar{\mathrm{U}}_0(t) \int_{a_r}^1 \hat{\mathcal{C}}_1 F_0 dZ + \int_{a_r}^1 \mathcal{C}_0 \hat{u}_1 dZ \right) \right] +$$

$$+ \quad \left. \frac{2\phi_\theta \frac{\partial \hat{u}_1}{\partial Z}}{\bar{\mathrm{U}}_0(t) F_0'} \right|_{Z_0} + \frac{r M^2}{\beta \sqrt{\theta}_0} \bar{\mathrm{U}}_0(t) \left(\bar{\mathrm{U}}_0(t) \overline{h}_1 \mathcal{H} + |\bar{\mathrm{U}}_0(t)| A_m \overline{h}_3 \right) +$$

$$- \quad \frac{M}{Q_0 \phi_{b0}} \int_{a_r}^{1} \mathcal{C}_0 \hat{v}_1 dZ - \left. \frac{M \frac{\partial \hat{v}_1}{\partial Z}}{|\bar{\mathrm{U}}_0(t)| F_0'} \right|_{Z_0} , \tag{2.171}$$

having set

$$\phi_{b0} = \phi_b(\theta_0) , \tag{2.172}$$

$$\phi_\theta = \left. \frac{\theta_0}{\phi_{b0}} \frac{d\phi_b}{d\theta} \right|_{\theta_0} . \tag{2.173}$$

The equation (2.169) is easily solved numerically. Once the quantities $\overline{d}$ and $d_m (m = 1, 2, 3, ...)$ are known, the whole solution for the flow and topography fields is completely determined. The reader will note that the complex nature of the function $\mathcal{G}$ in (2.168) and of coefficients s_1 and s_2 in (2.169) suggests that both the 'centrifugally induced' lateral deformation of the bed and the 'topographically induced' component are out of phase relative to channel curvature. The temporal dependence of both components is non linearly related to the basic velocity field.

2.5.1 Linearization of eddy viscosity

In the present subsection we report the procedure we have employed to linearize the eddy viscosity. From (2.18) we have:

$$\nu_T = u_* D \mathcal{N}(Z) \,, \tag{2.174}$$

hence, expanding u_* and D in powers of ν according to (2.93):

$$\nu_T = \nu_{T0} \left[1 + \nu \left(d + \frac{u_{*1}}{u_{*0}} \right) + O(\nu^2) \right] \,. \tag{2.175}$$

An expression for $\frac{u_{*1}}{u_{*0}}$ is readily obtained from the definition:

$$u_*^2 = \frac{T^*_{zs}|_{z_0^*}}{\rho V_0^{*2} C_{f0}} \,, \tag{2.176}$$

where the contribution of $T^*_{zn}|_{z_0^*}$ is ignored, being of order ν^2. From (2.176) we find:

$$u_*^2 = \frac{\nu_T^* \frac{\partial U^*}{\partial z^*}|_{z_0^*}}{V_0^2 C_{f0}} = \nu_T \frac{\partial U}{\partial z}|_{z_0} = \frac{\nu_T}{D} \frac{\partial U}{\partial Z}|_{Z_0} \,. \tag{2.177}$$

Hence, expanding both sides of equation (2.177) in powers of ν

$$\begin{aligned} u_{*0}^2 \left(1 + 2\nu \frac{u_{*1}}{u_{*0}} + O(\nu^2) \right) = \\ = \nu_{T0} \left(1 + \nu \frac{\nu_{T1}}{\nu_{T0}} + O(\nu^2) \right) \left(1 - \nu d + O(\nu^2) \right) \\ \left(\frac{\partial U_0}{\partial Z}|_{Z_0} + \nu \frac{\partial u}{\partial Z}|_{Z_0} + O(\nu^2) \right) \,. \end{aligned} \tag{2.178}$$

Using (2.175) to express $\frac{\nu_{T1}}{\nu_{T0}}$ in (2.178) and equating terms of various orders in ν we finally find:

$$O(\nu^0) \qquad u_{*0}^2 = \nu_{T0} \frac{\partial U_0}{\partial Z}|_{Z_0} \,, \tag{2.179}$$

$$O(\nu^1) \qquad \frac{u_{*1}}{u_{*0}} = \frac{\frac{\partial u}{\partial Z}|_{Z_0}}{\frac{\partial U_0}{\partial Z}|_{Z_0}} \,. \tag{2.180}$$

Substituting from (2.180) into (2.175) we finally recover equation (2.99)

2.6 Results for the flow and topography fields

The basic flow and concentration field and the solution of the linearized problem is obtained once appropriate closure relationships for $\mathcal{C}_e, a_r, \Psi(Z), \phi_b$ and C_{f0} are introduced. To evaluate the friction coefficient C_{f0} we employ the Einstein's (1950) formula in the plane bed regime and Engelund & Hansen's (1967) formula, as modified by Engelund & Fredsøe (1982), in the case of dune-covered bed. Note that we are tacitly assuming that dunes adapt instantaneously to the variation in time of the basic flow field. Such assumption is only approximately true as dunes are known to exhibit a small delay with respect to the variation of the basic flow field.
To evaluate the reference concentration $\mathcal{C}_e$ at the distance a_r^* from the bed we employ van Rijn's (1984) relationships. They read:

$$\begin{aligned} \mathcal{C}_e &= 0.015\frac{d_s^*}{a_r^*}\left(\frac{\theta'}{\theta_c}-1\right)^{1.5} R_p^{-0.2}\,, & \text{(2.181a)}\\ a_r^* &= \epsilon_e \qquad (\epsilon_e \geq 0.01D^*)\,, & \text{(2.181b)}\\ a_r^* &= 0.01D^* \qquad (\epsilon_e < 0.01D^*)\,, & \text{(2.181c)} \end{aligned}$$

where θ' is the effective Shields stress acting on bedload particles, which is expressed in terms of the total Shields parameter θ using Engelund & Fredsøe's (1982) relationship:

$$\theta' = 0.06 + 0.3\theta^{3/2}\,. \tag{2.182}$$

Furthermore, ϵ_e is an effective roughness accounting for the effect of dunes, for which van Rijn (1984) gives expression which ultimately relate ϵ_e to bed shear stress, and θ_c is the critical Shields stress for sediment motion evaluated using Brownlie's (1981) relationship:

$$\theta_c = .22R_p^{-0.6} + 0.06\exp(-17.77)R_p^{-0.6}\,. \tag{2.183}$$

The eddy diffusivity has been given Mc Tigue's (1981) form

$$\begin{aligned} \Psi &= 0.35Z \qquad (Z < 0.314)\,,\\ \Psi &= 0.11 \qquad (0.314 \leq Z \leq 1)\,. \end{aligned} \tag{2.184}$$

The intensity of bed load transport was evaluated using Meyer-Peter & Muller classical relationship:

$$\phi_b = 8(\theta' - \theta_c)^{3/2} \tag{2.185}$$

with θ_c defined in (2.183). The fall velocity W_s^* was obtained employing the following relationship fitting the experimental curve of Parker (1978):

$$\lg_{10}\left(\frac{W_s^*}{\sqrt{(s-1)gd_s^*}}\right) = - 1.181 + 0.966\pi_p - 0.1804\pi_p^2 + + 0.003746\pi_p^3 + 0.0008782\pi_p^4 \,, \quad (2.186)$$

with $\pi_p = \lg_{10} R_p$.

Before discussing the main results obtained in the present work let us provide some information about typical values of physical parameters controlling the morphodynamics of tidal channels. Data concerning typical widths, curvature radii of the channel axis and flow depths have already been given in figures 2.2 and 2.3 referring to three distinct tidal environments. Typical amplitude of flow velocity and of friction coefficient C_{f0} then range about $(0.5-1)$m/s and $(4-2.5)\cdot 10^{-3}$ respectively; a typical grain size may range about 0.1 mm corresponding to a settling velocity of 1 cm/s and a particle Reynolds number about 4 (Danish Hydraulic Institute, 1990). Friction velocity then ranges about $(3-6)$cm/s while the peak Shields stress (see eq. 2.89) attains values around 0.6-1.5. Typical values of the peak reference concentration are then immediately calculated and are found to increase from $4.4\cdot 10^{-5}$ to $9.6\cdot 10^{-5}$ as the Shields stress increases from 0.6 to 1.5. Such values are experienced at a reference distance from the bed ranging about $(3-16)$cm, the bed being covered with dunes characterized by peak amplitudes of the order of $(20-80)$cm.

Let us then proceed to describe the procedure employed to obtain our results. The analysis has been carried out considering the simplest temporal distribution of tidal velocity, namely:

$$\bar{\mathrm{U}}_0(t) = \cos(\mathrm{t}) \,. \quad (2.187)$$

Once flow resistance was calculated we obtained the basic flow field from equations (2.65, 2.82). The basic concentration field was then found by means of eq. (2.91) having calculated the dimensional fall velocity W_s^* using (2.186). Once the basic state was completely determined, we could then proceed to calculate the perturbation of the flow field and finally the bottom topography. All the differential systems were solved numerically using a Runge-Kutta scheme

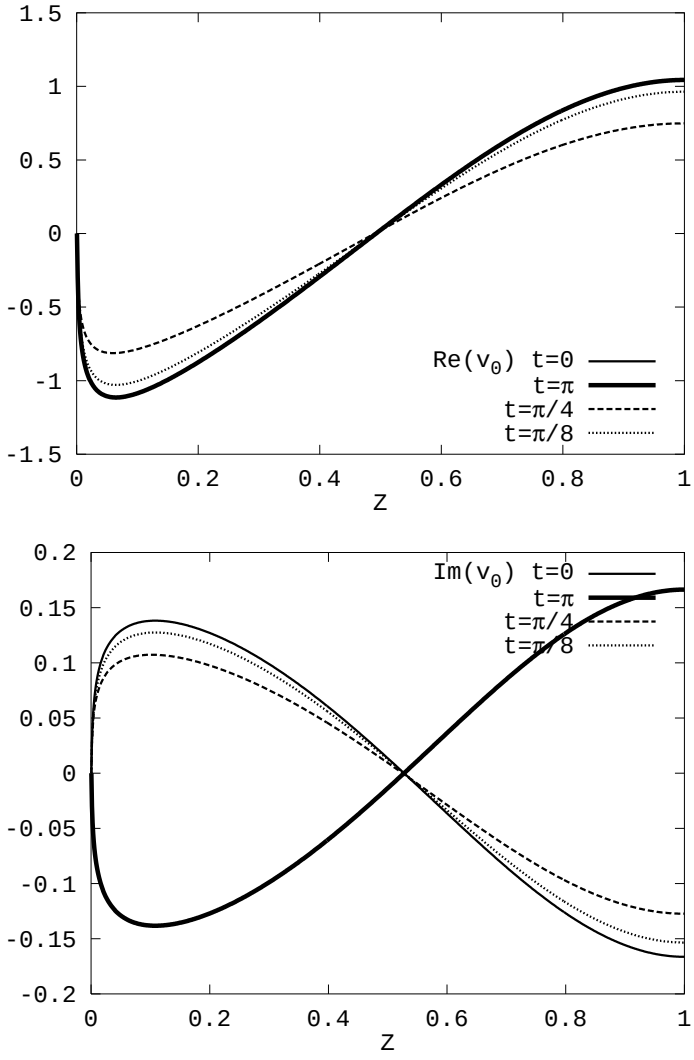

Figure 2.6: *The real part (above) and the imaginary part (below) of the vertical distribution of the lateral component of velocity perturbation with vanishing depth average v_0 is plotted at various instants. (Values of the relevant parameters are as follows $\beta = 6, \lambda = 0.05, R_p = 4, \overline{\theta}_0 = 0.6, d_s = 2 \cdot 10^{-5}$).*

of fourth order while quadratures were performed using Simpon's rule. Figure 2.6 shows examples of the real part and imaginary part of the vertical distributions of the centrifugally induced lateral component of the perturbation velocity v_0 for given values of the relevant parameters β, C_{f0}, R_p, d_s at

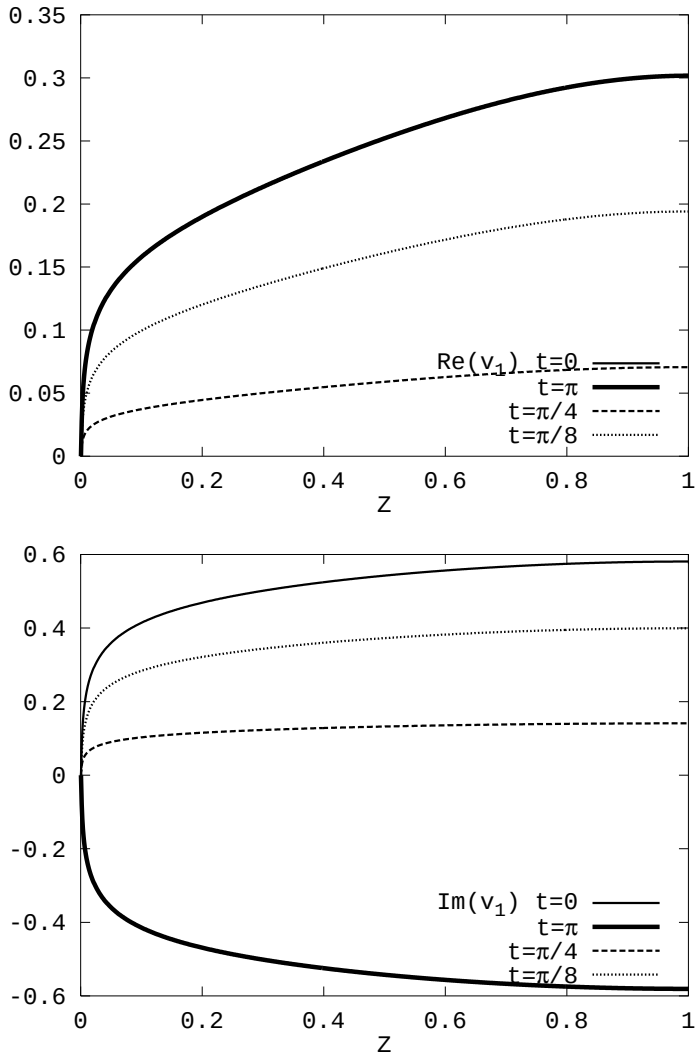

Figure 2.7: *The real part (above) and the imaginary part (below) of the vertical distribution of the topographically driven lateral component of velocity perturbation* $v_m(m = 1)$ *is plotted at various instants. (The values of the relevant parameters are the same as in fig. 2.6).*

various instants during the tidal cycle, namely at the flood $(t = 0)$ and ebb $(t = \pi)$ peaks, as well as at $t = \pi/8, t = \pi/4$. The vertical distribution of the topographic component of the perturbation of the lateral velocity v_m for $(m = 1)$ is plotted in figure 2.7. As one may expect from the symmetry of the

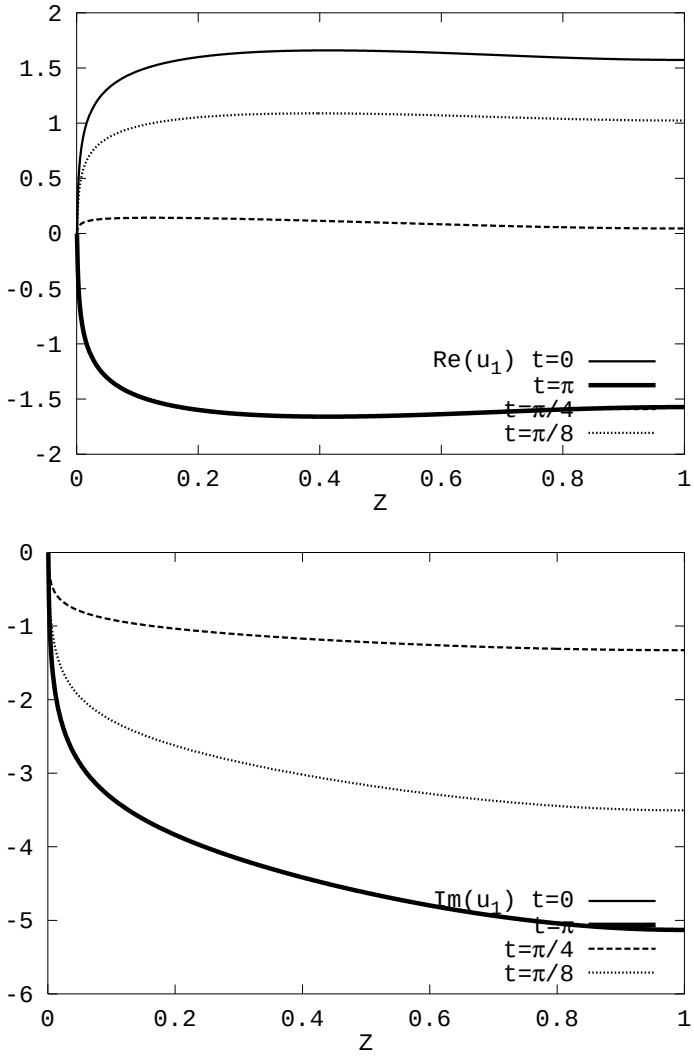

Figure 2.8: *The real part (above) and the imaginary part (below) of the vertical distribution of the longitudinal flow perturbation $u_m(m = 1)$ is plotted at various instants. (The values of the relevant parameters are the same as in fig. 2.6).*

problem it appears that the reversal of the basic tidal flow does not affect the secondary flow. Therefore the solutions for v_0 and $v_m(m = 1, 2, 3, ..)$ satisfy

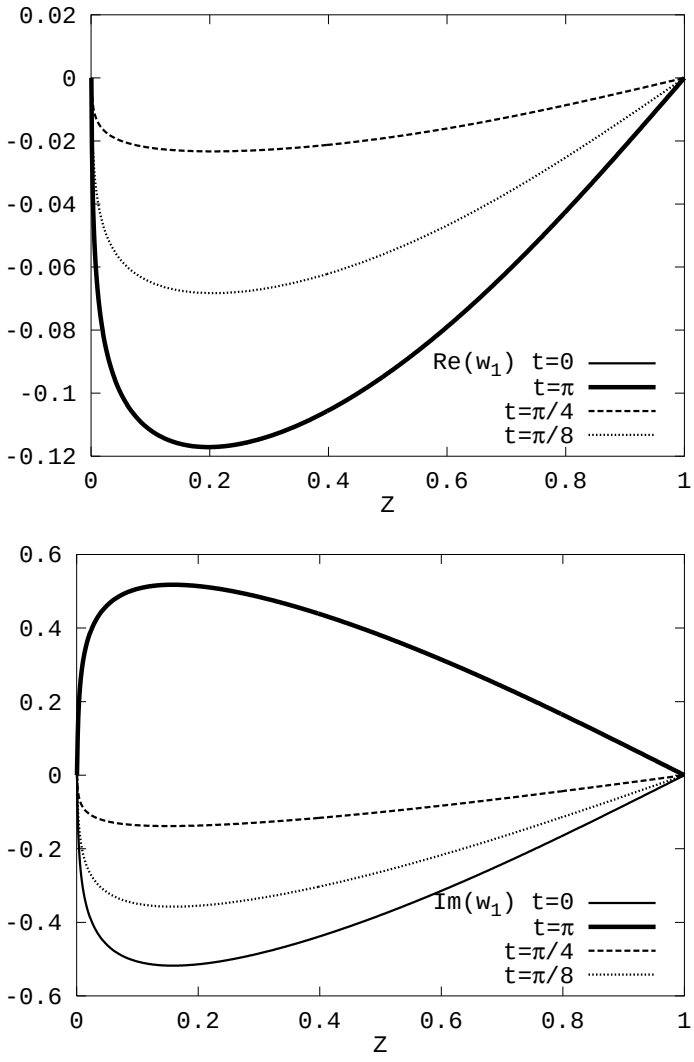

Figure 2.9: *The real part (above) and the imaginary part (below) of the vertical distribution of the vertical flow perturbation* $w_m(m = 1)$ *is plotted at various instants. (The values of the relevant parameters are the same as in fig. 2.6).*

the condition

$$v_m(Z,t) = \tilde{v}_m(Z,t+\pi) \qquad (m = 0,1,2,3,....)\,, \tag{2.188}$$

where a tilde denotes the complex conjugate of a complex number. Note that

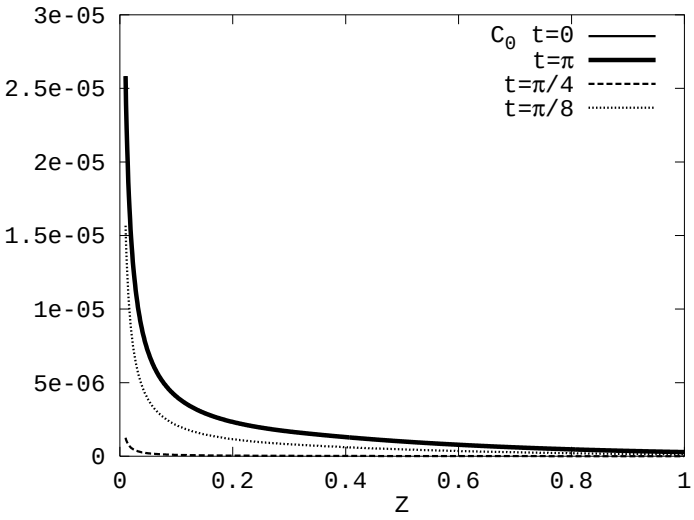

Figure 2.10: *The vertical distribution of the basic concentration field $\mathcal{C}_0$ is plotted at various instants. (The values of the relevant parameters are the same as in fig. 2.6).*

for the values of relevant parameters of figures 2.6, 2.7, 2.8 and 2.9 the lateral component of secondary flow attains peak values equal to $(2.7\nu V_0^*)$. Figure 2.8 shows the vertical distribution of the perturbation of the longitudinal velocity u_m for $(m = 1)$. Note that, due to the symmetry of channel geometry, the reversal of the basic flow leads to an antisymmetric pattern of the perturbation of the longitudinal velocity, hence:

$$u_m(Z,t) = -\tilde{u}_m(Z,t+\pi) \qquad (m = 1,2,3,....)\ . \tag{2.189}$$

Results for the vertical component of flow perturbation $w_m(m = 1)$ (fig. 2.9) and for the perturbation of the sediment concentration $\mathcal{C}_1$ (fig. 2.11) display characteristics similar to those found for the lateral component of velocity perturbation. Note that, for the values of the relevant parameters of figure 2.11, $\mathcal{C}_1$ takes values of the same order as $\mathcal{C}_0$ which is plotted in figure 2.10.

Having determined the perturbation of the flow field, we then proceeded to evaluate the functions $\overline{d}(t)$ and $d_m(t)$ in order to obtain the pattern of bottom topography. Figure 2.12 shows the patterns of deposition and scour for given values of the relevant parameters at the positive $(t = 0)$ and negative $(t = \pi)$ peaks of the tidal cycle (the arrow indicates the direction of the basic flow). Again note the symmetrical position of the point bar-pool with

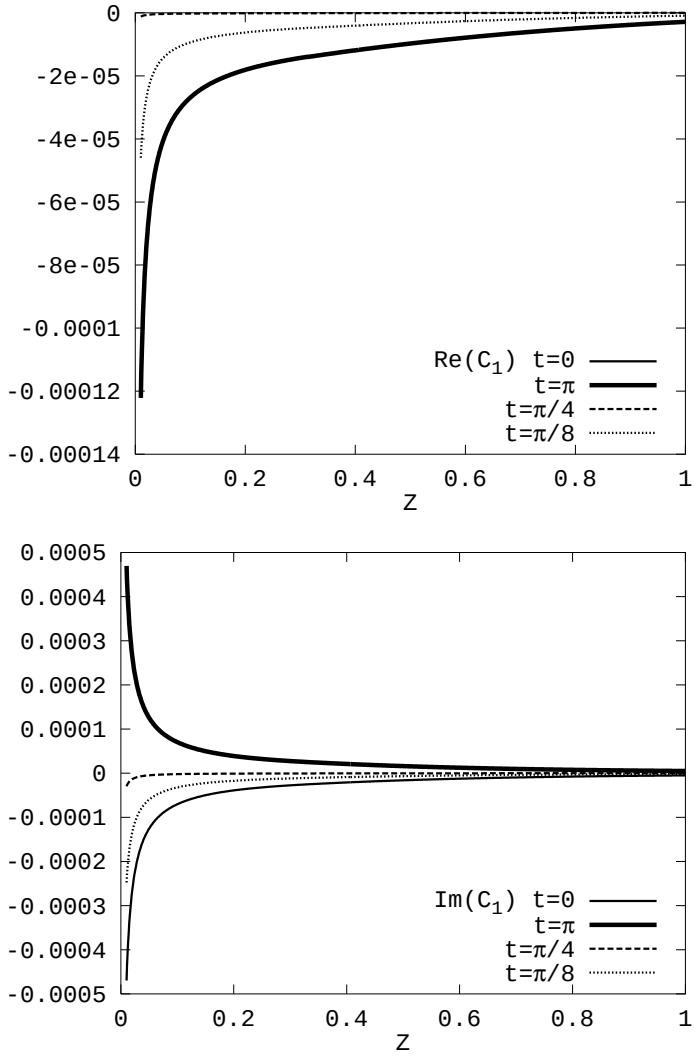

Figure 2.11: *The real part (above) and the imaginary part (below) of the vertical distribution of perturbation of concentration field $\mathcal{C}_m(m = 1)$ is plotted at various instants. (The values of the relevant parameters are the same as in fig. 2.6).*

respect to the bend apex, a result which provides a check of consistency for the present analysis. The patterns of the dimensionless velocity at the free surface (a) and of the dimensionless bed shear stress vector (b) are plotted in Figures 2.13, 2.14, 2.15 at $t = 0, \pi/8, \pi/4$ respectively. As one may expect

the thread of high-velocity shifts from the inner to the outer bend due to the effect of secondary flow, while the channel deepens towards the outer part of the bend. At the same time the channel experiences higher bed shear stress at the outer bank close and downstream to the bend apex, thus indicating the tendency of the meander to amplify and migrate downstream. Note that, at each cross section the transverse slope of the bottom is maintained through a balance, acting on bedload particles, between the inward transverse component of the bed shear stress and the the outward downhill component of gravity. Such effects tend to weaken as the basic flow reversal is approached. Due to the periodicity of the basic flow, the point bar-pool pattern migrates alternatively forward and backward in a symmetric fashion: in other words no net bar migration in a tidal cycle is present. During the cycle the instantaneous Shields parameter varies from zero to some maximum value at the tidal peak. As the Shields parameter θ increases, sediments are transported at first as bed load; for larger values of θ suspension becomes an appreciable fraction of the total transport. At the same time the bottom surface experiences the formation of dunes ascertained by using Van Rijn's (1984) criterion, according to which dunes are present whenever the stage parameter $\frac{\theta'-\theta_c}{\theta_c}$ is lower than 25. The oscillatory character of both position and amplitude of point bar emerges from Fig. 2.16 (left) which describes position and intensity of the maximum dimensionless flow depth during a quarter of tidal cycle: in fact $\Psi_{D_{max}}$ denotes the phase of the location where the maximum dimensionless flow depth D_{max} is experienced at the outer bank, measured relative to the bend apex. Note that the location of the maximum scour oscillates in time with maximum displacement (in half a cycle) of the order of a fraction of a radiant, hence a small value relative to meander wavelength. It appears that, as the intensity of the basic flow decreases, the point bar migrates upstream decreasing its amplitude. Approaching basic flow reversal, the Shields parameter reaches some threshold value below which part of the channel cross section becomes inactive: in other words close to the inner bend the flow velocity can be so small that the Shields number falls below the threshold value for sediment motion. The analysis of Seminara & Solari (1998) suggests that the present approach fails when the mean Shields parameter ranges about $2-3$ times θ_c, which corresponds to the minimum Shields parameter for the occurrence of transport throughout the whole of the cross section. Note that overtides would not produce any net migration of point bars. This is clearly shown in fig. 2.16 (right) where we have plotted the location of the maximum dimen-

sionless flow depth referring to a basic state characterized by the presence of a second harmonic, namely $\bar{U}_0(t) = \cos(\mathrm{t}) + \frac{1}{5}\cos(2\mathrm{t})$. The figure clearly shows that such location oscillates back and forth in a perfectly symmetric fashion. The role of suspension can be inferred from Fig. 2.17, which shows the amplitude of the maximum flow depth at $t = 0$ as a function of particle Reynolds number R_p, which controls the ratio of suspended to bed load (see the line labelled as '$\frac{q_{s0}}{Q_0 \phi_{b0}}$'). As it has been shown by Seminara & Tubino (1986) in the fluvial case, suspension leads both to downstream shifting and to increasing amplitude of the point bar with respect to the case of vanishing suspended load, whereas flattening of the point bar occurs for higher values of the above ratio.

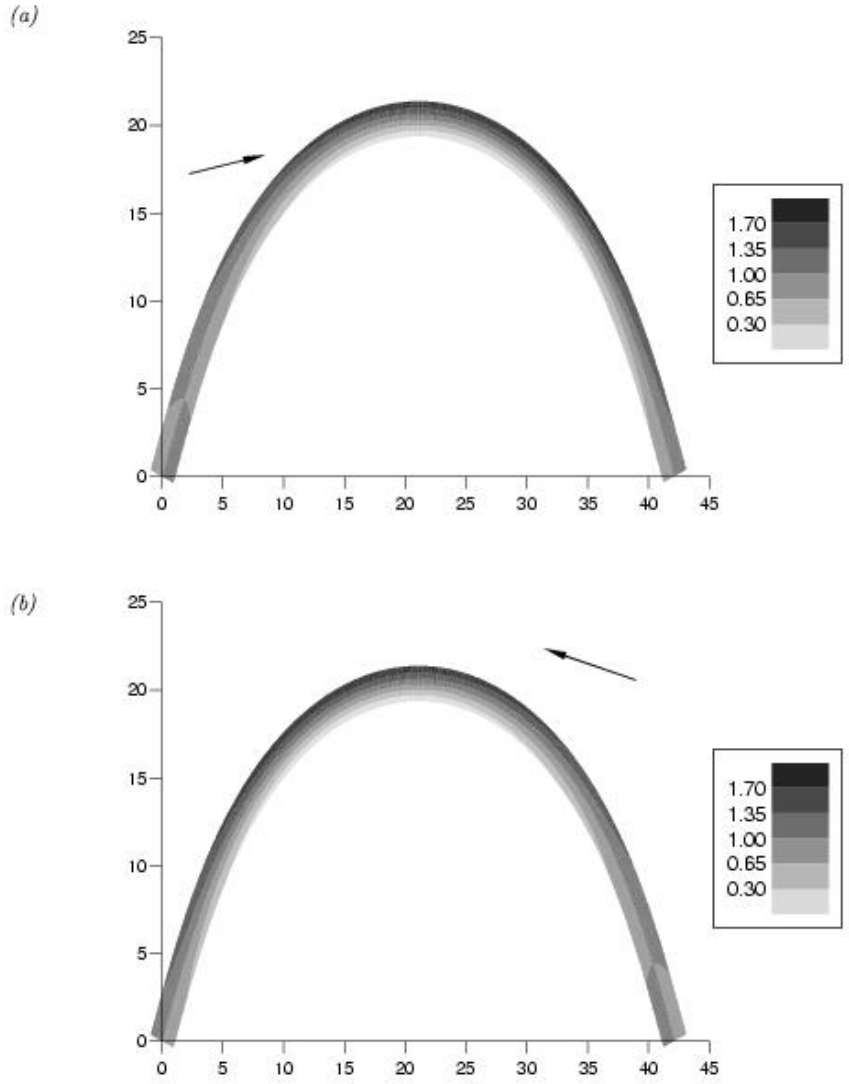

Figure 2.12: *The pattern of the dimensionless flow depth is plotted at the positive* $(t = 0)$ *peak of the tidal cycle (figure (a)) and the the negative* $(t = \pi)$ *peak of the tidal cycle (figure (b)). (The values of the relevant parameters are the same as in fig. 2.6 moreover* $\nu = 0.03$*).*

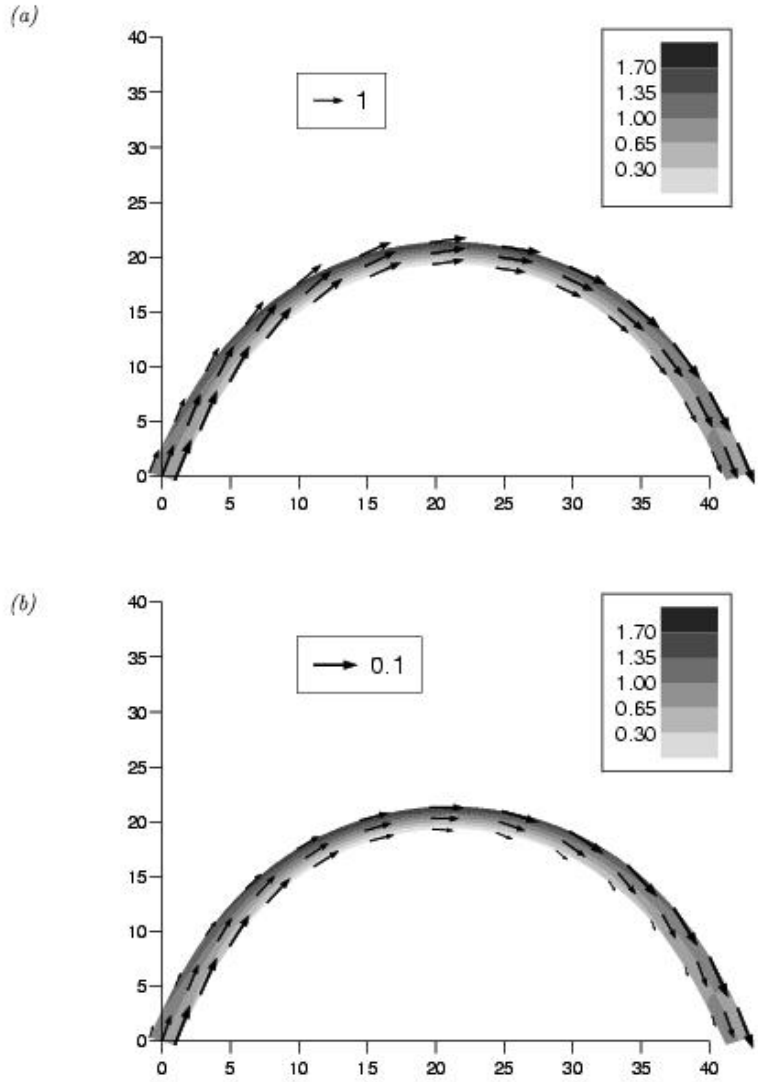

Figure 2.13: *The pattern of the dimensionless velocity at the free surface (figure (a)) and of the dimensionless bed shear stress vector (figure (b)) is plotted at the positive peak of the tidal cycle. (The values of the relevant parameters are the same as in fig. 2.6, moreover* $\nu = 0.03$*).*

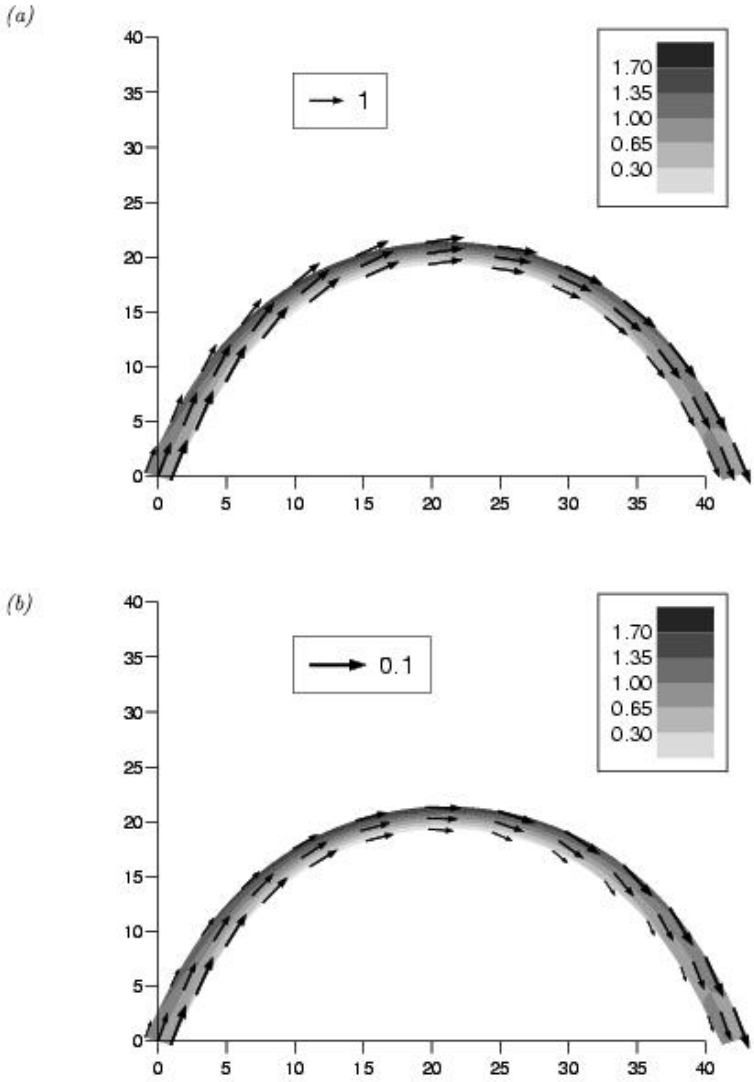

Figure 2.14: *The pattern of the dimensionless velocity at the free surface (figure (a)) and of the dimensionless bed shear stress vector (figure (b)) is plotted at* $t = \pi/8$*. (The values of the relevant parameters are the same as in fig. 2.6, moreover* $\nu = 0.03$*).*

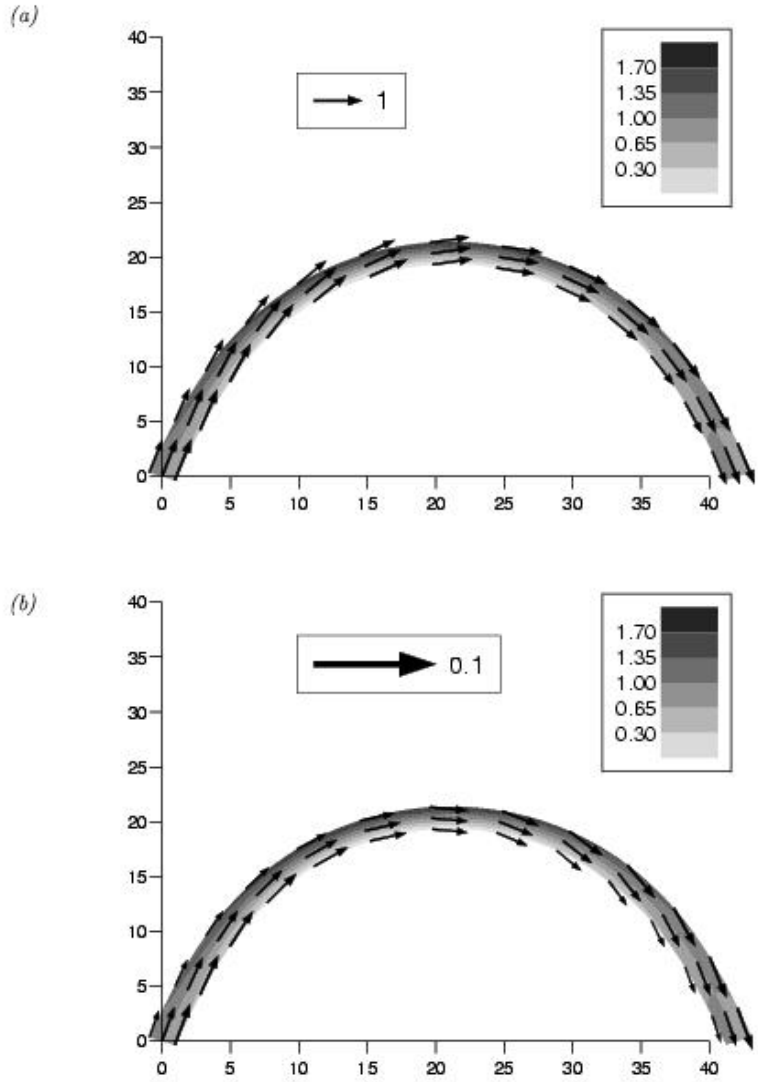

Figure 2.15: *The pattern of the dimensionless velocity at the free surface (figure (a)) and of the dimensionless bed shear stress vector (figure (b)) is plotted at* $t = \pi/4$*. (The values of the relevant parameters are the same as in fig. 2.6, moreover* $\nu = 0.03$*).*

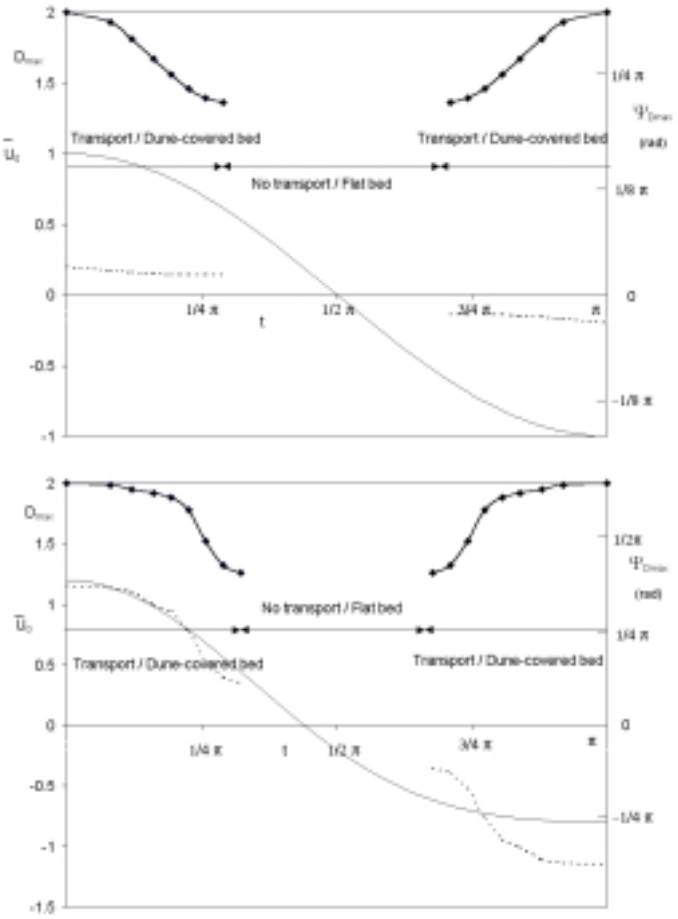

Figure 2.16: *Temporal variations of the position and intensity of the maximum dimensionless flow depth during half a tidal cycle in the case of a tidal velocity characterized by the temporal distributions* $\bar{\mathrm{U}}_0(t) = cos(t)$ *(above) and* $\bar{\mathrm{U}}_0(t) = \cos(\mathrm{t}) + \frac{1}{5}\cos(2\mathrm{t})$ *(below). (The values of the relevant parameters are the same as in fig. 2.6, moreover* $\nu = 0.03$*). The continuous line describes the temporal distribution of the basic flow field* $|\overline{\mathrm{U}}_0|$*, the dashed lines indicate the phase lag between the cross section where the maximum flow depth is located and the cross section at the bend apex (*$\Psi_{D_{max}}$*), the bold continuous lines denote the intensity of the maximum dimensionless flow depth (*D_{max}*).*

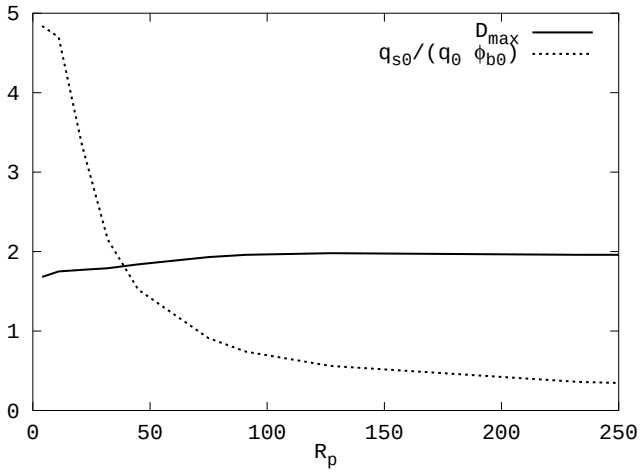

Figure 2.17: *The amplitude of the maximum dimensionless flow depth is plotted as a function of R_p. (Values of the relevant parameters are as follows $\beta = 5, \lambda = 0.25, \overline{\theta}_0 = 1.5, d_s = 10^{-4}, \nu = 0.03$).*

2.7 The formation of tidal meanders: a 'bend' process?

The above solution for the flow and bed topography fields can be set at the basis of a linear 'bend' instability theory of the type originally proposed by Ikeda et al. (1981) and later developed by Blondeaux & Seminara (1985). The

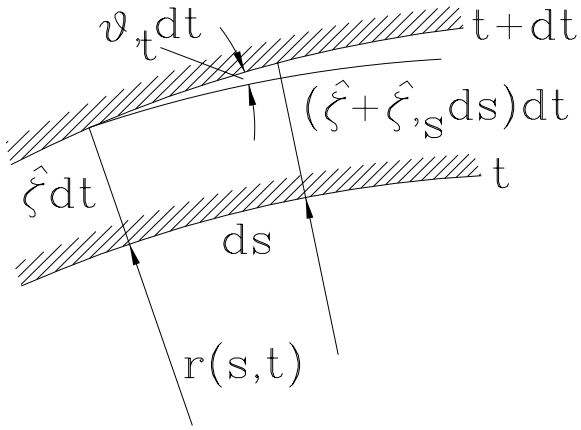

Figure 2.18: *Planimetric evolution: sketch and notations*

bend instability theory is best formulated in terms of a planimetric evolution equation of the meandering channel. A linear intrinsic form of the latter is readily obtained. Let $\hat{\zeta}$ denote the lateral migration rate of the channel, scaled by the quantity V_0^*, i.e. by the flow velocity scale (see eq. 2.4c). Furthermore let s be the curvilinear coordinate which identifies the location at time t of the cross section which was located at s_0 initially, the quantities s and t being dimensionless. The migration rate is a function of s and t through its dependence on the spatial and temporal distributions of the bank erosion rate. Below we will need to formulate some physically based closure assumption in order to couple the evaluation of $\hat{\zeta}$ to the knowledge of the flow field, of bed topography and of the geological texture of the bank. Fig. 2.18 shows that the relative displacement of two neighboring points of channel axis, say s and $s + ds$, in the infinitesimal time interval dt can be expressed in terms of the infinitesimal temporal variation of the angle ϑ which the tangent to the channel axis forms with some Cartesian direction x (say the valley axis). It is

found that:

$$\frac{\partial \hat{\zeta}}{\partial s} ds dt = (\frac{\partial \vartheta}{\partial t}\bigg|_{s_0} dt) ds \ . \tag{2.190}$$

Strictly speaking, the time derivative is a Lagrangian derivative. However, in the context of a linear stability theory, where deviations of the pattern of channel axis from the straight configuration are assumed to keep small, we may safely approximate the Lagrangian derivative with its Eulerian counterpart. Hence, the linear form of the planimetric evolution equation of the channel reads:

$$\frac{\partial \vartheta}{\partial t} = \frac{\partial \hat{\zeta}}{\partial s} \ . \tag{2.191}$$

The non linear version of the equation (2.191) for the fluvial case is derived by Seminara, Zolezzi et al., 2000 and has an integro - differential form. Meanders develop typically as a result of erosion at concave banks and deposition at the convex banks. This is a highly complex process which proceeds in an intermittent fashion: bank collapse may arise from excess scour at the bank toe, the development of tension cracks, the effects of ground water seepage and of vegetation, etc. However it has proved quite satisfactory (Ikeda et al., 1981, Mosselman, 1991, Hasegawa, 1989) to model the long term meander development as a continuous process such that the lateral migration rate of the channel is simply proportional, through some erodibility coefficient e (of the order of 10^{-7}), to some measure of the perturbation of the flow field relative to the straight configuration. We rule out any possible effect of laterally symmetric components of the flow perturbations on the erosion rate, on the ground that such symmetric components would lead to channel widening producing no shift of the channel axis: hence, any appropriate measure of flow perturbation must be expressed in terms of the difference between the value attained at the outer bank and the corresponding value at the inner bank.

We now assume that tidal meandering develops in a similar fashion as for its fluvial counterpart. This assumption is tentatively based on the analogy between the planimetric shapes of fluvial and tidal meanders but it does not rely on detailed field observations and will require substantiation in the near future. However, it is instructive to analyze its implications. Let us then propose a simple generalization of the erosion law suggested by Ikeda et al. (1981), accounting for the three dimensional and unsteady character of our flow field. In fact, in the context of the flow model employed by Ikeda et al. (1981), which was depth averaged and steady, the erosion law was assumed

to be

$$\hat{\zeta} = e\nu \left(\tilde{U}|_{n=+1} - \tilde{U}|_{n=-1} \right) \ , \tag{2.192}$$

with $\tilde{U}$ perturbation of the longitudinal component of the depth averaged velocity. In our case, we generalize (2.192) such to account for the integrated effect of erosion throughout a tidal cycle. Hence we write:

$$\hat{\zeta} = e\nu \left[\int_0^{2\pi} \left(\mathcal{I}_u|_{n=+1} - \mathcal{I}_u|_{n=-1} \right) dt \right] \ , \tag{2.193}$$

where $\hat{\zeta}$ represents the average lateral migration rate in a tidal cycle, being $\mathcal{I}_u = \int_{Z_0}^{1} u d\xi$. Note that, in the context of a linear theory, different choices of the perturbation quantity in (2.193) (say the perturbation of the bottom stress at the bank toe), would not lead to any significant differences in the predictions of the bend stability theory. We can then employ the solution derived in section 2.5 to transform the planimetric evolution equation (2.191) with the closure assumption (2.193) into a linear amplitude equation for meander evolution. Recalling (2.1, 2.2) and noting that higher harmonics are not generated as a result of a linear planimetric development, we may represent the instantaneous channel configuration as follows:

$$\vartheta = \vartheta_0(t) \exp i\lambda s + c.c. \ , \tag{2.194}$$

where the function $\vartheta_0(t)$ plays the role of a meander amplitude. Comparison between the latter formulation and the definition (2.1) suggests that ϑ_0 is an imaginary number, hence it is convenient to set $\vartheta_0 = i\hat{\vartheta}_0$ with $\hat{\vartheta}_0$ a real function such that

$$\hat{\vartheta}_0 = \nu/\lambda \ . \tag{2.195}$$

Recalling the expansion (2.105) and substituting from (2.193, 2.194) into the planimetric evolution equation (2.191) and using (2.195) we end up with the following amplitude equation:

$$\frac{\partial \hat{\vartheta}_0}{\partial t} = G\hat{\vartheta}_0 \ , \tag{2.196}$$

where

$$G = \int_0^{2\pi} G_i dt \ , \ G_i = -2e\lambda^2 \left(\sum_{m=1}^{\infty} (-1)^m \mathcal{I}_{u_m} \right) \ , \tag{2.197}$$

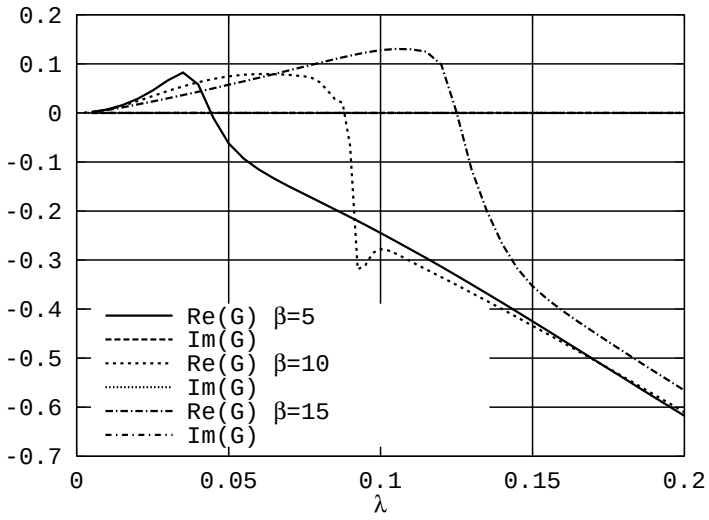

Figure 2.19: *The real part of the complex growth rate of tidal meanders is plotted as a function of meander wavenumber λ and for given values of the width ratio β. (Values of the relevant parameters are as follows: $\overline{\theta}_0 = 1, d_s = 2 \cdot 10^{-5}, R_p = 4$).*

being G_i the instantaneous growth rate. Not surprisingly, the amplitude equation (2.196) allows for a simple exponential solution with complex growth rate G, a result typical of any linear stability theory. Hence, for given values of the width to depth ratio β, of the peak Shields parameter θ and of the particle Reynolds number R_p, meanders grow for values of the meander wavenumber λ such that the real part of the complex growth rate G is positive. Furthermore, the net migration rate of the meander pattern is proportional to the imaginary part of G. The latter quantity is invariably found to vanish, confirming the absence of any net migration of the meander pattern, which could be anticipated on physical ground due to the absence of a preferential direction of the basic state. Fig. 2.19 shows the typical trend exhibited by the growth rate as a function of meander wavenumber for given values of the relevant physical parameters. Such trend is quite similar to that found in the river case (see, for instance, Blondeaux & Seminara (1985)). It shows that initial perturbations with wavelengths smaller than some threshold value decay. Moreover, a peak of growth rate occurs for the most unstable wavenumber λ_m depending on the flow and sediment parameters. Such peak is reminiscent of the analogous

peak discovered by Blondeaux & Seminara (1985) for river meanders. This is not surprising as, in the context of the present formulation, the response of tidal meanders simply arises from an integrated effect of the instantaneous patterns associated with the oscillatory basic state. Hence, the peak in the response is associated with the occurrence, during the tidal cycle, of resonant or quasi resonant conditions in a similar fashion as found in the steady river case. Figure 2.20 shows the behavior of the instantaneous growth rate G_i during a quarter of tidal cycle. Each curve displays a maximum which may attain a large value, indicating that, for given values of the pair λ_m, β, the instantaneous Shields number θ is such that quasi-resonant conditions are typically approached. Resonance arises when curvature forces the flow-bottom topography under conditions such that the system allows for a natural response in the form of non amplifying and non migrating bars with wavelength equal or close to meander wavelength. The occurrence of resonance is displayed in Fig. 2.21 which shows that the topographically induced component of flow depth has an infinite peak at some value of the width ratio. Fig. 2.22 shows the dependence of the most unstable wavenumber λ_m on the width to depth ratio β for various values of the peak value of the Shields parameter $\overline{\theta}_0$ and for given values of R_p and d_s. It appears that the wavenumber selected by the present planimetric instability analysis ranges between 0.02 and 0.15, at least for peak values of the Shields parameter larger than 0.6.

We cannot pursue a thoroughly satisfactory comparison between theory and experimental observations, as detailed measurements of the hydrodynamic and sedimentologic characteristics of tidal meanders are not available. However, observations reported in section 2.2 suggest that the selected dimensionless wavenumbers range about 0.2 - 0.4, a range somewhat larger than that suggested by fig. 2.22, for typical values of the relevant physical parameters. Note that tidal meandering differs from river meandering for several reasons. One major feature is the oscillatory character of the basic state, which prevents meander migration. Moreover, as pointed out by Seminara & Tubino (2000), free bars oscillates in time without displaying any net migration in a tidal cycle. Such behavior may suggest that planimetric instability of an initially straight tidal channel may be forced by finite amplitude perturbations consisting of free stationary bars. Furthermore the altimetric growth rate of free bars is definitely larger than the planimetric growth rate of meanders, the time scale of the former process being of the order of days, the latter (scaling by the erosion coefficient e) of the order of years. Nevertheless fig. 2.22

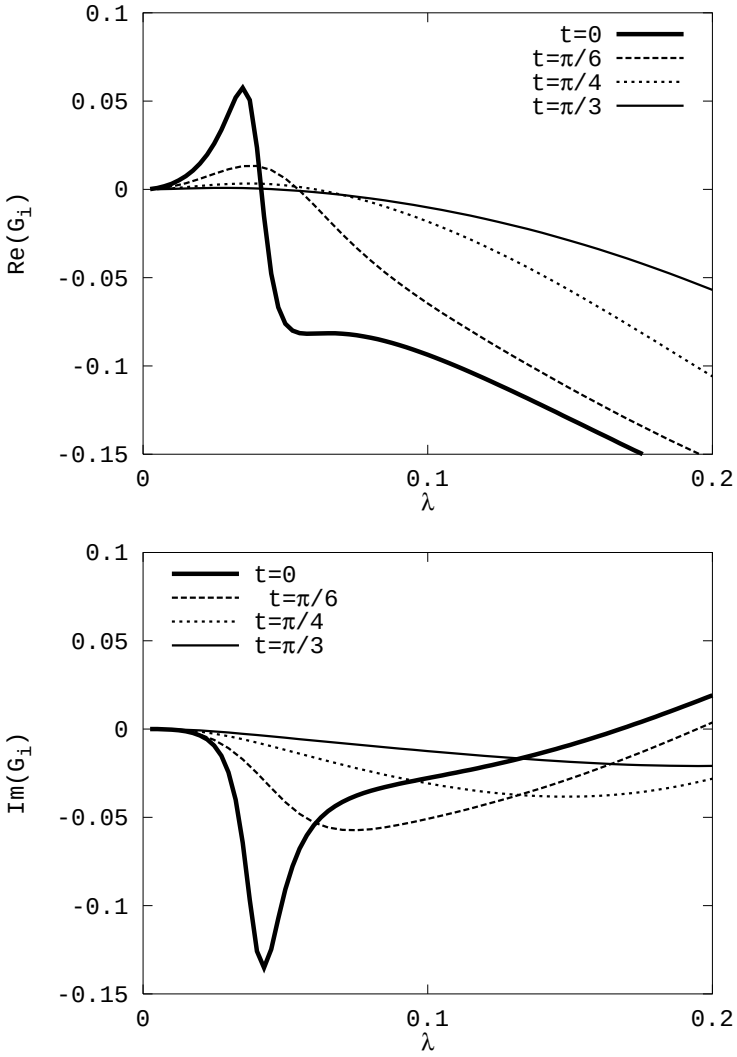

Figure 2.20: *The real part (above) and the imaginary part (below) of the instantaneous complex growth rate of tidal meanders is plotted as a function of meander wavenumber λ for different values of the width ratio β. (Values of the relevant parameters are as follows: $\overline{\theta}_0 = 1, d_s = 2 \cdot 10^{-5}, R_p = 4, \beta = 5$)*

shows that the wavenumber λ_b selected by the free bar mechanism (obtained by Seminara & Tubino, 2000) is much larger than λ_c which represents the threshold value of meander wavenumber above which small amplitude me-

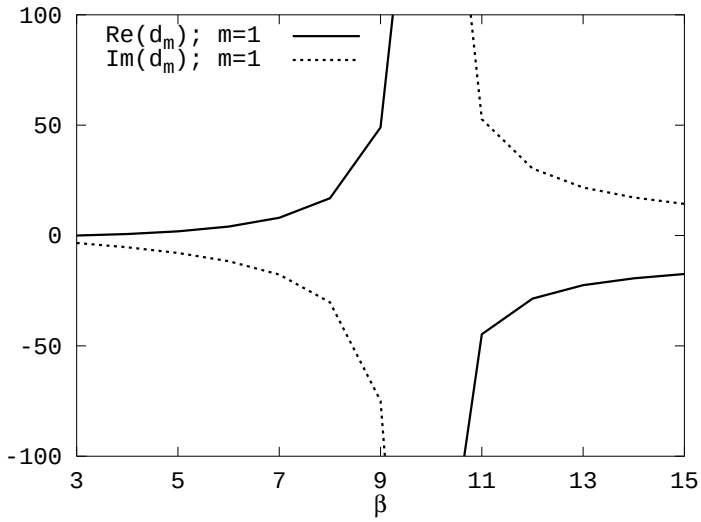

Figure 2.21: *The values of topographically induced component of flow depth* $d_m(m = 1)$ *is plotted versus the width ratio* β *(Values of the relevant parameters are as follows:* $\overline{\theta}_0 = 0.6, \lambda = 0.09, d_s = 2 \cdot 10^{-5}, R_p = 4$*). Note the occurrence of a resonant peak.*

andering perturbations are stable. Hence, though free bar perturbations grow in an initially straight channel much faster than planimetric perturbations, the former are not able to generate growing planimetric perturbations.
On the other hand fields observations have pointed out that tidal meanders are typically more stable than river meanders. In other words their planimetric evolution is much slower than that of their fluvial counterparts. This may be partly due to the more cohesive character of channel banks, typically steeper than their fluvial counterparts (see fig. 2.23). Furthermore, the actual rate of lateral migration of river meanders is known to be controlled by the transport capacity of the stream, i.e. by its ability to remove the sediment accumulated at the bank toe. Such capacity is rather stronger in the fluvial case, where the flow does not reverse, than in the tidal case. Furthermore, in tidal channels, vegetation growing in the adjacent salt marshes plays a stabilizing role which may alter the dynamics of tidal meanders. The observation of tidal networks which have been stable for several decades (like Barnstable (MA, USA), Petaluma (CA, USA) and Pagliaga (Venice, Italy)) suggests that the cohesion may play a crucial role. The formulation of a mechanism of me-

ander formation different from the type discussed in the present contribution should then be attempted in future works.

2.8 Conclusions and future developments

The field evidence reported in section 2.2 suggests that the process of formation of tidal meanders displays a characteristic spatial scale ranging about 10-15 channel widths. It is important to appreciate that such scale is found to be fairly uniform in channels whose width may change by two orders of magnitude. In other words the mechanism of meandering initiation is definitely controlled by morphodynamic effects acting at a scale of a few channel widths. This observation has motivated the present attempt at interpreting the above process on the basis of a planimetric instability theory of the type established for fluvial meandering. The theoretical results discussed in the previous sections show that such a planimetric instability mechanism may indeed operate and selects meander wavenumbers of the correct order of magnitude, though somewhat smaller than those observed in nature.

A few simplifying assumptions adopted in the present work will require some more attention in the near future. Firstly, channel convergence may appreciably affect the structure of point bars induced by channel curvature. Moreover, sediments are often cohesive in the inner portion of tidal channels, a feature which has been ignored in the present analysis. Tidal flats adjacent to the main channel, besides producing a storage effect which controls the adjustment of channel width may also affect the structure of point bars through their influence on the hydrodynamics of channel flow. The present theory is linear, in that perturbations induced by channel curvature are taken to be small enough. As meanders develop, both geometric and flow non linearities may become important, as well as non linear interactions between the free bars (Seminara & Tubino, 2000) and point bars analyzed in the present work. Detailed field observations of flow and bed topography in natural channels and of the role of vegetation in controlling the process of bank erosion are strongly needed to further substantiate the present work. Progress in understanding the morphodynamics of curved tidal channels will also benefit from detailed experimental observations to be performed in the laboratory. Finally, the approach employed in the present work relies on a ‘cohesionless mechanism’ of channel shift similar to that known to be characteristic of fluvial

environments. Field evidence suggest that tidal meanders form in cohesive environment, thus indicating that an alternative mechanism may be acting during the process of meander formation. Further investigation is needed to clarify this issue.

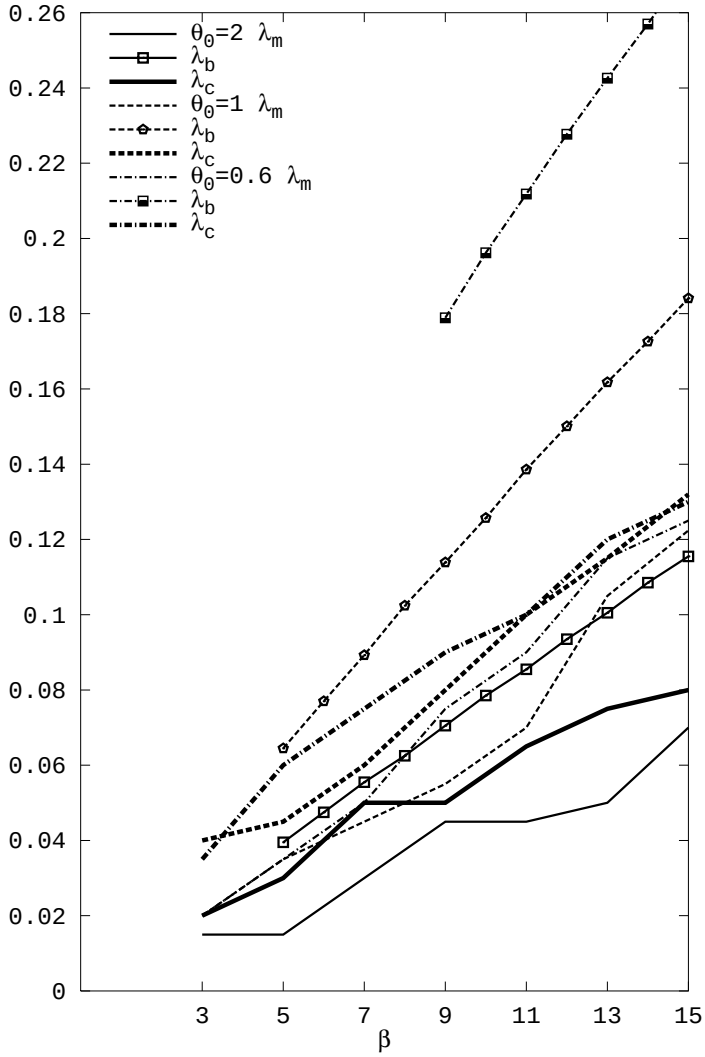

Figure 2.22: *The values of meander wavenumber λ_m selected by bend instability, of meander wavenumber λ_c above which small amplitude meandering perturbations are stable and of the wavenumber λ_b selected by the free bar mechanism (see figure 10 Seminara & Tubino, 2000), are plotted versus the width ratio β for given values of the values of the peak value of the Shields parameter $\overline{\theta}_0$. (Values of the relevant parameters are as follows: $d_s = 2 \cdot 10^{-5}, R_p = 4$; the continuous lines are for $\overline{\theta}_0 = 0.6$, the dashed lines are for $\overline{\theta}_0 = 1$, the dashed-dotted lines are for $\overline{\theta}_0 = 2$).*

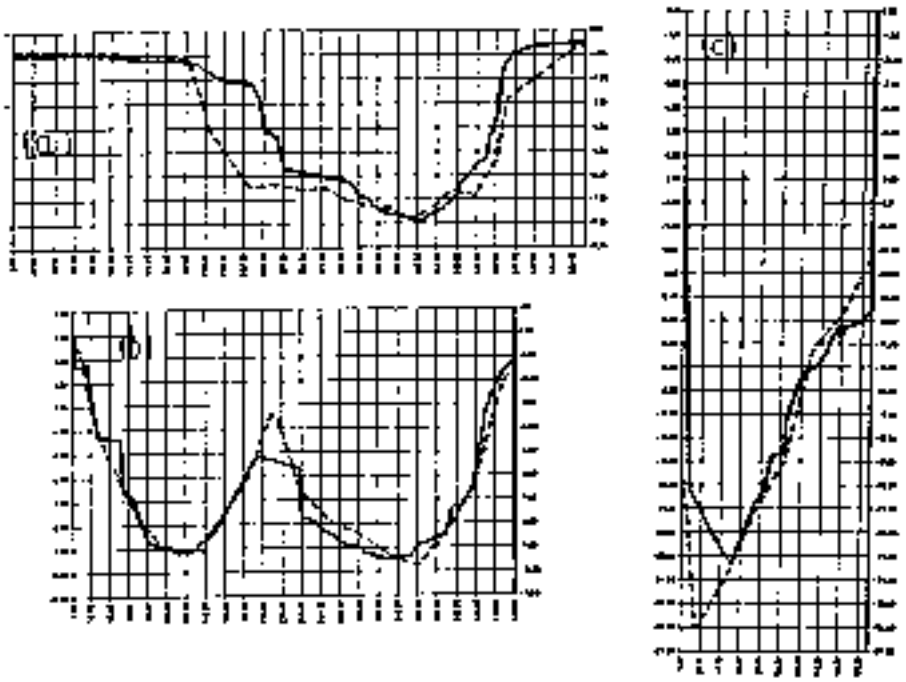

Figure 2.23: *Typical channel cross sections of Venice Lagoon: a) Perognola channel (basin of Chioggia); b) Treporti channel (basin of Lido); c) S. Nicolò (basin of Lido)*

References

Blondeaux P. & Seminara, G., A unified bar-bend theory of river meanders, *J. Fluid. Mech.*, 157, 449-470, 1985

Brownlie, W. R., Prediction of flow depth and sediment discharge in open channels, Rep. KH-R-43A W. M. Keck Laboratory, Cal. Inst. Techn. at Pasadena, 1981.

Danish Hydraulic Institute, Venice Lagoon - Study C.2.3: Morphological Field Investigations, Intensive measurements, Final report, *Consorzio Venezia Nuova*, 1990.

Dean, R. B., Aero Rept. 74-11, Imperial College, London, 1974.

Einstein, H. A., The bedload function for sediment transport in open channel flow, *U.S. Dept. Agric. Tech. Bull.*, 1026, 1950.

Engelund, F. & Hansen, E., A monograph on sediment transport in alluvial streams, *Copenhagen: Danish Technical Press*, 1967.

Engelund, F., Flow and bed topography in channel bends, *J. Hydr. Div. ASCE*, 100(HY11), 1631-1648m 1974.

Engelund, F. & Fredsøe, Sediment ripples and dunes, *Ann. Rev. Fluid Mech.*, 14, 13-37, 1982.

Fagherazzi, S., Bortoluzzi, A., Dietrich, W.E., Adami, A., Lanzoni, S., Marani, M. & Rinaldo, A., Tidal networks 1. Automatic network extraction and preliminary scaling features from digital terrain maps, *Water Resources Res.*, 35(12), 3891-3904, 1999.

Gottlieb, L., Three-dimensional flow pattern and bed topography in meandering channels, *Tech. Univ. Denmark*, I.S.V.A., Series Paper no. 11, 1976.

Hasegawa, K., Study on qualitative and quantitative prediction of meander channel shift, *AGU Water Resources Monograph*, 12, 215-235, 1989.

Ikeda, S., Parker, G. & Sawai, K., Bend theory of river meanders. Part 1. Linear development, *J. Fluid. Mech.*, 112, 363-377, 1981.

Ikeda, S. & Parker, G. (eds.), River Meandering, *Water Resources Monograph*, 12, AGU, Washington D.C, 1889.

Kalkwijk, J. P. TH., & Vriend, H. J. DE, Computation of the flow in shallow river

bends, *J. Hydraul. Res.*, 18, 327-342, 1980.

Kikkawa, H., Ikdea, S. & Kitagawa, A., Flow and bed topography in curved open channels, *J. Hydr. Div. ASCE*, 102(HY9), 1326-1342, 1976.

Kovacs, A. & Parker, G., A new vectorial bedload formulation and its application to the time evolution of straight river channels, *J. Fluid. Mech.*, 267, 153-183, 1994.

Langbein, W. B. & Leopold, L. B., Quasi-equilibrium states in channel morphology, *Amer. J. of Science*, 262, 782-794, 1964.

Lanzoni, S. & Seminara, G., On tide propagation in convergent estuaries, *J. Geophys. Res.*, 103 C13, 793-812, 1998.

Leopold, L. B. & Wolman, M. G., River channel patterns: braided, meandering and straight, *U.S. Geol. Survey Prof.*, 282-B, 1957.

Lumley, J. L., Two-phase and non-Newtonian flows. In *Turbulence*, ed. P. Bradshaw, Topics in Applied Physics, 12, Springer Verlag, 1976.

McTigue, D. F., Mixture theory for suspended sediment transport, *J. Hydr. Div. ASCE*, 107(HY6), 659-673, 1981.

Mosselman, E. & Crosato, A., Theoretical investigation on discharge-induced river-bank erosion, *Comm. on Hydr. and Geotech. Eng.*, 91-1, Delf University of Tecnology, The Netherlands, 1991.

Parker, G., Self formed rivers with stable banks and mobile bed. Part 1. The sand-silt river, *J. Fluid Mech.*, 89, 109-125, 1978.

Rinaldo, A., Fagherazzi, S., Lanzoni, S., Marani, M. & Dietrich, W.E., Tidal networks 2. Watershed delineation and comparative network morphology, *Water Resour. Res.*, 35(12), 3905-3917, 1999.

Rinaldo, A., Fagherazzi, S., Lanzoni, S., Marani, M. & Dietrich, W.E., Tidal networks 3. Landscape-forming discharges and studies in empirical geomorphic relationships, *Water Resour. Res.*, 35(12), 3919-3929, 1999.

Seminara, G. & Solari, L., Finite amplitude bed deformations in totally and partially transporting wide channel bends, *Water Resour. Res.*, 34(6) 1585-1598, 1998.

Seminara, G. & Tubino, M., Further results on the effect of transport in suspension on flow in weakly meandering channels, *Colloquium on 'The Dynamics of Alluvial Rivers'*, Genoa, Italy, 1986.

Seminara, G., Zolezzi, G., Tubino M. & Zardi, D., Downstream and upstream influence in river meandering. Part two: planimetric development, *J. Fluid. Mech.* (on press), 2000.

Solari, L., Seminara, G., Lanzoni, S., Marani, M. & Rinaldo A., Sand bars in tidal channels. Part two: Tidal meanders, *J. Fluid. Mech.* (submitted), 2000.

Talmon, A. M., Mierlo, M. C. L. M. VAN & Struiskma, Laboratory measurements of

the direction of sediment transport on transverse alluvial-bed slopes, *J. Hydr. Res.*, 33, 495-517, 1995.

Rijn, L.C. VAN, Sediment transport, part II: suspended load transport, *J. Hydr. Engng ASCE*, 110(11),1613-1641, 1984.

Chapter 3

Experimental investigation on tidal channels

3.1 Introduction

In the present chapter we illustrate and interpret a set of experimental observations collected in a physical model of tide-dominated well-mixed estuary. Such experiments were aimed at studying the hydrodynamic processes involved in the propagation of the tidal wave and investigating the interactions between a tidal current and a cohesionless bottom. The morphodynamic study will be developed focusing on three major features; namely: i) we wish to observe the formation of bed forms such as dunes and bars, ii) furthermore we wish to ascertain the possible existence of a long term longitudinal equilibrium profile and iii) finally we intend to analyze the interaction between the channel and the adjacent tidal sea. Note that such processes are characterized by distinct time scales, as the time scale typical of bed forms is much shorter than the time scale required for the bottom profile to reach an 'equilibrium' configuration which is of the order of tens of hundreds of years (Lanzoni & Seminara, 2000).
The investigation has been carried out in the laboratory of the Department

Environmental Engineering of Genova University. The study has been developed in the simplest geometry, i.e. a rectilinear flume closed at one end, with fixed side-walls and constant width, as shown in fig. 3.9. The role played by additional features such as channel convergence and the presence of tidal flats will be investigated in future experiments. The procedure followed in the rest of the paper is as follows. After presenting the equations governing the hydrodynamic and morphodynamic problem (section 3.2), we will discuss the scaling rules employed in our physical model of tidal channels (section 3.3). The experimental technique is described in section 3.4, while results concerning the hydrodynamic mechanisms and some preliminary morphodynamic observations are illustrated in section 3.6. Finally, in section 3.7, we report some conclusions and suggestions for future developments.

3.2 Theoretical framework

The experimental investigation has been carried out in an apparatus whose geometry is quite simple: a long, straight flume with a rectangular cross section of constant width, closed at the 'landward' boundary by a vertical wall and connected, at the 'seaward' boundary, to a rectangular basin. It is then appropriate to approach the study of tidal wave propagation employing a one dimensional model in which the hydraulic quantities are cross sectionally averaged.

We perform experiments generating a monochromatic tidal wave. We then impose the following condition at the channel inlet:

$$D^*|_{x^*=0} = D_0^* \left[1 + \epsilon \cos(\omega^* t^*)\right] \ , \tag{3.1}$$

[1] where D_0^* is the average flow depth, ϵ is the ratio tidal wave amplitude/average flow depth, ω^* is the angular frequency and x^* is the channel axis pointing landward starting from the channel inlet. Such temporal distribution models the semidiurnal component (M_2), characterized by a wave period of 12.42 hours, of any tidal wave that would occur in nature. Note that at the channel inlet we were able to impose any free surface oscillation since the generating system was able to produce any low frequency oscillation of the water surface.

The equation (3.1) also represents mathematically the boundary condition at the channel inlet to be applied to the governing equations. At the 'landward'

[1] Hereafter a star will denote a dimensional quantity subsequently made dimensionless.

boundary the impermeable vertical wall requires that both water and sediment fluxes must vanish.

Note that the one-dimensional approach is valid to investigate the propagation of the tidal wave only inside the channel, the flow in the rectangular basin having a two dimensional character due to the presence of a tidal induced jet (see section 3.6.4).

3.2.1 The hydrodynamic problem

We analyze the flow field induced by the propagation of a tidal wave in a straight channel with a rectangular cross section; such problem has been recently revisited by Lanzoni & Seminara (1998). We employ the following notations:

H^* : local free surface elevation;
D^* : local flow depth;
B^* : local width of the cross section;
B_0^* : channel width at the mouth of the channel;
U^* : cross sectionally averaged local flow velocity;
P^* : mean pressure;
t^* : time;
T : tidal wave period;
ω^* : angular frequency of the tide;
x^* : landward oriented longitudinal coordinate;
g : gravity;
U_0^* : characteristic flow speed;
D_0^* : averaged flow depth;
C_0 : characteristic flow conductance;
C : local and instantaneous flow conductance;
a_0^* : the amplitude of the tidal wave at the estuary mouth;
L_0^* : characteristic length scale;
L_e^* : channel length;
L_b^* : channel convergence length.

As it is typical of many estuaries we assume local channel width B^* to vary along x^* according to a classical exponential law, namely:

$$B^* = B_0^* exp\left(-\frac{x^*}{L_b^*}\right), \tag{3.2}$$

where L_b^* will be called convergence length (see fig. 3.1).

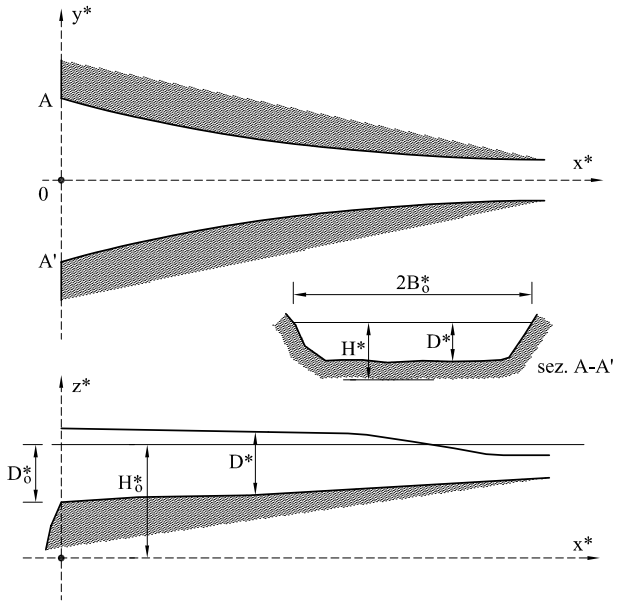

Figure 3.1: *Sketch and notations*

The governing equations describing the unsteady water flow in a wide rectangular channel are the continuity equation and the momentum equations, which read:

$$B^* D^*_{,t^*} + (B^* D^* U^*)_{,x^*} = 0 \tag{3.3}$$

$$U^*_{,t^*} + U^* U^*_{,x^*} + g H^*_{,x^*} + \frac{U^*|U^*|}{C^2 D} = 0 \tag{3.4}$$

where the flow conductance C is a function of bottom roughness. Note that we have neglected the possible presence of tidal flats flanking the main channel. The relevant variables of the problem are made dimensionless as follows:

$$t^* = \omega^{*-1} t \quad (D^*, H^*) = D_0^*(D, H); \quad U^* = U_0^* U; \quad x^* = L_0^* x; \quad C = C_0 c \tag{3.5}$$

Note that the value of L_0^* arises from the dominant balance prevailing in the momentum equation as will be illustrated below.

The resulting dimensionless form of equations (3.3) and (3.4) then read (Lanzoni & Seminara, 1998):

$$\frac{1}{\epsilon} D_{,t} + \mathcal{F} \left(UD \right)_{,x} - \mathcal{K} UD = 0, \tag{3.6}$$

$$\mathcal{S} U_{,t} + \epsilon \mathcal{S} \mathcal{F} U U_{,x} + \frac{1}{\epsilon} H_{,x} + \mathcal{R} \frac{U|U|}{c^2 D} = 0, \tag{3.7}$$

where the following dimensionless parameters arise:

$$\epsilon = \frac{a_0^*}{D_0^*}; \qquad \mathcal{F} = \frac{1}{\epsilon} \frac{U_0^*}{\omega^* L_0^*}; \qquad \mathcal{K} = \frac{1}{\epsilon} \frac{U_0^*}{\omega^* L_b^*}; \tag{3.8}$$

$$\mathcal{S} = \frac{F_0^2}{\epsilon} \frac{\omega^* L_0^*}{U_0^*}; \qquad \mathcal{R} = \frac{F_0^2}{\epsilon} \frac{L_0^*}{C_0^2 D_0^*}. \tag{3.9}$$

Here $F_0 = U_0^* / (g D_0^*)^{1/2}$ denotes the flow Froude number, C_0 is a typical value of the average flow conductance and a_0^* is the amplitude of the tidal wave at the estuary mouth. Note that the factor c in the last term of (3.7) allows one to account for spatial and temporal variations of flow conductance caused by changes in bedform characteristics during the tidal cycle. The parameters $\mathcal{S}$ and $\mathcal{R}$ in the momentum equation denote, respectively, a measure of the effect of local inertia and friction relative to that of gravity. The parameter $\mathcal{K}$ in the continuity equation measures the degree of channel convergence. As discussed by Lanzoni & Seminara (1998) estuaries can be classified as weakly or strongly dissipative if $\mathcal{R}/\mathcal{S} \ll 1$ or $\mathcal{R}/\mathcal{S} \gg 1$ respectively; weakly or strongly convergent if $\mathcal{K} \ll 1$ or $\mathcal{K} \gg 1$ respectively. Such classification allows one to clarify one of the most important mechanism related to hydrodynamic process; in particular whether the channel is flood or ebb dominated. Tide propagating along the channel become asymmetric giving rise to a residual current superimposed on an otherwise symmetrical current profile. Such residual currents are directed seaward/landward in the case of ebb/flood dominated channel. The analysis developed by Lanzoni & Seminara (1998) suggests that weakly dissipative 'infinitely' long channels, either weakly or strongly convergent, are ebb dominated as the peak ebb velocity exceeds the corresponding flood value. On the contrary, strongly dissipative estuaries are invariably flood dominated. Note that due to the formation of a residual current, the channel displays a net sediment flux which is crucial to determine

the altimetric evolution of the bed, as will be discussed in section 3.2.3. Such net flux is directed landward (seaward) in the case of flood (ebb) dominated estuaries.

At the channel inlet we impose a monochromatic tidal wave (see eq. 3.1), we hence write:

$$D|_{x=0} = 1 + \epsilon \cos(t) \tag{3.10}$$

At the landward boundary we impose:

$$U|_{x^*=L_e^*} = 0 \tag{3.11}$$

In the set of experiments we will present below the relevant physical quantities take the following values: $U_0^* = 0.10m/s, T = 130s, C_0 = 20, D_0^* = 0.10m$. The ratio $\mathcal{R}/\mathcal{S}$ (see eq. 3.9) is therefore 0.21. The present tidal channel can be then classified as weakly convergent (being $\mathcal{K} = 0$) and weakly dissipative (being $\mathcal{R}/\mathcal{S} \ll 1$).

The numerical solution of the full de St. Venant equations has been performed by Lanzoni & Seminara (1998) employing the classical box scheme developed by Preissman (1961). Such implicit scheme is based on a four-point rectangular box where time and spatial derivatives are discretized as weighted averages of differences calculated at adjacent points with temporal and spatial weights which have been chosen to attain the values 0.6 and 0.5 respectively.

For values of the parameters typical of our experimental conditions we have employed the algorithm elaborated by Lanzoni & Seminara (1998) to study the propagation of the tidal wave inside the channel. Results, reported in figures 3.2 and 3.3, illustrate the maximum and minimum value of the tidal velocity and of the flow depth along the channel, respectively. It appears that the channel displays a higher flood velocity throughout most of its length; moreover the amplitude of tidal wave increases inward.

3.2.2 Hydrodynamics of a weakly dissipative and weakly convergent channel: linear theory

The equations governing the hydrodynamics of weakly convergent ($\mathcal{K} \ll 1$) and weakly dissipative ($\frac{\mathcal{R}}{\mathcal{S}} \ll 1$) channels on flat bottom assume the following form:

$$D_{,t} + \epsilon \mathcal{F}(UD)_{,x} = 0 \ , \tag{3.12}$$

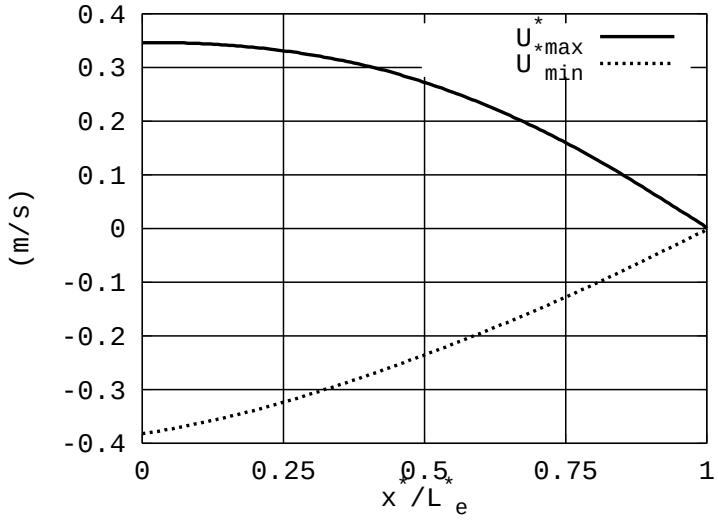

Figure 3.2: *Maximum and minimum values of tidal velocity along the channel. Parameter values are:* $T = 130s, C_0 = 20, D_0^* = 0.098m, \epsilon = 0.132$

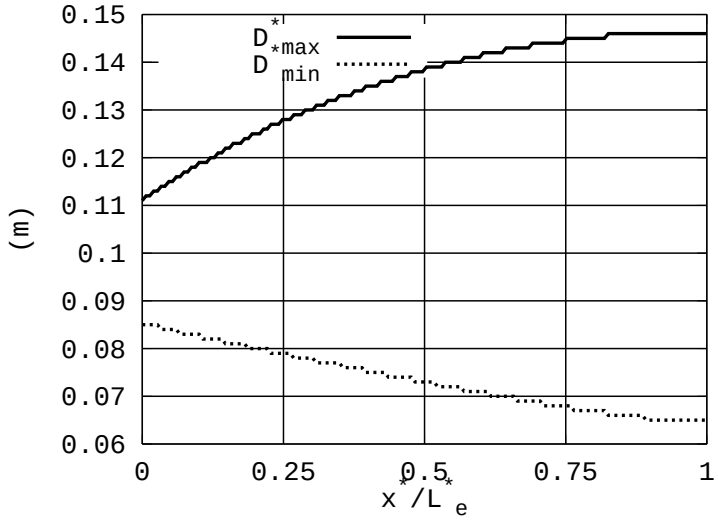

Figure 3.3: *Maximum and minimum values of flow depth along the channel. Parameter values are:* $T = 130s, C_0 = 20, D_0^* = 0.098m, \epsilon = 0.132$

$$U_{,t} + \frac{1}{\mathcal{S}\epsilon} D_{,x} + \epsilon \mathcal{F} U U_{,x} = 0 \ . \tag{3.13}$$

Expanding the flow depth D in the form

$$D = 1 + \epsilon d(x,t) \ , \tag{3.14}$$

the governing equations (3.12, 3.13) become

$$d_{,t} + \mathcal{F}(\epsilon U d_{,x} + D U_{,x}) = 0 \ , \tag{3.15}$$

$$S U_{,t} + \epsilon \mathcal{F} U U_{,x} + d_{,x} = 0 \ . \tag{3.16}$$

The balances imposed by flow continuity and momentum equations (which requires that local inertia must dominantly balance gravity) lead to the following constraints:

$$\mathcal{S} = 1 \ , \qquad \mathcal{F} = 1 \ , \tag{3.17}$$

which are equivalent to the following choices for the scales L_0^* and U_0^*:

$$L_0^* = \frac{\sqrt{g D_0^*}}{\omega^*}, \qquad U_0^* = \epsilon \sqrt{g D_0^*} \ ; \tag{3.18}$$

note that the quantity $\sqrt{(g D_0^*)}$ represents the speed of the tidal wave. Also note that from (3.17) it follows that $F_0^2 \sim O(\epsilon^2)$, hence convective inertia is also negligible in the momentum equation. The system (3.12, 3.13) at the leading order of approximation becomes:

$$d_{,t} + U_{,x} = 0 \ , \tag{3.19}$$

$$d_{,x} + U_{,t} = 0 \ , \tag{3.20}$$

which can be rewritten in the following form

$$d_{,tt} - d_{,xx} = 0 \ . \tag{3.21}$$

Equation (3.21) is the well-known wave equation. The solution, in the case of a channel closed at the inner boundary, reads:

$$d = \frac{1}{cos(L_e)} \cos(t) \cos(\bar{x}) \ , \tag{3.22}$$

$$U = \frac{1}{cos(L_e)} \sin(t) \sin(\bar{x}) \ . \tag{3.23}$$

where $\bar{x} = L_e - x$.
Such solution represents a stationary wave which displays the maximum amplitude at the wall ($\bar{x} = 0$) and a vanishing amplitude at a distance $\bar{x} = n \cdot l/4$ (with n an odd number) from the wall, l being the dimensionless tidal wavelength. Note that the phase lag between flow velocity and free water surface is $\pi/2$. The ratio between maximum tidal amplitude at the landward boundary and at the tidal inlet is

$$\frac{d_{max|\bar{x}=0}}{d_{max|\bar{x}=L_e}} = \frac{1}{\cos(L_e)} \tag{3.24}$$

such ratio is infinite when $L_e = n \cdot \pi/2$ in other words when $L_e/l = n \cdot 1/4$. When this condition is met the system becomes resonant, in reality tidal wave peaking is smoothed by a number of factors: diffusive terms, non linearities, non uniform geometry.

In the present experiments, the wave celerity is about 1 m/s (as $D_0^* = 0.10m$), the tidal wave length is about 130 m (being T=130 s), $l^*/4$ is therefore 33 m; the channel is then not too far from being resonant (as $L_e^* = 24m$). For the same value of the parameters employed in the experiments we will present below, we have plotted the maximum and minimum value of the flow velocity and of the flow depth, such results are reported in figures 3.4 and 3.5 respectively.

3.2.3 The one dimensional morphodynamic problem

Based on the one dimensional formulation of the hydrodynamic problem, one can then study the long-term equilibrium configuration of the bed profile employing a cross sectionally averaged model. The latter problem has been recently tackled by Lanzoni & Seminara (2000). In this section we will outline their work, which will prove useful to understand the physical mechanisms occurring during our experiments.

The dimensionless form of the Exner equation reads

$$\eta_{,\tau} + \left(q_{s,x} - \frac{\mathcal{K}}{\mathcal{F}} q_s \right) = 0 \tag{3.25}$$

where

$$t^* = \tau_0^* \tau; \qquad \eta^* = D_0^* \eta; \qquad q_s^* = \sqrt{\Delta g d_s^{*3}}\, q_s;$$

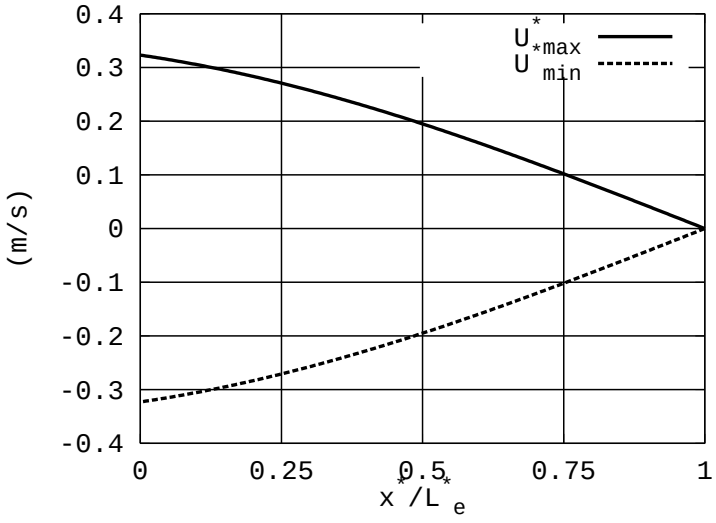

Figure 3.4: *Maximum and minimum value of the flow velocity (according to the linear theory) along the channel. Parameter values are:* $T = 130s, D_0^* = 0.098m, \epsilon = 0.132$

$$\tau_0^* = \frac{(1-p)D_0^* L_0^*}{\sqrt{\Delta g d_s^{*3}}}; \qquad \Delta = \frac{\rho_s - \rho}{\rho} \tag{3.26}$$

where p is sediment porosity, q_s^* is the sediment flux per unit width, d_s^* is the average sediment grain size, ρ_s and ρ are water and sediment densities respectively, η^* represents the bottom elevation which is related to the flow depth by means of the relationship $\eta^* = H^* - D^*$.
The sediment continuity equation states that the spatial variations of the sediment flux are balanced by a rate of aggradation or degradation of the bed surface. The total amount of sediment transport at a certain time in a given cross section is the sum of two contributions: bedload and suspended load which can be evaluated using some semi-empirical formula, such as Meyer-Peter & Muller (1948) relationship for bed load and Van Rijn (1984) approach for the suspended load. In this respect we note that the model of Lanzoni & Seminara (2000) is based on the assumption that sediment transport is in equilibrium with the local and instantaneous conditions. The Exner equation also requires boundary conditions. In the present case the sediment flux at the end of the channel must vanish: such condition is automatically satisfied by the hydrodynamic solution where it was imposed that the instantaneous cross sec-

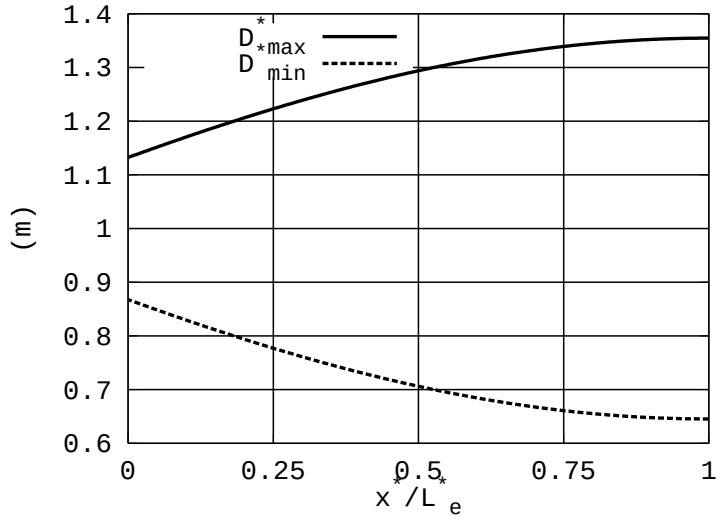

Figure 3.5: *Maximum and minimum value of the flow depth (according to the linear theory) along the channel. Parameter values are:* $T = 130s, D_0^* = 0.098m, \epsilon = 0.132$

tionally averaged speed must also vanish at the 'landward' boundary (recall equation (3.11)).

As pointed out by Lanzoni & Seminara (2000) in the absence of a net sediment discharge either from the sea or from the river, the channel can only reach an average altimetric equilibrium of the bottom (the average being referred to the tidal cycle), provided the average sediment flux vanishes at any cross section along the channel. The distortion of the tidal wave along the channel produces over each tidal cycle a net sediment flux which modifies the bed profile. The hydrodynamics associated with the new bottom configuration leads to a new pattern of bottom stresses and therefore to a new pattern of sediment transport. The equilibrium profile is found to be characterized by a concavity which increases as the estuary convergence increases. The final length of the estuary is determined by the formation of a 'beach' towards the inner portion of the estuary. Notice that, strictly speaking, an instantaneous equilibrium is never reached as the instantaneous sediment flux is in general a non vanishing quantity. Morphodynamics and hydrodynamics are then strictly coupled in a long term evolution process. The result of such a process for parameter values typical of our experimental conditions, is dis-

played in figure 3.6, which illustrate the temporal evolution of the bottom (above) and of the net sediment flux (below) from an initially plane bed configuration along the channel at various instants, respectively. Note that q^*_{s0} in fig. 3.6(below) denotes the quantity $\sqrt{\Delta g d^{*3}_s}$.

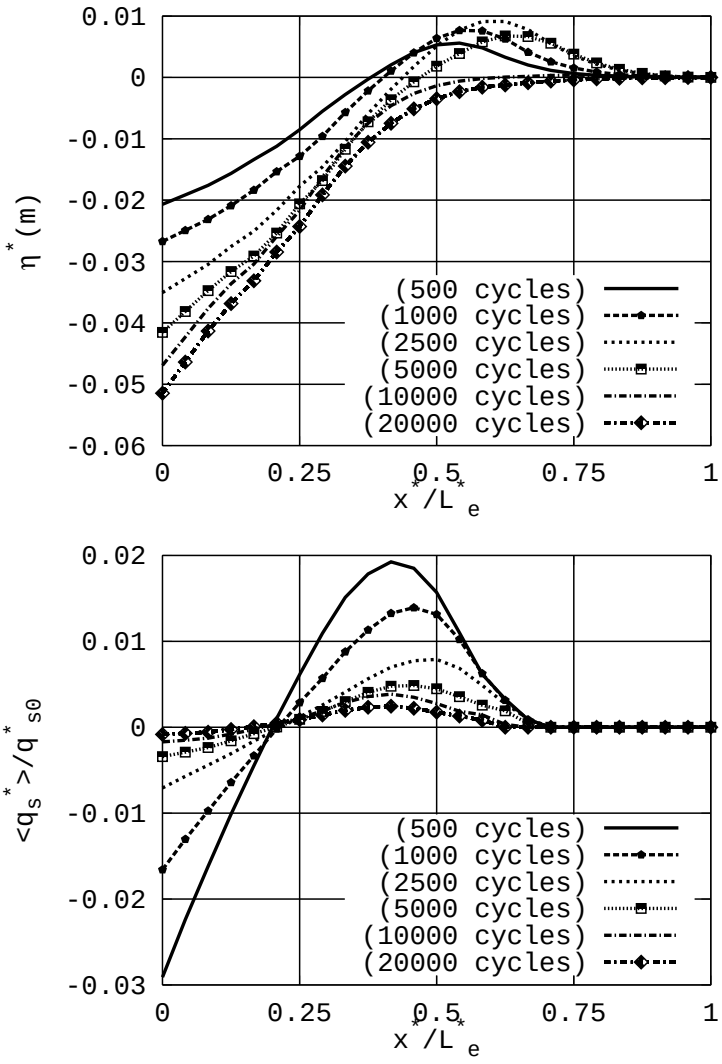

Figure 3.6: *Temporal evolution of the bottom profile (above) and of the net sediment flux (below) from an initially plane configuration. Parameter values are:* $D^*_0 = 0.098m, \epsilon = 0.132, C_0 = 16, d^*_{s50} = 0.31mm, \rho_s = 1480kg/m^3$

3.3 Scaling rules of physical models of tidal morphodynamics

Hydraulic models are essentially based on the establishment of geometric, kinematic and dynamic similarities. Geometric similarity requires the 'shape' of the model to be the same as that of the prototype. It is achieved by making sure that each characteristic length of the prototype is reduced by a constant factor called the scale. Kinematic similarity requires that the 'shape' of the streamlines at any particular time be the same in the model as in the prototype. Dynamic similarity requires that the ratio between forces in the model must be equal to the corresponding ratio in the prototype. In order to achieve dynamic similarity of a phenomenon it is necessary and sufficient to make sure that all relevant dimensionless parameters governing the phenomenon be equal in the model and prototype. In the present section we will discuss the requirements for dynamic and kinematic similarity, the analysis will move from the dimensionless form of the governing equations (see sections 3.2.1 and 3.2.3).

3.3.1 The case of weakly dissipative estuaries

Examples of such estuaries are found frequently in nature: they display large flow depths and fairly low friction coefficient. This limiting behavior is mathematically described by the condition

$$\mathcal{R} \ll \mathcal{S} \, . \tag{3.27}$$

The momentum equation therefore requires that local inertia is balanced by gravitational term (which is an $O(\epsilon^0)$ term, as the spatial fluctuations of the flow depth D are of order ϵ). It follows that we may write:

$$\mathcal{S} = 1 \, , \qquad \Rightarrow \qquad \frac{\omega^* L_0^*}{U_0^*} \frac{F_0^2}{\epsilon} = 1 \, . \tag{3.28}$$

This condition allows us to find the spatial scale L_0^*. By substituting from (3.28) into the definition of the parameter $\mathcal{F}$ (see equation 3.8), it is found that

$$\mathcal{F} = \frac{F_0^2}{\epsilon^2} \, . \tag{3.29}$$

From the conservation of the parameter $\mathcal{F}$ it then follows that the ratio between Froude numbers must be related to the ratio between the amplitude parameters as follows:

$$\frac{F_0}{F_0'} = \frac{\epsilon}{\epsilon'} = e \ , \tag{3.30}$$

having denoted by an apex the quantities in the model. If we indicate by φ the velocity scale and by λ the length scale, the previous relationship reads

$$\varphi = e\sqrt{\lambda} \ . \tag{3.31}$$

In order to simulate the sediment transport process we require that the values of the Shields parameter θ and of the particle Reynolds number R_p be kept constant both in the model and in the prototype. The former constraint reads

$$\frac{\left(\frac{U_0^*}{U_0^{*\prime}}\right)^2}{\frac{\Delta d_s^*}{\Delta' d_s^{*\prime}}} = \frac{\varphi^2}{\sigma\delta} = 1 \ , \tag{3.32}$$

in other words

$$\varphi = \sigma^{1/2}\delta^{1/2} \ , \tag{3.33}$$

having introduced 'distortion' scales for sediment size (δ) and sediment density (σ) as follows:

$$\delta = \frac{d_s^*}{d_s^{*\prime}} \ , \qquad \sigma = \frac{\Delta}{\Delta'} \ . \tag{3.34}$$

We then require that the parameter R_p be kept constant and obtain:

$$\left(\frac{\Delta}{\Delta'}\right)^{1/2} \left(\frac{d_s^*}{d_s^{*\prime}}\right)^{3/2} = \sigma^{1/2}\delta^{3/2} = 1 \ , \tag{3.35}$$

whence:

$$\delta = \sigma^{-1/3} \ . \tag{3.36}$$

Notice that, so far, we have assumed the resistance coefficient to be constant, an assumption which will be discussed later.
Equations (3.31, 3.33, 3.36) may be written as follows:

$$\delta = \sigma^{-1/3} \ , \tag{3.37}$$

$$\varphi = \sigma^{1/3} \ , \tag{3.38}$$

$$e\sqrt{\lambda} = \sigma^{1/3} \ . \tag{3.39}$$

Once we fix the value of σ, which depends on the availability of sediments used in the model, we can calculate the scale for sediment size δ and the velocity scale φ. The parameter e, i.e. the distortion of the dimensionless amplitude of the tide wave, is then obtained once we assume a convenient value for the length scale λ. In the present model we have employed crushed hazelnut shells which have an average diameter of $0.31mm$ and a density of $1480kg/m^3$ (see section 3.4) therefore we find:

$$\sigma = 3.4 \ , \quad \delta = 0.66 \ (\Rightarrow d_s^* = 0.2mm) \ , \quad \varphi = 1.51 \ , \quad e\sqrt{\lambda} = 1.51 \tag{3.40}$$

In the experiments we have carried out D_0^* ranges about 0.1m. If we set $\lambda = 50$ it follows that the dimensionless amplitude of the tidal wave in the model is about 4.6 times that of the prototype. In the first set of experiments ϵ' ranged about $(0.13 - 0.15)$ and the corresponding value of ϵ in the prototype is about $(0.028 - 0.032)$, a fairly low value. It is then appropriate to perform the future experiments with higher values of ϵ'.
We now discuss the role played by the dissipative terms. Evidently both the model and the prototype require $\mathcal{R}/\mathcal{S} \ll 1$. Let us see what are the implications of the following condition

$$\frac{\mathcal{R}/\mathcal{S}}{\mathcal{R}'/\mathcal{S}'} = 1 \ . \tag{3.41}$$

If Θ is the ratio between tidal wave periods, we obtain

$$\frac{\lambda\chi^2}{\varphi\Theta} = 1 \tag{3.42}$$

having denoted by χ the ratio between the flow conductance of the prototype and that of the model. In order to reproduce the dissipative effects we should impose the following scaling:

$$\Theta = \frac{\lambda\chi^2}{\varphi} = \frac{\sigma^{1/3}\chi^2}{e^2} \tag{3.43}$$

In the experiments we have carried out the conductance takes a value ranging about 20 (see section 3.4). Since similar values can be typically observed in many tidal channels (see Lanzoni & Seminara, 1998), we can assume $\chi = 1$.

Figure 3.7: *A wave train superimposed to tidal wave*

The scale Θ therefore ranges about 34 corresponding to a tidal wave period in the model of about 1300 s. The tidal wave period in the laboratory is limited by the size of the experimental apparatus: the longer the tidal wave period, the bigger is the tidal prism which needs to be displaced in order to generate a current in the flume strong enough to bring sediments in suspension. The size of the present generating system (see section 3.4) does not allow to realize tidal wave periods larger than about 180s-200s, hence in our model the time scale Θ is much larger than needed to keep the ratio $\mathcal{R}/\mathcal{S}$ constant. In other words the ratio $\mathcal{R}/\mathcal{S}$ in the model is much smaller than in the prototype. Such distortion does not affect significantly the analysis elaborated here as long as the prototype keeps weakly dissipative. Note that another source of distortion is due to the relative role played by the convective-inertial term which is enhanced in the model, thus leading to a tidal wave which may display sharp fronts, as it has sometimes been observed in the present experiments (fig. 3.7).

Finally, in order to reproduce channel convergence, the parameter $\mathcal{K}$ must remain constant, therefore

$$\left(\frac{\epsilon'}{\epsilon}\right)\frac{\left(U_0^*/U_0^{*'}\right)}{\omega^*/\omega^{*'}\left(L_b^*/L_b^{*'}\right)}=1 \tag{3.44}$$

, in other words

$$\frac{\lambda_b}{\lambda}=\frac{e}{\sigma^{1/3}}\Theta \tag{3.45}$$

, where $\lambda_b = L_b^*/L_b^{*'}$. The convergence of the channel may then be easily reproduced: note that the degree of convergence in the model is much larger

than in the prototype, the right hand side of equation (3.45) being larger than one.

3.3.2 The case of strongly dissipative estuaries

Examples of this kind of estuaries are alos frequent in nature and are characterized by small flow depths. This limiting behavior is mathematically described by the condition

$$\mathcal{R} \gg \mathcal{S} \, . \tag{3.46}$$

In this case the momentum equation imposes a balance between gravity and friction as local inertia is relatively small. Spatial variations of the gravitational term are of order 1. It is then appropriate to write

$$\mathcal{R} = 1 \, , \qquad \Rightarrow \qquad \frac{L_0^*}{C_0^2 D_0^*} \frac{F_0^2}{\epsilon} = 1 \, . \tag{3.47}$$

This condition allows us to find the spatial scale L_0^*. By substituting from (3.47) in the definition of the parameter $\mathcal{F}$ (see equation 3.8) it is found that:

$$\mathcal{F} = \frac{U_0^*}{D_0^* \omega^*} \frac{F_0^2}{\epsilon^2} \frac{1}{C_0^2} \, . \tag{3.48}$$

The conservation of the parameter $\mathcal{F}$ then gives:

$$\Theta = \frac{e^2}{\varphi^3} \lambda^2 \, . \tag{3.49}$$

Such relationship allow us to determine the time scale once the length scale λ and the velocity scale φ are given. The velocity scale is determined by the requirement that sediment transport be reproduced. To reproduce sediment transport we obtain constraints identical to those expressed by equations (3.33, 3.36), therefore:

$$\varphi = \sigma^{1/2} \delta^{1/2} \, , \tag{3.50}$$

$$\delta = \sigma^{-1/3} \, . \tag{3.51}$$

Again notice that we have assumed a constant value of flow conductance. The scaling rules thus obtained may be rewritten as follows

$$\delta = \sigma^{-1/3} \, , \tag{3.52}$$

$$\varphi = \sigma^{1/3} \,, \tag{3.53}$$

$$\Theta = \frac{e^2}{\sigma}\lambda^2 \,. \tag{3.54}$$

For a given value of σ one can find the scale δ for sediment size and the velocity scale φ. The time scale Θ is calculated once the length scale and the scale for the dimensionless tidal amplitude are imposed. If we consider the present model as strongly dissipative we find

$$\sigma = 3.4 \,, \quad \delta = 0.66 \; (\Rightarrow d_s^* = 0.2mm) \,, \quad \varphi = 1.51 \,, \quad \Theta = \frac{e^2}{3.4}\lambda^2 \,. \tag{3.55}$$

In the experiments we have carried out D_0^* ranges about $0.1m$ which may be taken to correspond to a length scale of about 50. If e ranges about $0.5 - 1$ the time scale falls in the range $180 - 735$, hence the period of tidal wave in the model ranges about $(248 - 60)s$ respectively.
It is instructive at this point to investigate the role played by local inertial effects. Evidently both the model and the prototype require $\mathcal{R}/\mathcal{S} \gg 1$. We then examine the consequences of assuming that:

$$\frac{\mathcal{R}/\mathcal{S}}{\mathcal{R}'/\mathcal{S}'} = 1 \,. \tag{3.56}$$

Taking into account equations (3.53, 3.54) we find

$$\frac{\mathcal{R}'}{\mathcal{S}'} = \left(\frac{\mathcal{R}}{\mathcal{S}}\right) \frac{e^2\lambda}{\sigma^{2/3}} \,. \tag{3.57}$$

From such relationship it appears that the strongly dissipative character of the prototype is definitely maintained in the model which is more strongly dissipative than the prototype.
Channel convergence is maintained keeping constant the parameter K, therefore

$$\lambda_b = \frac{e^3\lambda^2}{\sigma^{2/3}} \,, \tag{3.58}$$

in other words

$$\frac{\lambda_b}{\lambda} = \frac{e^3\lambda}{\sigma^{2/3}} \,. \tag{3.59}$$

The convergence of the channel may be then easily reproduced.

3.4 Experimental setup and procedure

The experiments are carried out on a large indoor platform 29.6 m long and 2.3 m wide. The concrete platform has a weak longitudinal upslope of about $7 \cdot 10^{-4}$ and is covered by 2 cm thick wood panels. Along both sides of the platform is an approximately 0.40 m high rail supporting a carriage used for levelling the bed and measuring the bed topography and water surface level. The rail has been carefully set horizontal, using a cathetometer. The side walls of the channel were constructed by attaching 0.30 m high and 5 mm thick strips of forex to the wooden platform base to form vertical flume walls.

The flume is straight, 24.14 m long and 0.30 m wide with a rectangular cross section closed at one end and connected at the other end to a rectangular basin (2.23 m wide and 4.6 m long) which models the sea. The rectangular basin is connected to a feeding tank (1.51 m, 3.08 m, 1.76 m) in which the tidal wave generation system is installed. Such system consists of an oleodynamic mechanism which moves an empty cylinder (diameter=1.1 m, length=2.8 m) according to a given temporal law. The oleodynamic system is computer controlled by means of a DAQ. The oscillation of the cylinder causes the displacement of the water from/to the feeding tank to/from the channel resulting in a tidal wave.
The length of the flume has obviously been determined by the size of the platform, the width of the channel has been chosen such to avoid the formation of free bars, a feature which we will focus on later. From the fluvial literature (Tubino, Repetto & Zolezzi, 1999), it is well known that the crucial parameter controlling the formation of bars in straight channels is the aspect ratio β defined as the ratio between the half width of the channel and the average flow depth. The formation of alternate bars in straight channels subject to a tidal current have been recently investigated by Seminara & Tubino (2000) by means of a stability analysis. The stability analysis provides a dispersion relationship for the growth rate and migration speed of the bars as functions of bar wavenumber, width ratio β, Shields parameter θ, particle Reynolds number R_p and relative roughness d_s^*/D_0^*. Such dispersion relationship allow to build neutral curves corresponding to perturbations with vanishing growth rate. An example of a neutral curve is reported in fig. 3.8. Note that such curve displays a minimum which is found to correspond to critical or threshold conditions for the formation of alternate bars. For values of β larger than the critical one, any perturbation characterized by a wavenumber falling within

the neutral curve is unstable, therefore bars will form. In the case of parameter values typical of our experimental conditions ($d_s = 3 \cdot 10^{-3}$, $R_p = 12$, peak value of Shields parameter = 0.43) the critical value of β is ranging about 5. At the initial stage our experiments displayed a β ranging about 1.5 which is below the critical value, therefore alternate bars should not form.

The length of the rectangular basin should have allowed the unsteady jet

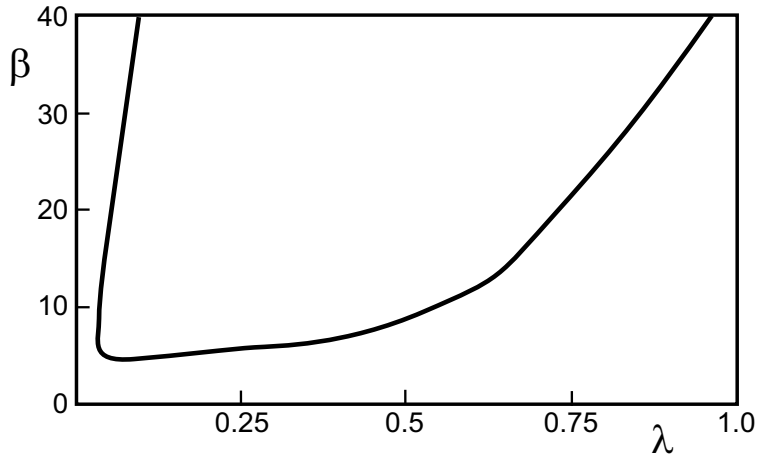

Figure 3.8: *Marginal stability curve for alternate bars (from Seminara & Tubino (2000)). Parameter values are:* $d_s = 2 \cdot 10^{-5}$, $R_p = 4$, *peak value of Shields parameter = 1*

forming in the basin during the ebb phase, to decay completely. However, space did allow to achieve such goal, hence we made sure that sediment discharged into the feeding tank were kept in suspension by the stirring action of recirculating water jets acting on the bottom of the tank. As a result no loss of sediment from the channel-basin system occurred throughout the experiment. A sketch and a picture of the channel are reported in fig. 3.9 and in fig. 3.10, respectively.

The first step of the present experimental investigation was to study the hydrodynamics of tide propagation along the channel. We therefore performed a first set of fixed bed experiments. We measured water velocity and water surface elevation in 5 cross sections placed every 6 m along the channel starting from the channel inlet, as indicated in fig. 3.9.

Water velocities were measured using a micropropeller, which has an accu-

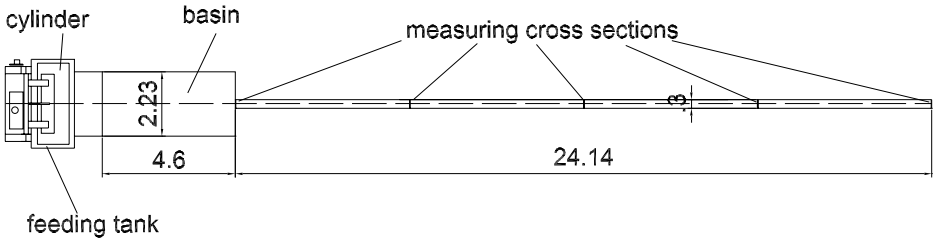

Figure 3.9: *Sketch of the experimental apparatus*

Figure 3.10: *View of the experimental apparatus*

racy of $\pm 1\%$ when the velocity falls in the range (0.15-1.5)m/s and it is characterized by a propeller diameter of 11.6 mm which needs to be located at least 15 mm below the free surface. The micropropeller was calibrated using a high resolution (0.1 mm/s) acoustic doppler velocimeter.
In order to determine the distribution of flow velocity we measured the flow speed at various points along the axis of symmetry of the cross sections. Unfortunately the diameter of the microproller does not allow to measure flow velocity in the nearest proximity of the bottom. Moreover, due to the fact that the propeller must be submerged for at least 15 mm and the tidal wave amplitude increased inward, the locations and number of the measuring points was not the same in any cross section. In section 2, the spatial distribution of flow velocity was determined by virtually dividing the cross section into 5 vertical

subsections; the velocity of the flow was then measured at 5 points along the vertical axis of each of the subsections for a total of 25 points.
In order to obtain a sufficient accuracy, at each point the velocity was monitored for a period of at least 12 tidal cycles, discarding the first two since the system required about two periods to reach 'stationary' conditions. The pattern of flow velocity over cross sections 1, 3 and 4 was determined by assuming a transverse distribution similar to that measured in section 2.
Water surface elevation was measured in the same cross sections in which we performed velocity measurements. We took measurements of free surface elevation at the channel axis employing ultrasonic sensors which have an accuracy of $\pm 0.172mm$.

A second set of experiments was performed with a mobile cohesionless bottom. Such experiments were devoted to made some preliminary observations of the formation and behavior of bedforms (such as dunes and possibly bars) and investigate the long term altimetric bed profile. The flume was then filled with crushed hazelnut shells characterized by a density of 1480 kg/m^3 and $D^*_{50} = 0.31$ mm. The sediment size distribution is reported in fig. 3.11. Such sediments were light and fine enough to produce a sufficiently large sediment flux throughout most of the tidal cycle with the values of friction velocities typically generated during the present experiments.

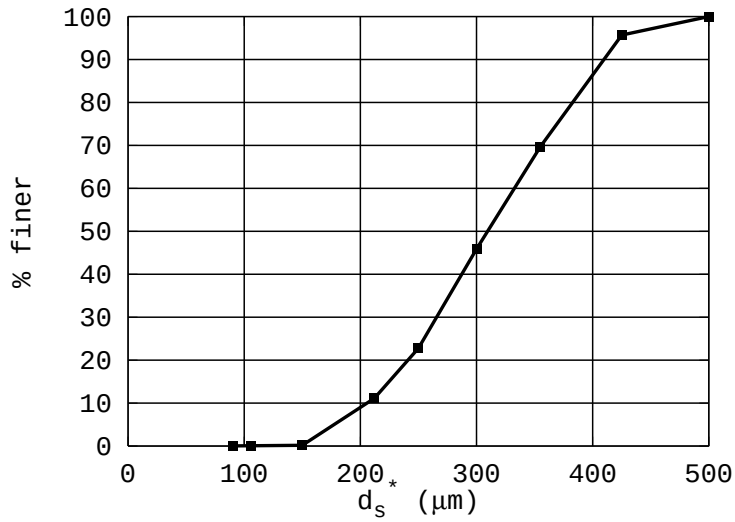

Figure 3.11: *Sediment size distribution*

The channel bed was prepared using a 0.30 m wide scraper attached to a carriage running along the rails. The bed was smoothed flat and set at a vanishing slope before each experiment.

3.5 Control of the wave generating system

The knowledge of the relationship between the motion of the cylinder inside the feeding tank and the oscillations of the surface level in the basin is crucial for planning the experimental tests. To solve this problem we apply the mass continuity equation to a control volume consisting of the feeding tank and the rectangular basin as shown in fig. 3.12. The problem is readily solved once

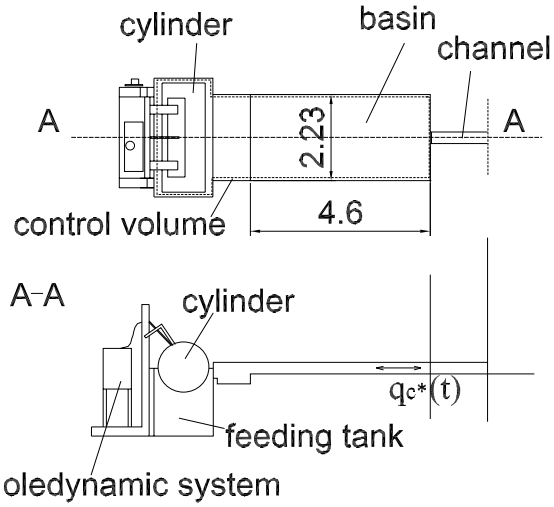

Figure 3.12: *Sketch and notations of control volume*

we give the kinematic characteristics of the tidal wave (period, amplitude and average depth), the size of the cylinder, the geometry of the control volume (feeding tank+basin) and the discharge $q_c^*(t)$ exchanged at any time between the control volume and the channel through its inlet section. Mass conservation applied to the control volume depicted in fig. 3.12, requires that the time derivative of the water volume contained in the feeding tank due to the oscillation of the cylinder, must equal the sum of the time derivative of the volume of water contained inside the basin due to the oscillation of the free surface

and of the water flux exchanged with the channel through the inlet section. The differential equation expressing such balance can be written in the form:

$$\frac{dV_i^*(t)}{dt^*} = [A_{tot}^* - A_c^*(t)] \frac{dD_0^*(t)}{dt^*} + q_c^*(t) \, , \tag{3.60}$$

where

$V_i^*(t)$: submerged volume of the cylinder;
A_{tot}^* : total free water surface area (feeding tank + rectangular basin);
$A_c^*(t)$: intersection between free water surface and oscillating cylinder;
$q_c^*(t)$: flow discharge exchanged through the channel inlet;

Notice that the discharge $q_c^*(t)$ can only be determined by solving the problem of propagation of the tidal wave inside the channel. Once $q_c^*(t)$ is known and the free surface elevation the basin $D_0^*(t)$ is assigned we can calculate the position of the cylinder in terms of its submerged volume. Notice that the equation (3.60) is in implicit form as the submerged volume $V_i^*(t)$ and the transverse area $A_c^*(t)$ both depend on the position of the cylinder, which is unknown.

The oscillations imposed to the cylinder during our experiments are shown in fig. 3.13 where they are compared with the theoretical law calculated by means of eq. (3.60). It can be seen that differences are relatively small ($\leq 15\%$).

3.6 Experimental observations

In this section we present some preliminary observations on the hydrodynamics and morphodynamics of our model of tidal channels.

3.6.1 Tidal wave hydrodynamics: the water surface elevation

As mentioned before (see section 3.4) we measured the free surface elevation at the channel axis in 5 cross sections. The oscillation of the free surface at the five locations along the flume is reported in fig. 3.14. Notice that the signal has been averaged over an extremely high number of tidal cycles (about 360).

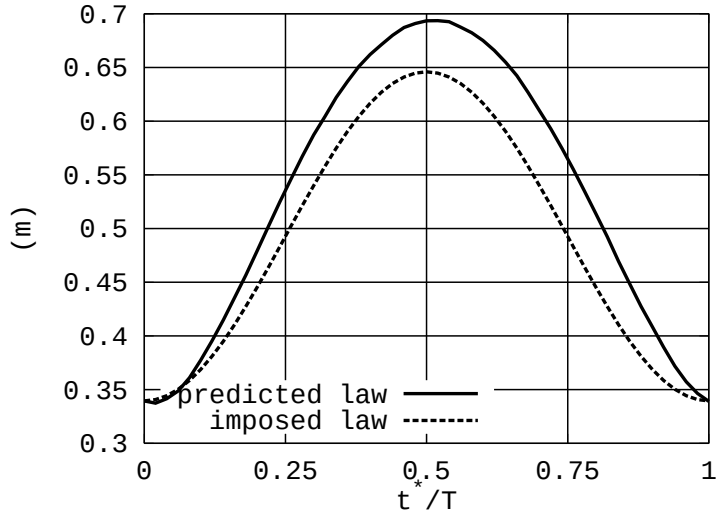

Figure 3.13: *The law of oscillation assigned to the cylinder is compared with the theoretical law calculated by solving eq. (3.60) numerically for given temporal dependence of free surface oscillations in the basin.*

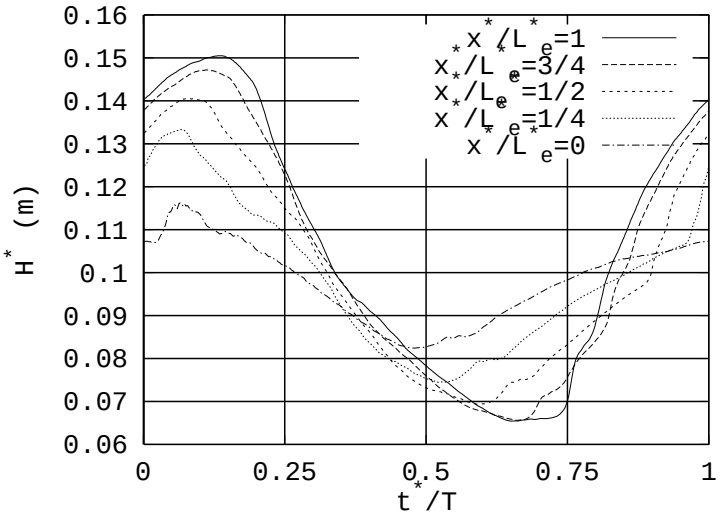

Figure 3.14: *Measurements of the free surface elevation in 5 cross sections*

As one may expect, the tidal wave amplitude grows in the landward direction, as shown in fig. 3.15, in which D_{max} (D_{min}) denotes the dimensionless highest (lowest) water elevation in each cross section while η is the dimensionless bottom profile.

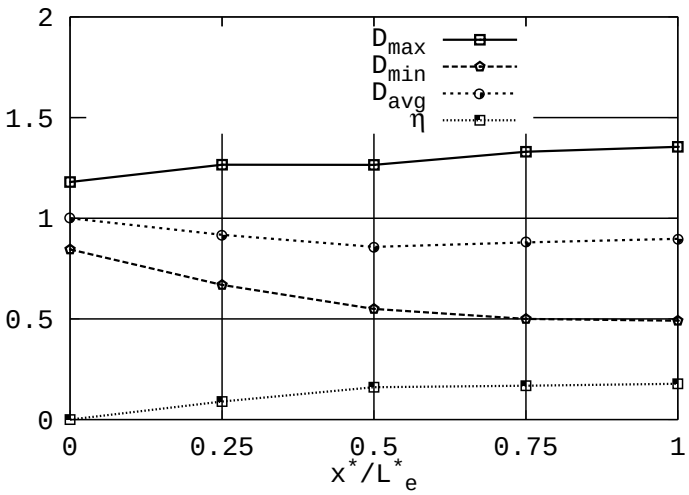

Figure 3.15: *The amplitude of tidal wave along the channel*

Note that the relative high value of the ratio convective inertial term/local inertial term is the cause of the sharp fronts observed in our experiments: such fronts can be detected in fig. 3.14. The free surface profiles predicted by the complete one dimensional model (see section 3.2.1) and by the linear model (see section 3.2.2) are compared with the experimental findings in figures 3.16, 3.17, 3.18, 3.19 and 3.20. It appears that the tidal wave amplitude is well predicted by the inviscid model, a result somewhat expected; the present model is indeed weakly dissipative, therefore the frictional term can hardly play a fundamental role.

Through a comparison between the water surface profiles measured and those calculated by means of the complete one dimensional model we have estimated the value of the flow conductance C. We have calibrated C employing the water surface elevation data rather than the velocity measurements since the former ones are more accurate. It appears that C takes a value of about 20, if we consider an average flow depth of about 10 cm the corresponding value of the Gauckler-Strickler parameter is about $100 m^{1/3} s^{-1}$, which appears to be

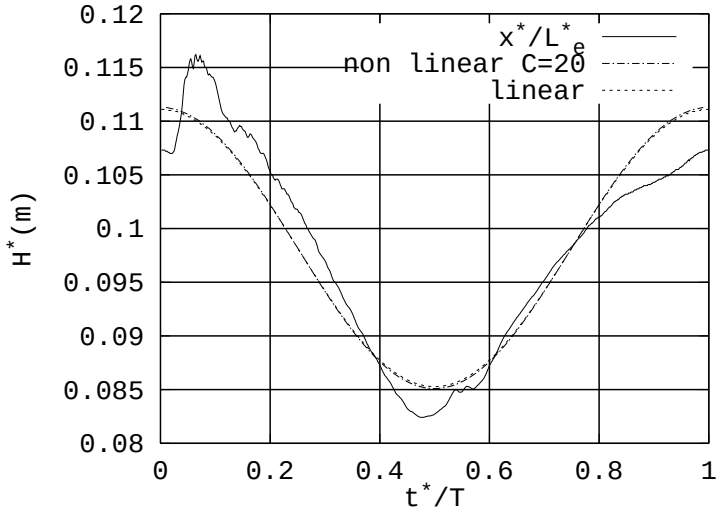

Figure 3.16: *The water surface elevation at cross section 1 as predicted by linear and nonlinear theory is compared with experimental findings*

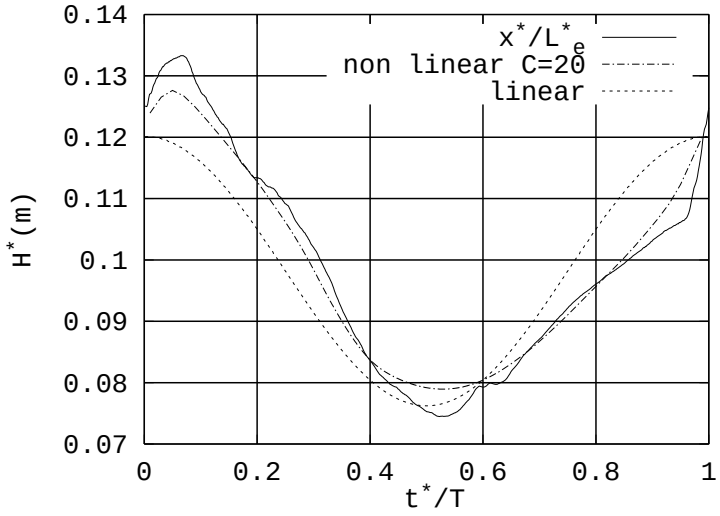

Figure 3.17: *The water surface elevation at cross section 2 as predicted by linear and nonlinear theory is compared with experimental findings*

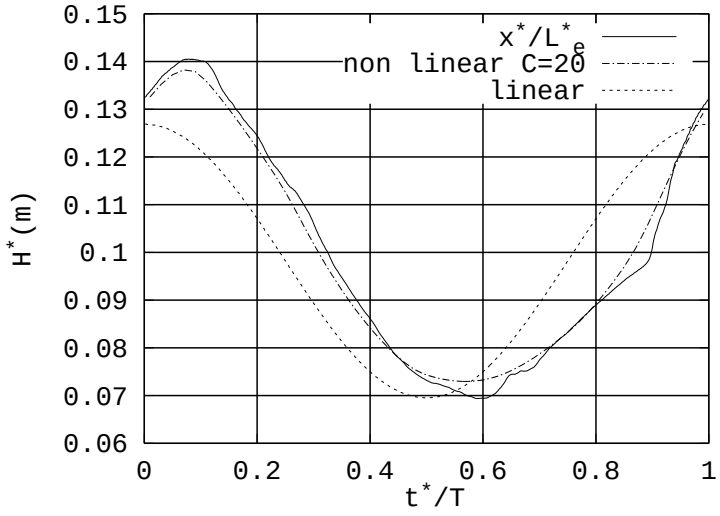

Figure 3.18: *The water surface elevation at cross section 3 as predicted by linear and nonlinear theory is compared with experimental findings*

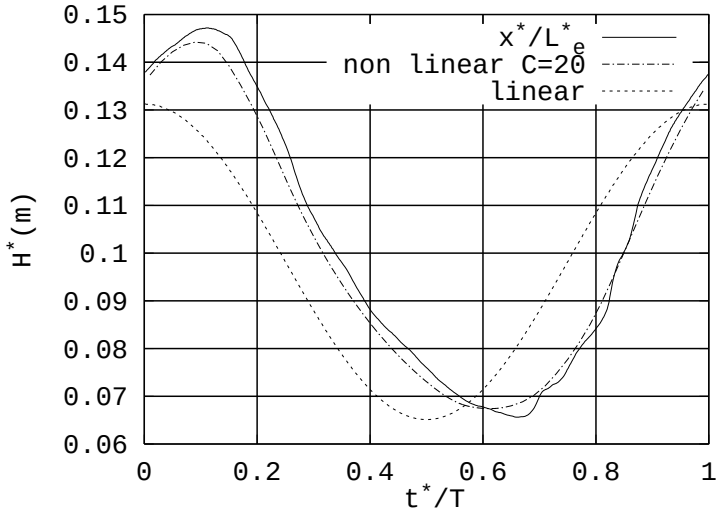

Figure 3.19: *The water surface elevation at cross section 4 as predicted by linear and nonlinear theory is compared with experimental findings*

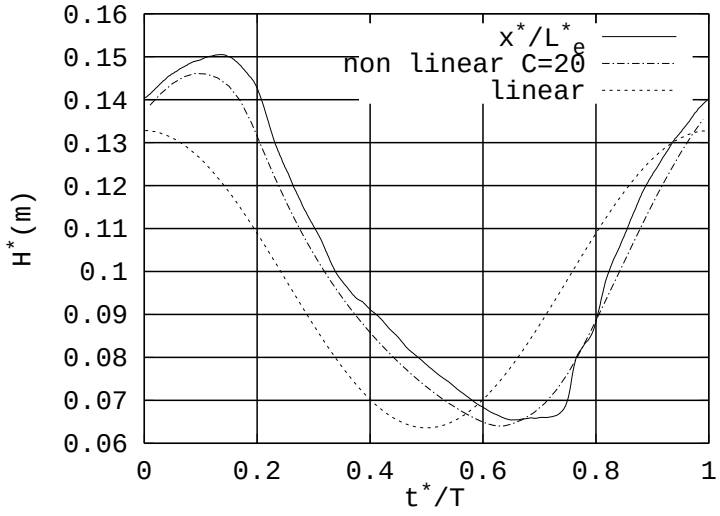

Figure 3.20: *The water surface elevation at cross section 5 as predicted by linear and nonlinear theory is compared with experimental findings*

reasonable for channels with very smooth walls. The corresponding value of the homogeneous wall roughness Υ^* is about 0.2 mm, while the peak value of the wall Reynolds number ranges about 3. Such value suggests that the wall is hydraulically smooth as the threshold value for hydraulically rough wall ranges about 20. To take into account the smooth character of the wall we then calculated the value of C employing Marchi's formula (1981) which can be used both in a rough and smooth regime; such formula reads:

$$C = -5.75log(\frac{C}{Re\phi} + \frac{\Upsilon^*}{13.3R_i^*\phi}) \,, \tag{3.61}$$

where ϕ denotes a shape factor (which for the present rectangular sections takes a value of 0.95), R_i^* is the hydraulic radius and $Re = \frac{4U^*R_i^*}{\nu}$ is the Reynolds number. It is important to note that C is not constant, but varies in time according to the temporal variations of the flow velocity, ranging from 20 when the flow velocity is at the peak to about 10 when the velocity is about 1 cm/s. In fact, during the tidal cycle the Reynolds number ranges from some maximum value (of about 10^5) to zero. Hence, approaching flow reversal, the flow tends to relaminarize.

3.6.2 Tidal wave hydrodynamics: the water speed

The distribution of the flow velocity averaged over the axis in cross sections 1,2,3 and 4 are reported in fig. 3.21. Note the distortion of the tidal velocity profile moving landward: while the ebb phase displays a longer duration, the peak of the flood velocity is higher. Such asymmetry becomes more pronounced approaching the landward boundary, as it is demonstrated in fig. 3.22 which shows the dimensionless maximum velocity U_{max} and minimum velocity U_{min} along the channel. It also appears that, moving upstream, the ratio $U_{max}/|U_{min}|$ increases (apart from the initial part of the channel where entrance effects are present), thus indicating that the flood dominated character increases upstream. Also note from fig. 3.21 that the duration of water slack following the flood phase increases upstream.

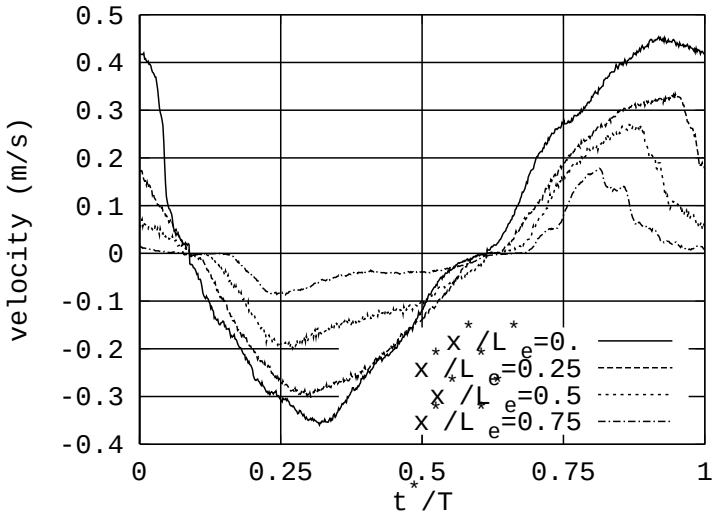

Figure 3.21: *The distribution of the vertically averaged flow velocity during a tidal cycle along the channel*

As mentioned in section 3.4 we evaluated the distribution of the water speed along the axis of 5 subsections at cross section 2. The results of such procedure are shown in fig. 3.23. Although small differences are displayed during the ebb phase, it appears that the velocity has an almost uniform distribution along the transverse axis

The cross sectionally averaged speed in sections 1,3 and 4 was calculated

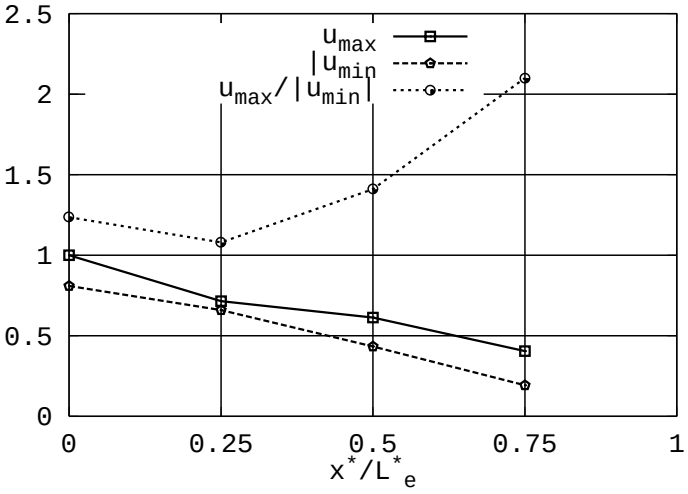

Figure 3.22: *The maximum and minimum velocity along the channel*

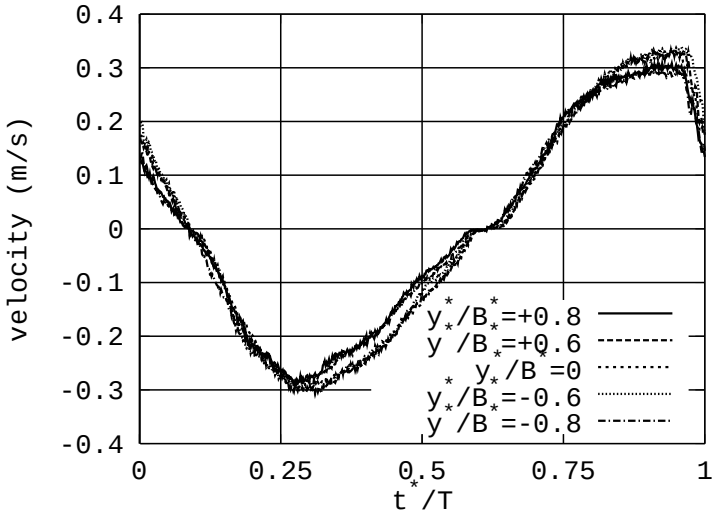

Figure 3.23: *The temporal distribution of the vertically averaged flow velocity at different locations throughout the cross section 2*

assuming a pattern of flow velocity similar to that observed in section 2. The mean velocity in section 1,2,3 and 4 as predicted by the shallow water equa-

tions (see section 3.2.1) and by the linear model (see section 3.2.2) is compared with the experimental findings in figures 3.24, 3.25, 3.26 and 3.27; respectively.

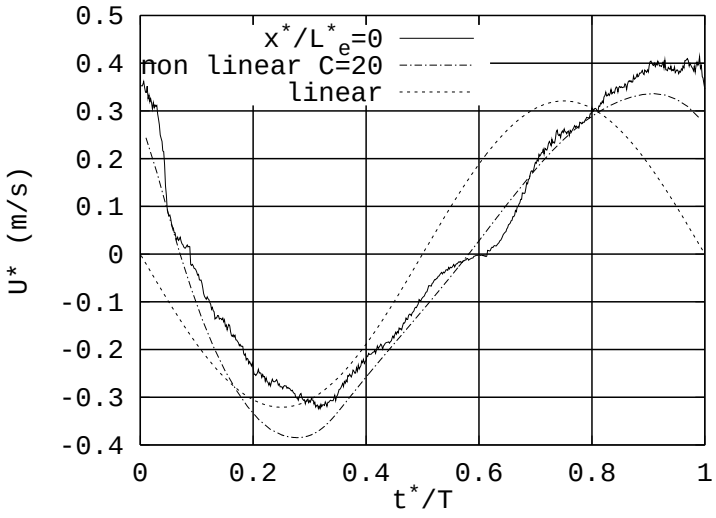

Figure 3.24: *The cross sectionally averaged flow speed at the channel inlet as predicted by linear and non linear theory is compared with the experimental findings.*

As previously discussed, during a large part of the tidal cycle the flow is turbulent and the wall exhibits a hydraulically smooth character. The vertical distribution of the flow speed is therefore expressed by the following relationship:

$$\frac{U^*}{u_*} = \frac{1}{k} \ln \left(\frac{z^*}{\Upsilon^*} \right) + 5.5 \, , \tag{3.62}$$

with $k = 0.41$ von Karman's constant, u_* friction velocity, Υ^* wall roughness and z^* vertical coordinate. Results obtained through the application of such formula have been compared with the experimental findings in figure 3.28: it appears that the logarithmic law agrees with the experimental results satisfactorily choosing a value for the flow conductance ranging about 20.

Finally notice that the experimental findings present a few irregularities well evident in the descending part of the flood phase (figures 3.26, 3.27). Such anomalies are due to wave trains displaying sharp fronts which travel throughout the channel (see picture 3.7).

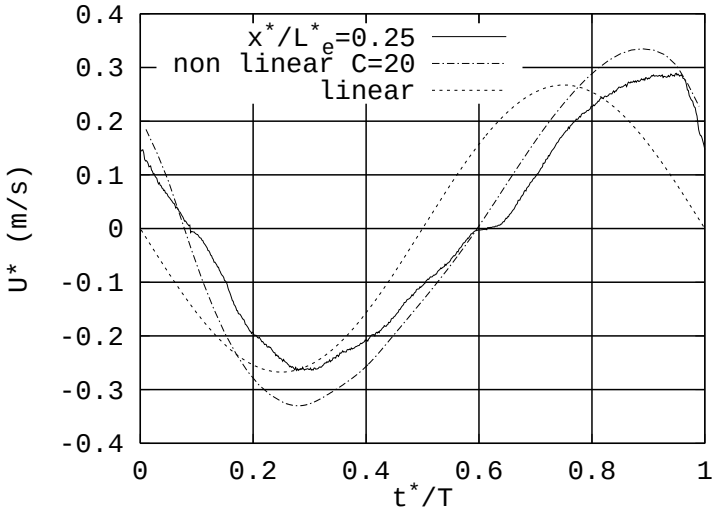

Figure 3.25: *The cross sectionally averaged flow speed at cross section 2 as predicted by linear and non linear theory is compared with the experimental findings.*

3.6.3 Tidal channel morphodynamics: preliminary observations

A first set of preliminary experiments has been performed to test the mechanism of sediment transport and the morphodynamic interactions between the current and the erodible bed. We did not take any quantitative measurements, so far, hence the discussion below is purely qualitative and simply aimed at designing adequately the future set of quantitative experiments. We have checked that the system is able to generate a current strong enough to bring the sediments in suspension throughout the most of the tidal cycle. At the channel inlet a large scour forms due to the sharp shape of the channel mouth and to the presence of a tidal induced jet (see section 3.6.4); such jet forms at the channel inlet during the ebb phase and excavates a channel inside the rectangular basin. The strength of such jet does not seem to decrease significantly during its propagation in the basin, as the jet is able to entrain sediments from the bottom of the basin. Consequently much sediment falls into the feeding tank where is located the oscillating cylinder. To avoid such process which would lead to a negative sediment budget at any tidal cycle, we have installed

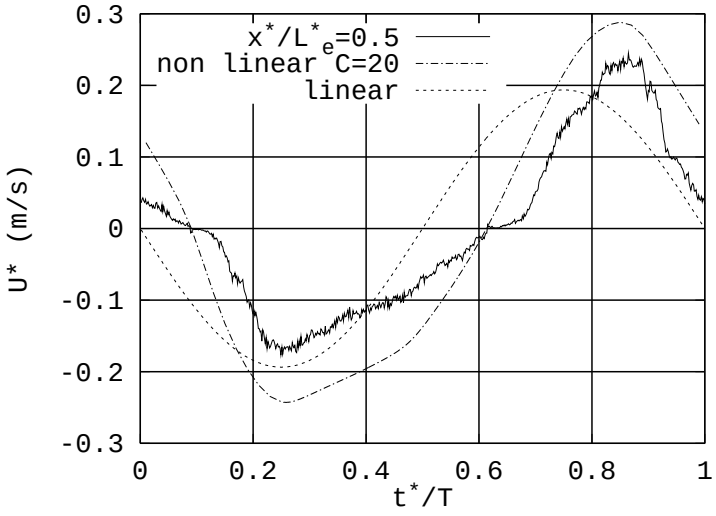

Figure 3.26: *The cross sectionally averaged flow speed at cross section 3 as predicted by linear and non linear theory is compared with the experimental findings.*

at the bottom of the feeding tank 4 water pumps able to create a circulation strong enough to prevent sediment from depositing at the bottom of the tank. The latter procedure insures that, at equilibrium, the sediment balance in the system channel+rectangular basin vanishes.
During the flood phase sediments inside the channel are flushed towards the land boundary, while in the rectangular basin the current is not strong enough to transport sediment in suspension, with the exception of the nearest proximity of the channel inlet where the convergence of streamlines induces higher speeds. After about some hours of experiments we can already distinguish a new bottom profile which exhibits a bed elevation increasing towards the landward boundary as predicted by Lanzoni & Seminara (2000)

The bed experiences also the formation of some bed forms, such as dunes fig. 3.29 and bars.

3.6.4 Experimental observations near the channel inlet

As mentioned before, the flow pattern inside the rectangular basin is essentially 2-D. We have visualized it using a white passive tracer consisting of a

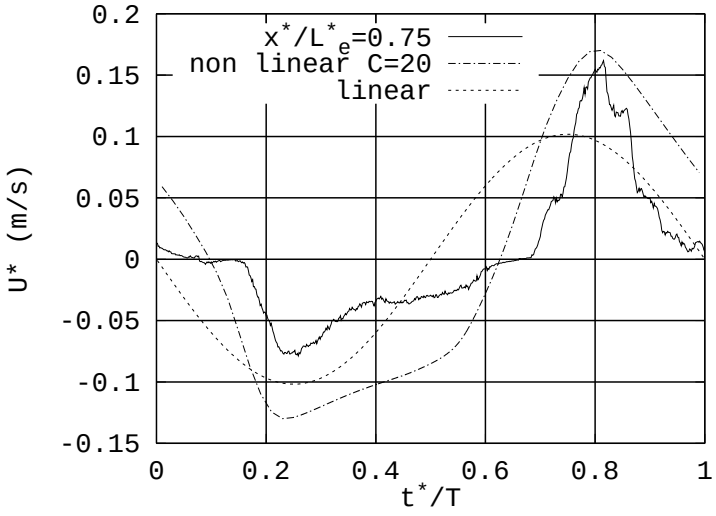

Figure 3.27: *The cross sectionally averaged flow speed at cross section 4 as predicted by linear and non linear theory is compared with the experimental findings.*

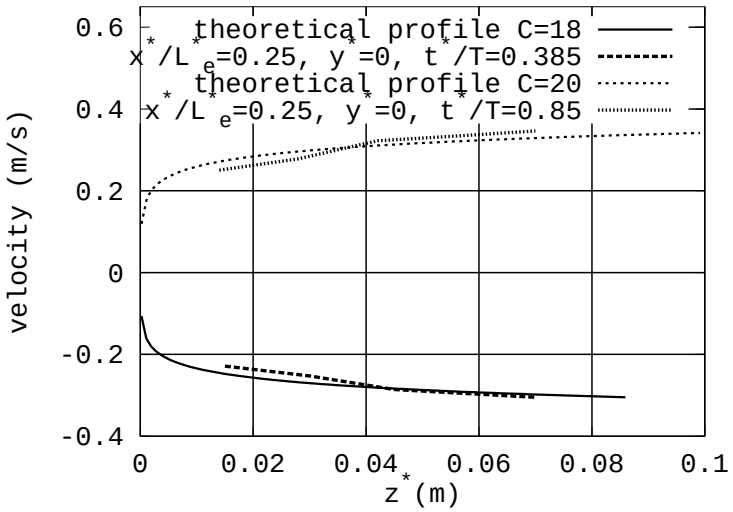

Figure 3.28: *The observed vertical distribution of flow velocity is compared with the theoretical distribution predicted from eq. (3.62)*

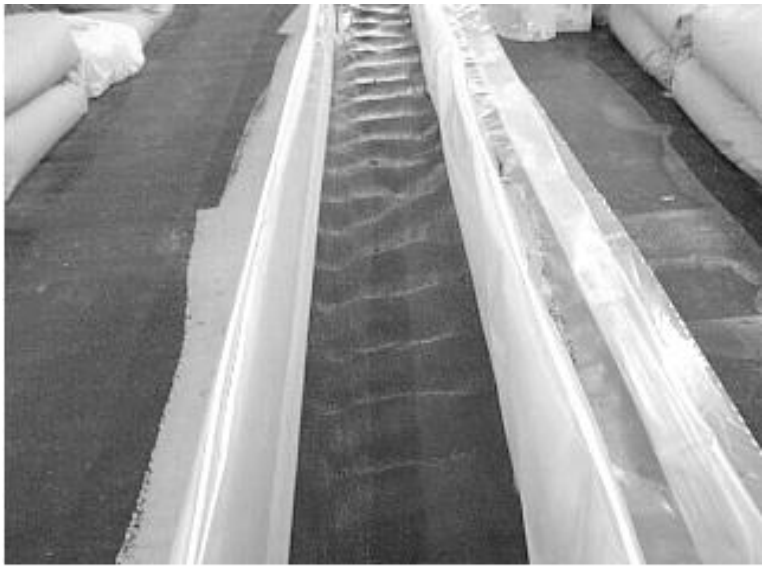

Figure 3.29: *Tidal dunes*

Figure 3.30: *The 2-D flow field pattern in the rectangular basin*

plastic powder, as illustrated in fig. 3.30. During the ebb phase an irregular pattern of whirling structures is displayed. The tidal jet exiting from the channel inlet is not straight, as shown in fig. 3.31, but curls to complete elliptical trajectories inside the rectangular basin, which are alternate in direction and verse, with respect to the tidal cycle. As a consequence of such circulation, during the flood phase water reenters the channel asymmetrically, with vor-

Figure 3.31: *Picture of the pattern of flow field during the ebb phase*

tex shedding mostly on one side of the inlet: in figure 3.33 the separation of vortices is more evident to the right, while, to show the alternate character of this phenomenon, the opposite case is illustrated in figure 3.32. Notice that the flow pattern inside the rectangular basin is drastically different during the flood and ebb phases; during the ebb phase flow is separated, flow separation is due primarily to the forcing effect of the momentum of the exiting jet, i.e. an unsteady jet forms with the jet expanding away from the inlet. On the contrary, during the flood phase, the flow is essentially irrotational and occurs in a sink-like manner. A theoretical description of such mechanisms was given by P. Blondeaux, B. De Bernardinis e G. Seminara (1986).

From a topographic map of the bottom in the rectangular basin (built plain) it seems that the curling of the tidal jet circulation is not induced by any altimetric factor. However we have observed that, after about 10 tidal

Figure 3.32: *Picture of the pattern of flow field during the flood phase. Notice the presence of vortexes in the left side of the channel inlet*

cycles, the tidal jet seems to maintain a straight configuration, as reported in fig. 3.34.

The asymmetric behavior of the tidal jet may be simply due to an instability phenomenon or it might be induced by the slightly asymmetric position, of the cylinder inside the feeding tank. Besides the cylinder axis is not perfectly horizontal. Further investigations are needed to clarify this point.

3.7 Conclusions and future developments

The present experimental apparatus successfully reproduces the hydrodynamic mechanisms commonly observed in tide dominated estuaries and tidal channels. A first set of experiments have been performed with fixed bed to investigate the propagation of the tidal wave throughout the channel. Measurements

Figure 3.33: *Picture of the pattern of flow field during the flood phase. Notice the presence of vortexes in the right side of the channel inlet*

of the flow field suggest that the present channel is flood dominated, as the velocity peak displayed by the tidal wave in the flood phase exceed the corresponding ebb value. Moreover, according to the classification proposed by Lanzoni & Seminara (1998), the present model can be classified as weakly dissipative as friction plays a negligible role relative to local inertia. As a consequence tide propagation can be treated as a weakly non linear phenomenon. Some qualitative observations of the interaction between the channel and the tidal sea indicate that the flow pattern in the rectangular basin during the ebb phase is drastically different from the pattern observed during the flood phase: during the ebb phase the flow separates due to the formation a tidal induced jet, whereas in the flood phase the flow is nearly irrotational.
A preliminary experiment aimed at studying the interaction between the tidal

Figure 3.34: *Detail of the flow field pattern during the ebb phase.*

current and the cohesionless bottom also suggests that the model is adequate to investigate the main features of morphodynamics of tidal channels.

The scaling rules reported in section 3.3 allows one to design physical models of tidal morphodynamics. The present physical model is affected by some distortions. In particular, in order to obtain a current strong enough to generate an appreciable transport in suspension with the size of the experimental apparatus, the period of the tidal wave cannot exceed about 200 s. Such constraint leads to an enhancement of the relative role played by the local inertia. As a consequence the model is more weakly dissipative than the prototype. Furthermore the convective inertia is higher in the model leading to the tendency of the tidal wave to display sharp fronts.

The present apparatus can be modified in the future to include some of the effects now neglected, e.g. the convergence of the channel and the presence of tidal flats.
Furthermore the present channel, straight and narrow, can be made wider and meandering since the platform on which the flume is built is 2.2 m wide. This will allow the formation of free and forced bars and investigate their effects on tidal morphodynamics.

References

Blondeaux, P., De Bernardinis B. & Seminara, G., Sul meccanismo di ricambio lagunare. Rep. B12/86. Istituto di Idraulica, Università di Genova, 1986.

Lanzoni, S. & Seminara, G., On tide propagation in convergent estuaries, *J. Geophys. Res.*, 103, C13, 793-812, 1998.

Lanzoni, S. & Seminara, G., Long term evolution and morphodynamic equilibrium of tidal channels, *J. Geophys. Res.*, submitted, 2000.

Marchi, E., L'Energia Elettrica, 38, nn. 4-5, 1961.

Parker, G., Self formed rivers with stable banks and mobile bed. Part l. The sand-silt river, *J. Fluid Mech.*, 89, 109-125, 1978.

Preissman, A., Propagation des intumescenes dans les canaux et riviers, *1st Congress de l'Association Francaise de Calcul*, Grenoble, France, 1961.

Seminara, G. & Tubino, M., Sand bars in tidal channels. Part one: free bars, *J. Fluid Mech.*, submitted, 2000.

Tubino, M., Repetto, R. & Zolezzi, G., Free bars in rivers, *J. Hydraul. Res.*, 37(6), 1999.

van Rijn, L.C., Sediment transport. Part Il. Suspended load transport, *J. Hydraul. Eng. ASCE*, 110(11), 1613-1641, 1984.

Part two

Topics in fluvial morphodynamics

Chapter 4

Bedload on arbitrarily sloping beds at low Shields stress

4.1 Introduction

Deterministic attempts to provide a theoretical description of bedload transport under uniform equilibrium conditions (Ashida & Michiue, 1972; Engelund & Fredsøe, 1976; Wiberg & Smith, 1985; Sekine & Kikkawa, 1992; Niño & García, 1994) invariably consist of two main steps.

In the former step an estimate of the average speed of saltating particles V_p is obtained either on the basis of an appropriate saltation model or, more simply, by ideally replacing the actual saltating motion by an equivalent uniform translatory motion such that the effects of particle rebound are accounted for in terms of a bulk dynamic coefficient of Coulomb friction. Though the use of saltation models provides a more complete picture of the bedload transport process, however the 'bulk' approach is sufficient to pick up the fundamental features of particle dynamics and leads to estimates for the average particle speed which are in reasonable agreement with experimental observations.

The second step is devoted to the evaluation of the average areal concentration C of saltating particles, i.e. the average volume of saltating particles

per unit area. This is a much more ambitious goal. In fact the number of particles in motion essentially depends on the spatial and temporal frequencies and on the intensity of near wall turbulent events (the so called sweeps and inward interactions) which are known (Heathershaw and Thorne, 1985, Thorne et al., 1989, Drake et al, 1988, Nelson et al., 1995) to be responsible for the entrainment of bedload particles. Estimating such frequencies and intensities under rough wall and mobile bed conditions is still outside the reach of present experimental techniques. Furthermore no model of the complex interaction between the near wall particles and such highly unsteady, spatially random, turbulent events has yet been proposed. The complexity of the detailed process has led Bagnold (1956) to attempt formulating a physically based assumption to estimate the average areal concentration C. Essentially Bagnold suggests that the external stress the fluid imposes at the upper edge of the saltation layer is reduced by the effect of the average reaction forces due to the presence of saltating particles to the extent that the average fluid residual stress acting at the bed interface equals the critical value for incipient particle motion. Such constraint determines the average number of saltating particles per unit area.

The rationale behind such assumption is based on a static notion of equilibrium of the bed interface: in other words, in order for the latter to keep in equilibrium, the residual average stress acting on the interface should reduce to the threshold value for the incipient motion of sediment particles. The validity of such assumption, which has been employed in virtually all the deterministic models of bedload transport appeared in the literature, has been questioned by Fernandez Luque and van Beek (1976) who performed detailed observations of the dynamics of saltating particles at fairly low Shields stress. For values of the latter stress smaller than about 0.1 the assumption appeared to fail. Similar doubts were shed by the more recent work of Niño et al. (1994). The question of the validity of Bagnold's hypothesis is then still the subject of debate and no conclusive evidence of either its validity or its failure can be claimed.

We wish to reexamine the latter issue in a more general context, namely that of bedload transport on arbitrarily sloping beds. Such problem is of great practical interest as most phenomena in river morphodynamics involve the motion of bedload particles on non planar beds. Recently Kovacs and Parker (1994) proposed a vectorial formulation of bedload transport able to cope with large local gradients of bed elevation. The analysis followed the line of

the classical approach of Ashida and Michiue (1972), which was extended to a general non planar bed configuration characterized by local slopes which may reach values up to the angle of repose of the sediment. The analysis of Kovacs and Parker (1994) employed a generalized form of Bagnold's assumption stipulating that the projection of the residual stress acting on the bed onto the direction of the external stress should be equal to the critical value for incipient motion. Such generalization is an approximate form of the exact generalization of Bagnold's condition which requires that the modulus of the residual stress vector must equal the critical stress.

In the present note we first investigate the consequences of the exact Bagnold's constraint. Such investigation gives rise to somewhat unexpected results. In fact it turns out that, for given particle Reynolds number and local longitudinal slope, Bagnold's condition can only be satisfied provided the local lateral slope does not exceed a fairly low threshold value depending on the applied Shields stress. Such finding has a simple physical explanation which will be given in sect. 4. As the applied Shields stress increases, the maximum allowed lateral slope decreases reaching values which range about few degrees. The implications of these results are somewhat striking: since equilibrium bedload transport can obviously occur on lateral slopes exceeding the threshold value discussed above, as experimental observations on bedload transport on transversely sloping beds clearly suggest (see in particular Ikeda, 1982), it then follows that Bagnold hypothesis cannot be valid.

In order to overcome the latter problem we then propose a simple approach based on a reinterpretation of the experimental observations of Fernandez Luque and van Beek (1976). The latter suggest that the equilibrium of the bed interface is dynamic rather than static, in that equilibrium is achieved through a balance between an entrained sediment flux and a deposited flux. A simple calculation based on Fernandez Luque and van Beek's results allows one to determine an approximate relationship between the excess residual stress acting at the bed interface (i.e. the difference between the residual stress and its critical value) and the excess applied stress. Such relationship turns out to be fairly close to linear, at least within the relatively narrow range of values investigated by Fernandez Luque and van Beek (1976). Having established such relationship, the average areal concentration of saltating particles, which is readily calculated in terms of the excess applied stress on the basis of the experimental results, can also be expressed in terms of the excess residual stress. It is then reasonable to assume that the relationship between

the areal concentration and the excess residual stress established from uniform flow experiments on planar beds can be extended to flow on arbitrarily sloping beds provided the modulus of the residual stress is correctly evaluated by performing a vectorial difference between the external stress and the stress associated with the average drag acting on saltating particles, the latter being no longer aligned with the former. Such assumption, which essentially consists of assuming that it is the modulus of the excess residual stress which measures in some sense the ability of the stream to entrain sediments, replaces Bagnold's assumption and allows one to derive a general relationship for bedload transport on arbitrarily sloping beds.

The procedure followed in the rest of the paper is as follows. In the next section we rederive the threshold condition for particle motion on an arbitrarily sloping bed. In Section 3 we determine a relationship for the intensity and direction of the average speed of saltating particles on arbitrarily sloping beds. In Section 4 we reinforce Bagnold's condition in order to evaluate the average areal concentration of saltating particles and show that the latter condition leads to contradictory conclusions predicting that a threshold value of the lateral slope exists above which Bagnold's constraint cannot be satisfied. Section 5 is devoted to the approach proposed in the present paper to replace Bagnold's assumption. Results based on the latter approach are discussed in the last section.

4.2 The threshold condition for the motion of bedload particles on arbitrarily sloping beds

A derivation of the threshold conditions for the motion of bedload particles on arbitrarily sloping beds was proposed by Kovacs and Parker (1994). Here we essentially follow their approach with some minor modifications. We consider a free surface flow on a non planar cohesionless bed and refer to fig. 4.1 for notations. Let P be a point lying on the bed and let z be the coordinate of a vertical axis with origin in P and unit vector $\hat{\boldsymbol{k}}$. Let the flow exert a tangential stress on the bed. The direction of such stress, along with the vertical direction, provide the only two externally imposed directions on the problem: in particular note that the direction of channel axis does not play any role in the present analysis. It is then convenient to introduce a right handed cartesian reference frame, centered at P, with coordinates x_τ, x_p and z. The x_τ axis

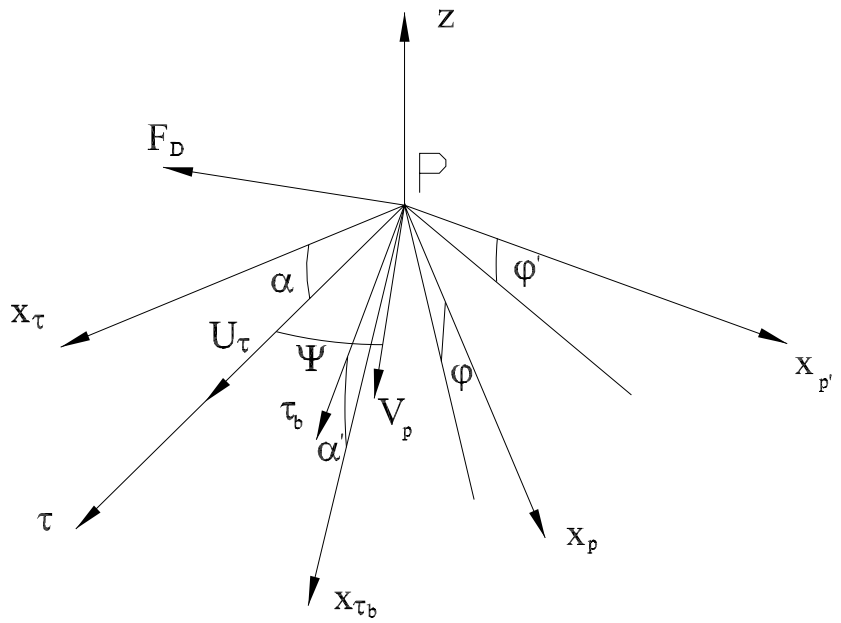

Figure 4.1: *Sketch and notations*

(with unit vector $\hat{\boldsymbol{x}}_\tau$) is the horizontal axis lying in the vertical plane $(\boldsymbol{\tau}, \hat{\boldsymbol{k}})$, while the x_p axis (with unit vector $\hat{\boldsymbol{x}}_p$) is the horizontal axis orthogonal to the plane $(\hat{\boldsymbol{x}}_\tau, \hat{\boldsymbol{k}})$. Let us now define a streamwise and a lateral slope of the bed as follows. The equation of the bed surface may be written in the form:

$$F_b = z - \eta(x_\tau, x_p) = 0 \ , \tag{4.1}$$

with η bed elevation. The unit vector in the direction normal to the bed reads:

$$\hat{\boldsymbol{n}} = \frac{\nabla F_b}{|\nabla F_b|} \ . \tag{4.2}$$

The vertical unit downward vector -$\hat{\boldsymbol{k}}$ is decomposed into normal $(\boldsymbol{k}_n)$ and tangential $(\boldsymbol{k}_t)$ components as follows:

$$\boldsymbol{k}_n = (-\hat{\boldsymbol{k}} \cdot \hat{\boldsymbol{n}})\hat{\boldsymbol{n}} \ , \qquad \boldsymbol{k}_t = -\hat{\boldsymbol{k}} - \boldsymbol{k}_n \ . \tag{4.3}$$

The streamwise slope of the bed at $P(\tan\alpha)$ is then defined as the slope of the line obtained by intersecting the bed surface with the plane $(\hat{\boldsymbol{k}}, \hat{\boldsymbol{x}}_\tau)$:

$$\tan\alpha = -\frac{\partial \eta}{\partial x_\tau} \ . \tag{4.4}$$

Similarly the lateral slope of the bed at $P(\tan\varphi)$ is the slope of the line obtained by intersecting the bed surface with the plane $(\hat{\boldsymbol{k}}, \hat{\boldsymbol{x}}_p)$ and reads:

$$\tan\varphi = -\frac{\partial\eta}{\partial x_p} \,. \tag{4.5}$$

Note that the above two lines are not orthogonal to each other in general. Having set the above notations we may now formulate the threshold condition for particle motion as follows:

$$\left| F_D \frac{\boldsymbol{\tau}}{|\boldsymbol{\tau}|} + (G-A)\boldsymbol{k}_t \right| = \mu |(G-A)\boldsymbol{k}_n + L\hat{\boldsymbol{n}}| \,, \tag{4.6}$$

having denoted by G the particle weight, by A the Archimedean force, by F_D the intensity of the drag force and by L the intensity of the lift force acting on the particle. In words we require that the resultant active force must balance the resistive force expressed in terms of a friction coefficient μ interpreting the effect of contact forces between the particle located at P and adjacent particles.

The latter expression can be reduced to a simple algebraic equation for the critical Shields stress by performing some simple algebraic manipulations. Let us first express the intensities of drag and lift forces in terms of drag and lift coefficients as follows:

$$F_D = \frac{1}{2}\varrho c_D \frac{\pi D^2}{4} u_0^2 \,, \tag{4.7}$$

$$L = \varrho \mathcal{V} c_L u_0 \left. \frac{du_0}{d\zeta} \right|_{\zeta_p} \,, \tag{4.8}$$

where u_0 is the mean fluid speed at the distance ζ_p from the wall where the particle centroid is located, D is particle diameter, $\mathcal{V}$ is particle volume, ρ is water density while c_L and c_D are drag and lift coefficients which require some estimates.

The reader will note that the expression (4.8) for the lift force differs from that employed in previous analyses of incipient particle motion. Indeed, though the hydrodynamic process which determines the average force acting on spheres lying on granular beds and subject to the action of turbulent shear flows is far too complex to be amenable to rigorous theoretical investigations,

however a considerable progress has been made in the last decade on the subject of the hydrodynamic forces acting on spheres immersed in an unbounded inviscid spatially and temporally varying flow in the presence of vorticity. In particular Auton (1987) has shown that, provided the strength of vorticity is weak, i.e. the change in incident velocity across the sphere is much smaller than the relative speed of the ambient flow at the centre of the sphere, the lift force $\boldsymbol{F}_L$ for a sphere at rest in a weakly rotational inviscid flow reads:

$$\boldsymbol{F}_L = -\varrho c_L \boldsymbol{v}_0 \times \boldsymbol{\omega} \,, \tag{4.9}$$

with $\boldsymbol{\omega}$ uniform ambient vorticity and c_L lift coefficient which takes the value 0.5. The above result was generalized by Auton, Hunt and Proudhomme (1988) who showed that the form (4.9) for the lift force is still valid when the ambient flow, besides being weakly sheared, is also slowly varying in space and time. Though a sphere lying on a cohesionless granular bed is subject to a strongly rather than weakly sheared ambient flow and viscous effects as well as the presence of the wall play a non negligible role, it appears that the expression (4.9) is the most reasonable form which may be envisaged for the lift force. We have estimated the value of c_L by reinterpreting Chepil's (1958) set of data, which is based on the possibly most reliable experimental work on the lift force acting on spheres lying on granular beds. Note that Chepil (1958) employed hemispheres set in a hexagonal pattern, three diameters apart center to center, with fine gravel covering the floor between them. Fig. 4.2 shows the results of such reinterpretation. It is interesting to note that values of c_L increase as the Reynolds number increases and, at the higher Reynolds numbers, reach values ranging about the theoretical value 0.5 appropriate to inviscid and weakly sheared unbounded ambient flows. In the following we will then assume such value for the lift coefficient. It is appropriate at this stage to point out that the formulation for the lift force proposed by Wiberg and Smith (1985) reduces to the present formulation if the velocity distribution of the incident flow is assumed to vary linearly across the sphere.

An explicit form for the threshold condition of particle motion (4.6) can finally be derived using the following relationships:

$$\hat{\boldsymbol{n}} = \frac{(\tan\alpha, \tan\varphi, 1)}{\sqrt{1 + \tan^2\alpha + \tan^2\varphi}} \,, \qquad \hat{\boldsymbol{k}} = (0, 0, 1) \,, \tag{4.10}$$

$$\boldsymbol{k}_n = -\frac{(\tan\alpha, \tan\varphi, 1)}{1 + \tan^2\alpha + \tan^2\varphi} \,, \qquad \boldsymbol{k}_t = \frac{(\tan\alpha, \tan\varphi, -\tan^2\alpha - \tan^2\varphi)}{(1 + \tan^2\alpha + \tan^2\varphi)} \,, \tag{4.11}$$

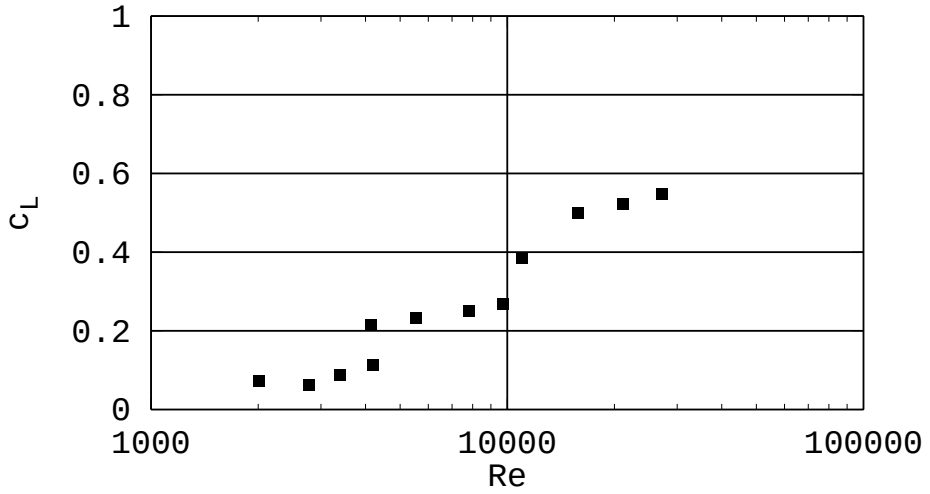

Figure 4.2: *The value of the lift coefficient c_L, estimated from Chepil's (1958) data, is plotted as a function of Reynolds number.*

$$\frac{\boldsymbol{\tau}}{|\boldsymbol{\tau}|} = (\cos\alpha, 0, -\sin\alpha) \ . \tag{4.12}$$

Substituting from (4.7-4.12) into (4.6) and dividing by $(\rho_s - \rho)gD$, ρ_s being the sediment density, we find:

$$\left| \frac{1}{2} c_D f^2 \frac{\pi D^2}{4} \tau_{*c} (\cos\alpha, 0, -\sin\alpha) + \frac{\mathcal{V}}{D} \frac{(\tan\alpha, \tan\varphi, -\tan^2\alpha - \tan^2\varphi)}{(1 + \tan^2\alpha + \tan^2\varphi)} \right| =$$
$$= \mu \left| \frac{\mathcal{V}}{D} \frac{(-\tan\alpha, -\tan\varphi, -1)}{(1 + \tan^2\alpha + \tan^2\varphi)} + c_L \mathcal{V} f \left. \frac{df}{d\zeta} \right|_{\zeta_p} \tau_{*c} \frac{(\tan\alpha, \tan\varphi, 1)}{\sqrt{1 + \tan^2\alpha + \tan^2\varphi}} \right| , \tag{4.13}$$

where f is the dimensionless form of the incident velocity distribution scaled by the friction velocity u_τ and ζ is a coordinate normal to the wall. In practice f can be written in the general form

$$f = \frac{1}{k} \ln(B \frac{\zeta}{K_s}) \ , \tag{4.14}$$

where $k = 0.4$ is the von Karman constant, K_s is a roughness height typically specified as

$$K_s = n_k D \ , \tag{4.15}$$

and n_k is an order-one constant. Moreover B is a function of friction Reynolds number $u_\tau K_s/\nu$ where ν denotes the kinematic viscosity of water. In the case for which $u_\tau K_s/\nu$ is sufficiently large B obtains the limiting value of 30 corresponding to a rough turbulent wall flow.
Let us denote by Δ and τ_{*c0} the following quantities:

$$\tau_{*c0} = \frac{4}{3}\frac{\mu}{c_D}\left[f^2|_{\zeta=\zeta_p}(1+\Delta)\right]^{-1} , \qquad \Delta = \frac{4}{3}\mu\frac{c_L}{c_D}\frac{D}{f}\left.\frac{df}{d\zeta}\right|_{\zeta=\zeta_p} , \tag{4.16}$$

where τ_{*c0} is the critical value of the Shields stress for vanishing α and φ.

Dividing equation (4.13) by τ_{*c0} and using equation (4.16) after some manipulations we obtain:

$$\left(\frac{\tau_{*c}}{\tau_{*c0}}\right)^2 + 2\frac{(1+\Delta)}{\mu}\sin\alpha\frac{\tau_{*c}}{\tau_{*c0}} + \\ + \left(\frac{1+\Delta}{\mu}\right)^2 \frac{tan^2\alpha + \tan^2\varphi + (\tan^2\alpha + \tan^2\varphi)^2}{(1+\tan^2\alpha+\tan^2\varphi)^2} = \\ = \frac{(1+\Delta)^2}{1+\tan^2\alpha+\tan^2\varphi} - 2\frac{\Delta(1+\Delta)}{\sqrt{(1+\tan^2\alpha+tan^2\varphi)}}\frac{\tau_{*c}}{\tau_{*c0}} + \Delta^2\left(\frac{\tau_{*c}}{\tau_{*c0}}\right)^2 . \tag{4.17}$$

Finally we end up with the following relationship:

$$(1-\Delta)\left(\frac{\tau_{*c}}{\tau_{*c0}}\right)^2 + 2\left\{\frac{\Delta}{\sqrt{1+\tan^2\alpha+\tan^2\varphi}} + \frac{\sin\alpha}{\tan\phi}\right\}\frac{\tau_{*c}}{\tau_{*c0}} + \\ \frac{(1+\Delta)}{1+\tan^2\alpha+\tan^2\varphi}\left(-1+\frac{\tan^2\alpha+\tan^2\varphi}{\tan^2\phi}\right) = 0 . \tag{4.18}$$

The equation (4.18) is immediately solved for (τ_{*c}/τ_{*c0}). Fig. 4.3 shows the dependence of the latter quantity on the lateral slope for given values of the longitudinal slope. Note that the calculations were performed assuming the value of 40° for the angle of repose ϕ of the particle.

4.3 The direction and intensity of the velocity of saltating particles in motion on arbitrarily sloping beds

Due to the sloping character of the bed, the average direction of particle motion deviates from the direction of the average bottom stress, while its average intensity changes with respect to the corresponding value for rectilinear mean flow.

We wish to derive estimates for both the intensity and direction of particle velocity. To this aim, following a fairly well established approach developed for the rectilinear case, we assume that the averaged particle dynamics is governed by an averaged balance between an average active force, obtained from

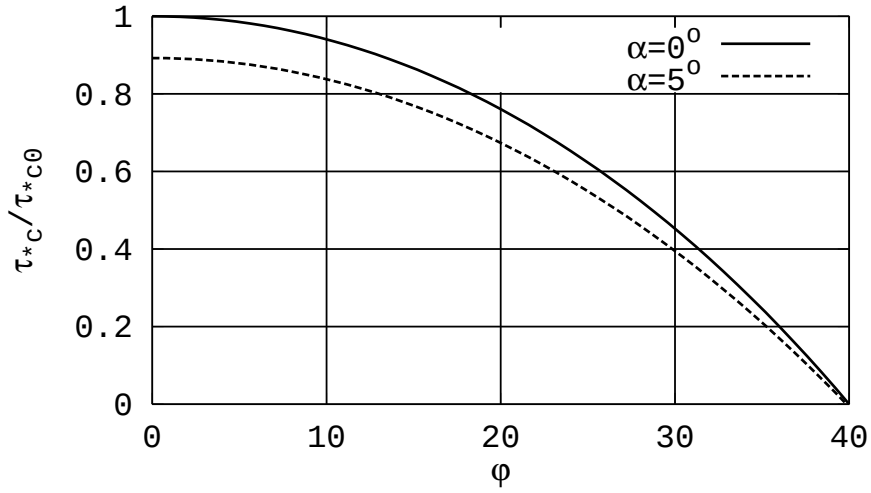

Figure 4.3: *The critical Shields stress τ_{*c} scaled by the critical Shields stress for an horizontal bed τ_{*c0} is plotted versus the lateral bed inclination φ for different values of the longitudinal bottom inclination α ($\phi = 40°, c_L/c_D = 1.25$, $c_D = 0.4$, $\zeta_p/K_s = 0.5$, $\tau_{*c0} = 0.032$).*

the vectorial composition of the drag force and the tangential component of the submerged particle weight, and an averaged resistive force, which interprets the effect of continuous or intermittent hydrodynamic interactions of particles with the bed and is aligned with particle velocity.

With the notations of fig. 1, we may write such balance in the form:

$$\boldsymbol{F}_D + (G - A)\boldsymbol{k}_t = +\mu_d(G - A)|\boldsymbol{k}_n|\frac{\boldsymbol{V}_p}{|\boldsymbol{V}_p|} \ . \tag{4.19}$$

Here the drag force $\boldsymbol{F}_D$ is a vector aligned with the relative fluid-particle velocity which reads:

$$\boldsymbol{F}_D = \frac{1}{2}\varrho c_D \left(\frac{\pi D^2}{4}\right)(\boldsymbol{U}_\tau - \boldsymbol{V}_P)|\boldsymbol{U}_\tau - \boldsymbol{V}_P| \ , \tag{4.20}$$

where $\boldsymbol{U}_\tau$ is the component of particle velocity tangential to the bed surface and $\boldsymbol{V}_P$ is particle velocity, a vector tangent to the bed which may be expressed in terms of the angle ψ that $\boldsymbol{V}_P$ forms with the bottom stress vector as follows:

$$\boldsymbol{V}_P = V_P \cos\psi \frac{\boldsymbol{\tau}}{|\boldsymbol{\tau}|} + V_P \sin\psi \left(\hat{\boldsymbol{n}} \times \frac{\boldsymbol{\tau}}{|\boldsymbol{\tau}|}\right) \ . \tag{4.21}$$

Recalling equation (4.12) and noting that :

$$\hat{\boldsymbol{n}} \times \frac{\boldsymbol{\tau}}{|\boldsymbol{\tau}|} = \frac{(-\sin\alpha\tan\varphi, \frac{1}{\cos\alpha}, -\cos\alpha\tan\varphi)}{\sqrt{1+\tan^2\alpha+\tan^2\varphi}} , \tag{4.22}$$

we may finally project equation (4.19) into the directions of $\hat{\boldsymbol{\tau}}$ and $\hat{\mathbf{n}} \times \frac{\boldsymbol{\tau}}{|\boldsymbol{\tau}|}$. This allows us to derive two scalar relationships for V_P and ψ in implicit form. They read:

$$\hat{V_p} = \frac{V_p}{\sqrt{(s-1)gD}} = f_p \sqrt{\tau_*}\, A(\psi;\alpha,\varphi) , \tag{4.23}$$

$$f_p\sqrt{\tau_*} = \sqrt{\frac{4}{3c_D}}\, \frac{(\cos\alpha\tan\varphi - \mu_d\sin\psi)^{1/2}}{[(1+A'^2)(1+\tan^2\alpha+\tan^2\varphi)]^{1/4}} \left(A' + \frac{1}{\tan\psi}\right) . \tag{4.24}$$

Here f_p is the function f introduced above, evaluated at some average saltation height. Moreover the quantities A and A' read:

$$A = (\cos\psi + \sin\psi A')^{-1} , \tag{4.25}$$

$$A' = \frac{\mu_d\cos\psi - \sin\alpha\sqrt{1+\tan^2\alpha+\tan^2\varphi}}{\cos\alpha\tan\varphi - \mu_d\sin\psi} . \tag{4.26}$$

The two relationships (4.23) and (4.24) have been solved for ψ and V_p by using an iterative procedure. Results for the angle ψ as a function of the applied Shields stress are reported in fig. 4.4. Note that, not surprisingly, the deviation of particle motion from the direction of the applied stress decreases as the Shields stress increases, an important feature which is known to be quite relevant to the process of lateral sorting in meander bends (Parker and Andrews, 1985).

4.4 Estimating the average areal concentration of saltating particles by Bagnold's hypothesis: an approach which leads to unrealistic results

Let us now investigate the consequences of imposing Bagnold's constraint on the dynamics of saltating particles.

To this aim we impose the dynamic equilibrium of a volume of fluid-sediment mixture adjacent the unit area of the bed surface, with height equal

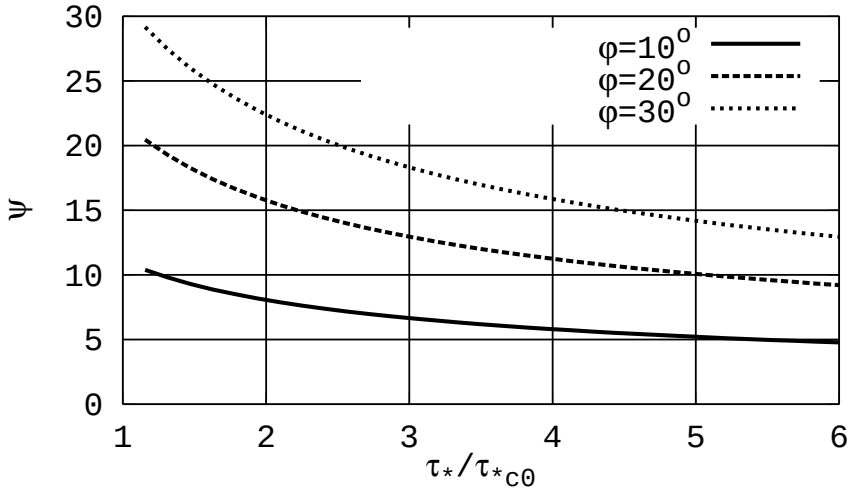

Figure 4.4: *The angle ψ, which measures the deviation of particle velocity relative to bottom stress, is plotted as a function of the local Shields stress τ_* for given values of the angles α and φ ($\phi = 40°, c_L/c_D = 1.25$, $c_D = 0.4$, $\tau_{*c0} = 0.032$, $f_p = 11.5$, $\mu_d = 0.6$).*

to the characteristic thickness of the saltation layer. Let us denote by $\boldsymbol{\tau}_B$ the shear stress acting on the upper surface of the control volume and by $(-\boldsymbol{\tau}_b)$ the residual shear stress that the fluid exerts on the bed surface. If the average volumetric concentration of saltating particles per unit area is denoted by C, then the average dynamic equilibrium of the control volume imposes the following condition:

$$\boldsymbol{\tau}_B + (h_s - C)\varrho g \boldsymbol{k}_t + \left(\frac{C}{\mathcal{V}}\right) \varrho_s g \mathcal{V} \boldsymbol{k}_t - \frac{C}{\mathcal{V}} \boldsymbol{R} = \boldsymbol{\tau}_b \, . \tag{4.27}$$

Noting that the quantity $\boldsymbol{\tau}_B + \varrho g h_s \boldsymbol{k}_t$ equals the clear water bottom stress $\boldsymbol{\tau}$ and recalling the condition (4.19), simple manipulations allow to transform equation (4.27) into the following form:

$$\boldsymbol{\tau} - \frac{C}{\mathcal{V}} \boldsymbol{F}_D = \boldsymbol{\tau}_b \, . \tag{4.28}$$

The exact generalization of Bagnold's hypothesis then poses the following constraint:

$$\frac{|\boldsymbol{\tau}_b|}{\varrho(s-1)gD} = \tau_{*c}(\alpha', \varphi') \, , \tag{4.29}$$

where τ_{*c} is the critical Shields stress associated with longitudinal slope $\tan(\alpha')$ and lateral slope $\tan(\varphi')$, having denoted by α' and φ' the values of α and φ associated with the residual stress vector $\boldsymbol{\tau}_b$ defined by equation (4.28). Evaluating such angles requires some tedious, though straightforward, algebraic manipulations.

Let us denote by $\hat{\boldsymbol{x}}_{\tau_b}$ the unit vector of the horizontal axis obtained by projecting the residual shear stress vector $\boldsymbol{\tau}_b$ into the horizontal plane through P. Moreover let $\hat{\boldsymbol{x}}'_p$ denote the unit vector of the horizontal axis orthogonal to $\hat{\boldsymbol{x}}_{\tau_b}$. We may then write:

$$\tan\alpha' = -\boldsymbol{\nabla}\eta\cdot\hat{\boldsymbol{x}}_{\tau_b}\ , \qquad \tan\varphi' = -\boldsymbol{\nabla}\eta\cdot\hat{\boldsymbol{x}}'_p\ . \tag{4.30}$$

Furthermore, we may write:

$$\hat{\boldsymbol{x}}_{\tau_b} = \frac{(\hat{\boldsymbol{k}}\times\boldsymbol{\tau}_b)\times\hat{\boldsymbol{k}}}{|(\hat{\boldsymbol{k}}\times\boldsymbol{\tau}_b)\times\hat{\boldsymbol{k}}|}\ , \qquad \hat{\boldsymbol{x}}'_p = \frac{\hat{\boldsymbol{k}}\times\boldsymbol{\tau}_b}{|\hat{\boldsymbol{k}}\times\boldsymbol{\tau}_b|}\ , \tag{4.31}$$

or, with the use of equation (4.28):

$$\hat{\boldsymbol{x}}_{\tau_b} = \frac{(\hat{\boldsymbol{k}}\times\boldsymbol{\tau})\times\hat{\boldsymbol{k}} - \frac{C}{\mathcal{V}}(\hat{\boldsymbol{k}}\times\boldsymbol{F}_D)\times\hat{\boldsymbol{k}}}{|(\hat{\boldsymbol{k}}\times\boldsymbol{\tau})\times\hat{\boldsymbol{k}} - \frac{C}{\mathcal{V}}(\hat{\boldsymbol{k}}\times\boldsymbol{F}_D)\times\hat{\boldsymbol{k}}|}\ , \tag{4.32a}$$

$$\hat{\boldsymbol{x}}'_p = \frac{(\hat{\boldsymbol{k}}\times\boldsymbol{\tau}) - \frac{C}{\mathcal{V}}(\hat{\boldsymbol{k}}\times\mathbf{F}_D)}{|(\hat{\boldsymbol{k}}\times\boldsymbol{\tau}) - \frac{C}{\mathcal{V}}(\hat{\boldsymbol{k}}\times\boldsymbol{F}_D)|}\ . \tag{4.32b}$$

With the help of equation (4.31), if $\hat{\boldsymbol{t}}_{\tau_b}$ is the unit vector $\boldsymbol{\tau}_b/|\boldsymbol{\tau}_b|$, equations (4.32a,b) may be written as follows:

$$\hat{\boldsymbol{x}}_{\tau_b} = \frac{(\hat{\boldsymbol{k}}\times\boldsymbol{\tau})\times\hat{\boldsymbol{k}} - \frac{C}{\mathcal{V}}(\hat{\boldsymbol{k}}\times\boldsymbol{F}_D)\times\hat{\boldsymbol{k}}}{|(\hat{\boldsymbol{k}}\times\hat{\boldsymbol{t}}_{\tau_b})\times\hat{\boldsymbol{k}}||\boldsymbol{\tau} - \frac{C}{\mathcal{V}}\boldsymbol{F}_D|}\ , \tag{4.33a}$$

$$\hat{\boldsymbol{x}}'_p = \frac{(\hat{\boldsymbol{k}}\times\boldsymbol{\tau}) - \frac{C}{\mathcal{V}}(\hat{\boldsymbol{k}}\times\mathbf{F}_D)}{|(\hat{\boldsymbol{k}}\times\hat{\boldsymbol{t}}_{\tau_b})||\boldsymbol{\tau} - \frac{C}{\mathcal{V}}\boldsymbol{F}_D|} \tag{4.33b}$$

Let us introduce the following unit vectors $\hat{\boldsymbol{t}}_\tau$ and $\hat{\boldsymbol{x}}_\tau$ which read

$$\hat{\boldsymbol{x}}_\tau = \frac{(\hat{\boldsymbol{k}}\times\boldsymbol{\tau})\times\hat{\boldsymbol{k}}}{|(\hat{\boldsymbol{k}}\times\boldsymbol{\tau})\times\hat{\boldsymbol{k}}|}\ , \qquad \hat{\boldsymbol{t}}_\tau = \frac{\boldsymbol{\tau}}{|\boldsymbol{\tau}|}\ . \tag{4.34}$$

Substituting from (4.34) into equations (4.33a,b) we find:

$$\hat{\boldsymbol{x}}_{\tau_b} = \frac{|(\hat{\boldsymbol{k}} \times \hat{\boldsymbol{t}}_\tau) \times \hat{\boldsymbol{k}}||\boldsymbol{\tau}|}{|(\hat{\boldsymbol{k}} \times \hat{\boldsymbol{t}}_{\tau_b}) \times \hat{\boldsymbol{k}}||\boldsymbol{\tau} - \frac{C}{\nu}\boldsymbol{F}_D|} \left[\hat{\boldsymbol{x}}_\tau - \frac{\frac{C}{\nu}(\hat{\boldsymbol{k}} \times \boldsymbol{F}_D) \times \hat{\boldsymbol{k}}}{|(\hat{\boldsymbol{k}} \times \hat{\boldsymbol{t}}_\tau) \times \hat{\boldsymbol{k}}||\boldsymbol{\tau}|}\right] , \tag{4.35a}$$

$$\hat{\boldsymbol{x}}'_p = \frac{\left[(\hat{\boldsymbol{k}} \times \boldsymbol{\tau}) - \frac{C}{\nu}(\hat{\boldsymbol{k}} \times \mathbf{F}_D)\right]|\boldsymbol{\tau}|}{|(\hat{\boldsymbol{k}} \times \hat{\boldsymbol{t}}_{\tau_b})||\boldsymbol{\tau} - \frac{C}{\nu}\boldsymbol{F}_D||\boldsymbol{\tau}|} . \tag{4.35b}$$

Substituting from the definitions (4.4, 4.5, 4.10, 4.11, 4.12, 4.22) into equations (4.35a,b) we find the following relationships:

$$\hat{\boldsymbol{x}}_{\tau_b} = \hat{\boldsymbol{x}}_\tau \frac{1 - \mathcal{P}\mathcal{M}}{Q} + \frac{\mathcal{P}\mathcal{R}}{Q}(-\sin\alpha\tan\varphi, \frac{1}{\cos\alpha}, 0) , \tag{4.36}$$

$$\begin{aligned} \hat{\boldsymbol{x}}'_p = \frac{1}{\mathcal{N}'} \Bigg\{ & \left[-\frac{\mathcal{P}\mathcal{R}}{\cos\alpha}\right] \ ; \\ & [\cos\alpha(1 - \mathcal{P}\mathcal{M}) - \mathcal{P}\mathcal{R}\sin\alpha\tan\varphi] \ ; \\ & 0\Bigg\} , \end{aligned} \tag{4.37}$$

where:

$$\mathcal{M} = f_p\sqrt{\tau_*} - \hat{V}_p\cos\psi \ ; \ \ \mathcal{P} = \frac{3}{4}c_D\frac{C}{D}\frac{\sqrt{\mathcal{M}^2 + \hat{V}_p^2\sin^2\psi}}{\tau_*} , \tag{4.38}$$

$$\mathcal{R} = \frac{\hat{V}_p\sin\psi}{\sqrt{1 + \tan^2\alpha + \tan^2\varphi}} , \tag{4.39}$$

$$Q = \left\{[1 - \mathcal{P}(\mathcal{M} + \mathcal{R}\sin\alpha\tan\varphi)]^2 + \left(\frac{\mathcal{P}\mathcal{R}}{\cos\alpha}\right)^2\right\}^{1/2} , \tag{4.40}$$

$$\begin{aligned} \mathcal{N} = \Big\{ & [\cos\alpha - \mathcal{P}(\mathcal{M}\cos\alpha + \mathcal{R}\sin\alpha\tan\varphi)]^2 + \\ & + [-\sin\alpha - \mathcal{P}(-\mathcal{M}\sin\alpha + \mathcal{R}\cos\alpha\tan\varphi)]^2 + \left[\frac{\mathcal{P}\mathcal{R}}{\cos\alpha}\right]^2\Big\}^{1/2} \\ \mathcal{N}' = \Bigg\{ & \left[\frac{\mathcal{P}\mathcal{R}}{\cos\alpha}\right]^2 + [\cos\alpha - \mathcal{P}(\mathcal{M}\cos\alpha + \mathcal{R}\sin\alpha\tan\varphi)]^2\Bigg\}^{1/2} . \end{aligned} \tag{4.41}$$

Finally, with the use of the relationships (4.36) and (4.37) the definitions (4.30, 4.31, 4.32a) give:

$$\tan\alpha' = \frac{1}{Q}[(1-\mathcal{PM})\sin\alpha + \mathcal{PR}\tan\varphi\cos\alpha] \,, \tag{4.42}$$

$$\tan\varphi' = \frac{1}{Q}\left[(1-\mathcal{PM})\tan\varphi\cos\alpha - \mathcal{PR}\sin\alpha\left(\frac{1}{\cos^2\alpha}+\tan^2\varphi\right)\right] \,. \tag{4.43}$$

The latter relationships allow to evaluate the angles α' and φ' as functions of $C, \alpha, \varphi, \tau_*$ and ψ We may then finally reinforce the exact generalization of Bagnold's condition. Noting that

$$|\boldsymbol{\tau}_b| = \left|\boldsymbol{\tau} - \frac{\mathcal{C}}{\mathcal{V}}F_D\right| = \mathcal{N}|\boldsymbol{\tau}| \,, \tag{4.44}$$

such generalization simply reads:

$$\tau_* = \frac{\tau_{*c}[\alpha'(\mathcal{C}), \varphi'(\mathcal{C})]}{\mathcal{N}(\mathcal{C})} \,. \tag{4.45}$$

Hence, we end up with an implicit equation for the unknown concentration C which can be solved by means of an iterative procedure. However an interesting, perhaps unexpected, difficulty arises: indeed, for given longitudinal slope and external Shields stress τ_*, it turns out that a threshold value of the lateral slope $\tan\varphi$ exists above which no solution is found. In other words such condition sets an upper limit for the lateral slope compatible with Bagnold's constraint. A simple physical explanation can be given to the latter finding, namely the existence of the above threshold condition. Such explanation is related to the vectorial nature of Bagnold's hypothesis. In fact, in the classical case of equilibrium bedload transport, the average motion is unidirectional and particle drag is aligned with the incident average fluid motion, hence the residual stress vector is obtained by subtracting two parallel vectors: under these conditions the modulus of the vector difference is equal to the difference between the moduli of the two vectors. In other words, the external stress can always be reduced to the critical value by appropriately increasing the resultant drag force, i.e. the concentration of saltating particles.

This is not the case when the bed surface is arbitrarily sloping as particle drag is no longer aligned with the external stress: as a result, we have to

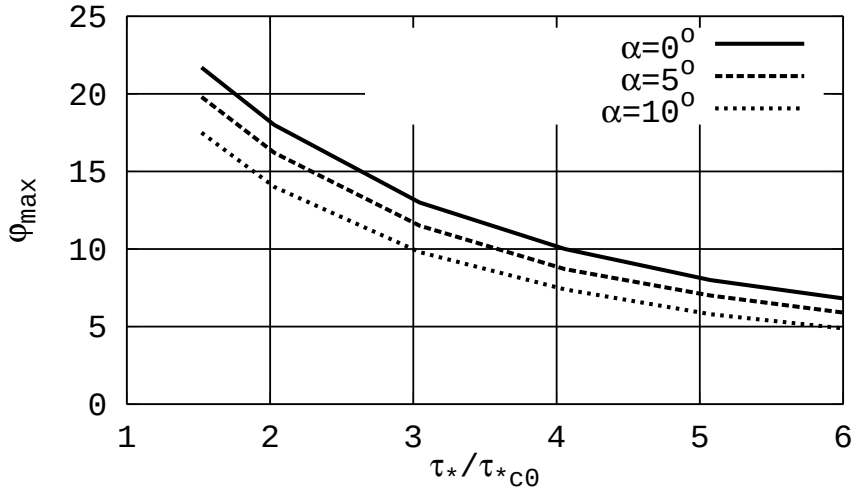

Figure 4.5: *The maximum lateral inclination of the bed surface φ_{max} for the validity of Bagnold hypothesis is plotted versus Shields stress for given values of longitudinal slope of the bed surface α ($\phi = 40°, c_D = 0.4, c_L/c_D = 1.25, \mu_d = 0.6, f_p = 11.5, \tau_{*c0} = 0.032$).*

evaluate the modulus of the difference between two vectors which form an angle β with each other. Hence, using Carnot theorem we may write:

$$\left| \boldsymbol{\tau} - \frac{C}{\mathcal{V}} \boldsymbol{F}_D \right| = \sqrt{\tau^2 + (CF_D/\mathcal{V})^2 - (2CF_D\tau/\mathcal{V})\cos\beta}\,, \qquad (4.46)$$

It is easy to show that the left hand side of equation (4.46) attains a minimum value when the areal concentration C takes the value $(\tau\mathcal{V}\cos\beta/F_D)$. It follows that, whenever such minimum exceeds the critical value of the shear stress appropriate for the longitudinal and lateral slopes of the bed associated with the residual stress, then Bagnold's constraint cannot be satisfied. In other words, no matter how large is the areal concentration C, the residual stress cannot be reduced to the critical value. Figures 4.5 and 4.6 show the dependence of $\varphi_{\max}$ and $(C/D)_{lim}$ on τ_* for given values of the longitudinal slope $\tan(\alpha)$. The results of Kovacs and Parker (1994) are also shown. Note that Kovacs and Parker's (1994) approximation appears to be fairly close to the 'exact' result, its only limit being its inability to predict the failure of Bagnold's hypothesis for sufficiently large lateral slopes. The existence of

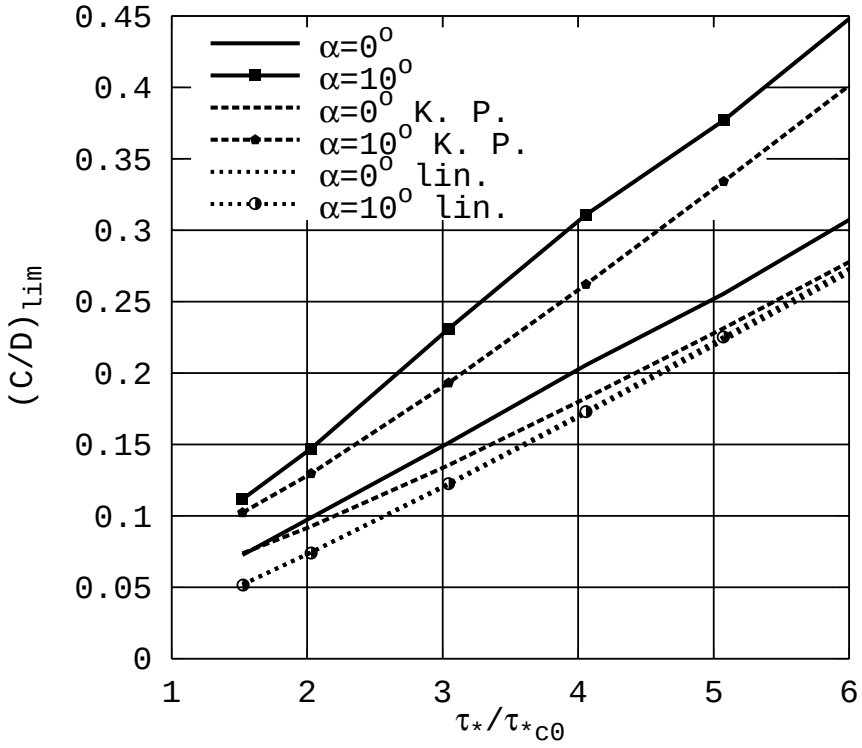

Figure 4.6: *The average areal concentration of bedload particles C scaled by particle diameter D for the limit conditions of validity of Bagnold hypothesis is plotted versus Shields stress for given value of the longitudinal inclination of the bed surface (*$\phi = 40^{\circ}, c_D = 0.4, c_L/c_D = 1.25, \mu_d = 0.6, f_p = 11.5, \tau_{*c0} = 0.032$*).*

such threshold condition poses a fairly severe and unrealistic constraint on the maximum admitted lateral slope. In fact fig. 4.5 shows that, for values of the Shields stress as low as 0.15, the maximum lateral inclination of the bed would range about 6°-7°. The ability of a stream to transport sediments as bedload under equilibrium conditions in the presence of such weakly sloping beds cannot be questioned. Hence, one is led to conclude that Bagnold's condition is not valid and must be replaced by a different condition able to account for the dynamic rather than static character of the equilibrium of the bed interface. In the next section we propose such an approach, relying on the help of the detailed experimental observations of Fernandez Luque and van Beek (1976).

4.5 An alternative approach: the excess residual stress as a measure of the entrainment capacity of the stream

If the equilibrium of the bed interface is indeed dynamic, then the excess residual stress acting on the bed interface cannot vanish. On the contrary, such stress is the most reasonable candidate to measure the residual turbulent activity present close to the interface, hence the ability of the stream to produce those turbulent events (sweeps and inward interactions) which appear to be the major hydrodynamic agents of bedload transport.

It is then instructive to reinterpret Fernandez Luque and van Beek's (1976) results, referring to uniform streams flowing on nearly horizontal planar beds, in the light of the above viewpoint. For a uniform stream flowing on a planar bed the modulus of the residual stress acting at the bed interface is readily calculated in the form:

$$\tau_b = \tau - \mu_d(\varrho_s - \varrho)gC \ . \tag{4.47}$$

Simple manipulations allow one to reduce the latter expression to the following dimensionless relationship for the excess residual Shields stress in terms of the excess external Shields stress and of the average areal concentration of saltating particles:

$$(\tau_{*b} - \tau_{*c}) = (\tau_* - \tau_{*c}) - \mu_d \frac{C}{D} \ . \tag{4.48}$$

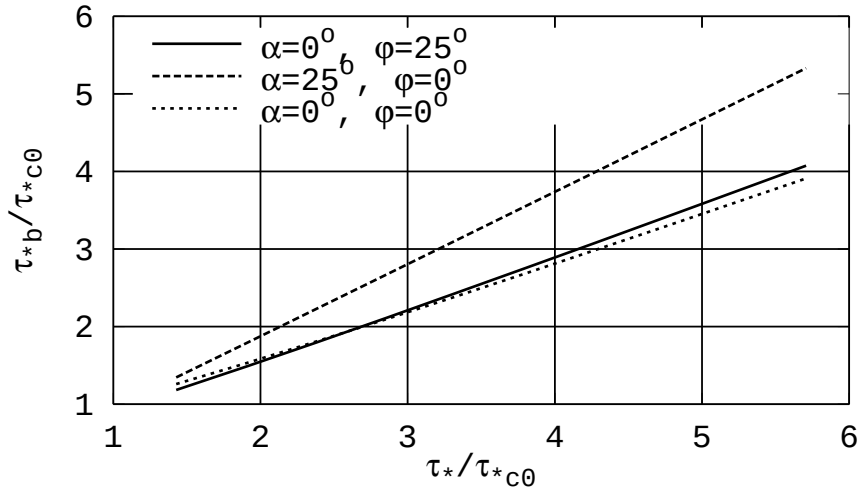

Figure 4.7: *The residual stress τ_{*b} acting on the bed interface is plotted versus the external Shields stress τ_* for given values of the angles α and φ ($\phi = 40°, c_L/c_D = 1.25$, $c_D = 0.4$, $\tau_{*c0} = 0.032$, $f_p = 11.5$, $\mu_d = 0.6$).*

The areal concentration C was estimated by Fernandez Luque and van Beek (1976). Employing their estimate allows us to test our conclusion about the failure of Bagnold's hypothesis. Following the latter authors, let us then write:

$$\frac{C}{D} = \frac{5.7}{11.5}\frac{(\tau_* - \tau_{*c})^{3/2}}{\sqrt{\tau_*} - 0.7\sqrt{\tau_{*c}}} = (\tau_* - \tau_{*c})g\left(\frac{\tau_*}{\tau_{*c}}\right) \ , \tag{4.49}$$

such relationship turns out to be very close to a linear relationship. Substituting from (4.49) into (4.48) we find:

$$(\tau_{*b} - \tau_{*c}) = (\tau_* - \tau_{*c})\left[1 - \mu_d g\left(\frac{\tau_*}{\tau_{*c}}\right)\right] \ . \tag{4.50}$$

The latter relationship is plotted in fig. 4.7 and turns out to be very close to a linear relationship. It shows that, at least within the range of values of Shields stress investigated by Fernandez Luque and van Beek (1976), Bagnold's assumption is never satisfied, a conclusion already reached by the latter authors. If equation (4.50) is replaced into (4.49) we achieve a useful goal, namely that of expressing the mean areal concentration of saltating particles in terms of the excess residual Shields stress. Such relationship, which is plotted in

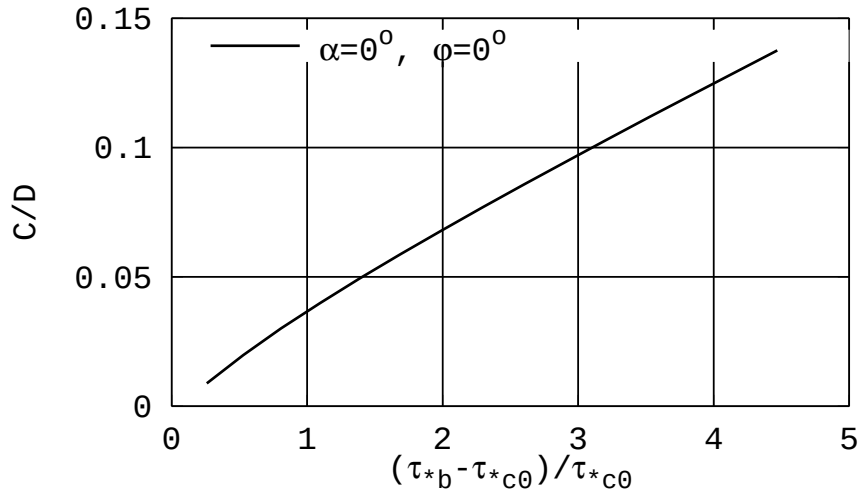

Figure 4.8: *The average areal concentration of bedload particles C scaled by particle diameter D is plotted versus the residual Shields stress* τ_{*b} *(*$\phi = 40°, c_L/c_D = 1.25$, $c_D = 0.4$, $\tau_{*c0} = 0.032$, $f_p = 11.5$, $\mu_d = 0.6$*).*

fig. 4.8, shows that the average areal concentration of saltating particles increases quasi linearly with the excess residual Shields stress, a result which is strongly suggestive of the fact that the latter quantity may indeed be taken as a measure of the entrainment capacity of the stream.

The latter argument can be set at the basis of an approach to the evaluation of bedload transport on arbitrarily sloping beds which does no longer need rely on Bagnold's assumption. The basic idea is simply to assume that the average areal concentration of saltating particles is an increasing function of the excess residual Shields stress, the latter quantity being taken as the appropriate measure of the residual turbulent activity at the bed interface. Needless to say, on a sloping bed the excess residual Shields stress will have to be evaluated by employing the vectorial formulation and the critical Shields stress will have to be evaluated in terms of the local values of the longitudinal and lateral slopes, as discussed in the previous sections. The structure of the above function is not known a priori. However it seems reasonable to assume that, if the entrainment capacity of the stream and the average areal concentration depend on the excess residual Shields stress, the structure of the relationship between the latter quantities is somehow universal, i.e. it does not depend on

the macroscopic features of the bottom configuration but only on the appropriately calculated values of the local quantities. As a first guess it seems also reasonable that, in the range of low Shields stress, we employ the quasi linear relationship between C and $(\tau_{*b} - \tau_{*c})$ determined from the experimental results of Fernandez Luque and van Beek (1976).

The general procedure to determine the intensity and direction of bedload transport on an arbitrarily sloping bed can then be summarized as follows.

Let the local values of the longitudinal and lateral slopes be assigned along with the intensity and direction of the external stress acting at the top of the saltating layer. From equation (4.18) we can immediately calculate the local value of the critical Shields stress. The relationship (4.21), with the help of (4.22-4.26), then allows to calculate intensity and direction of particle velocity. Next we proceed to evaluate the residual stress and the average areal concentration of saltating particles. This requires an iterative procedure: indeed equation (4.28) allows us to calculate the residual stress vector once we know the concentration. As a first guess we may employ the relationship (4.50) to have a first estimate of $(\tau_{*b} - \tau_{*c})$ in terms of the assigned value of $(\tau_* - \tau_{*c})$. We can then employ fig. 4.8 to obtain a first estimate for C. We then go back to equation (4.28) to obtain a second approximation for $(\tau_{*b} - \tau_{*c})$ using the preliminary estimate for C. With the latter updated value of $(\tau_{*b} - \tau_{*c})$ we may return to fig. 4.8 to derive a second approximation for C, and so on till convergence is achieved. The latter procedure is indeed found to be convergent. Having determined both $\hat{\boldsymbol{V}}_p$ and C we finally evaluate the bedload transport vector per unit width $\boldsymbol{q}$ in the classical dimensionless form obtained using Einstein's scale, as follows:

$$\hat{\boldsymbol{q}} = \frac{\boldsymbol{q}}{\sqrt{(s-1)gD^3}} = \frac{C}{D}\hat{V}_p \left(\cos\psi \frac{\boldsymbol{\tau}}{|\boldsymbol{\tau}|} + \sin\psi \left(\hat{\boldsymbol{n}} \times \frac{\boldsymbol{\tau}}{|\boldsymbol{\tau}|} \right) \right) . \qquad (4.51)$$

Finally it is instructive to analyze the dependence of the modulus of $\hat{\boldsymbol{q}}$ on the external Shields stress for different values of the longitudinal and lateral inclination angles and compare such dependence with the linear relationships to which our analysis reduces when the latter angles are sufficiently small.

Let us then derive the linear relationships as a particular case of our general approach. To this aim we assume that α, φ and ψ are small such that we may write:

$$(\sin\alpha, \sin\varphi, \sin\psi) \simeq (\tan\alpha, \tan\varphi, \tan\psi) \; ; \cos\alpha \simeq \cos\varphi \simeq \cos\psi \simeq 1 \; . \qquad (4.52)$$

Using the latter approximations, the equations (4.24, 4.25, 4.26) readily lead to the following linear dependence between $\tan(\psi)$ and $\tan(\varphi)$:

$$\tan\psi = \frac{r_t}{\sqrt{\tau_*}} \tan\varphi \,, \tag{4.53}$$

where the constant r_t reads:

$$r_t = \frac{1}{f_p}\sqrt{\frac{4}{3c_D\mu_d}} \,. \tag{4.54}$$

From (4.23) and (4.53) one readily derives a relationship for the dimensionless intensity of particle velocity of a form identical to that suggested by Fernandez Luque and van Beek on the basis of their experimental observations, namely:

$$\hat{V}_p = f_p(\sqrt{\tau_*} - \sqrt{\tau_{*c1}}) \,, \tag{4.55}$$

where τ_{*c1} is a dynamical form of the critical Shields stress which reads:

$$\tau_{*c1} = \frac{4}{3}\frac{\mu_d}{c_D f_p^2} \,. \tag{4.56}$$

The reader will note that, in the limit of gently sloping beds, the intensity of particle velocity is not affected by the sloping character of the bed.

Using the approximations (4.52), one readily shows that, at the leading order of approximation, the residual stress vector is aligned with the external stress vector, hence the relationship for the average areal concentration of saltating particles reduces to the quasi-linear relationship (4.49) of Fernandez Luque and van Beek (1976).

Hence, the linearized form of the bedload transport formula is found to read:

$$\frac{\boldsymbol{q}}{\sqrt{(s-1)gD^3}} = \frac{C}{D}\hat{V}_p\left[\frac{\boldsymbol{\tau}}{|\boldsymbol{\tau}|} + \frac{r_t}{\sqrt{\tau_*}}\tan\varphi\left(\hat{\boldsymbol{n}}\times\frac{\boldsymbol{\tau}}{|\boldsymbol{\tau}|}\right)\right] \,, \tag{4.57}$$

with $C, \hat{V}_p$ and ψ given by equations (4.49), (4.55) and (4.53) respectively. We may now compare the results of the fully non linear approach proposed herein with the linearized treatment just described. Such comparison is reported in fig. 4.9 which shows that, as expected, on sloping beds the intensity of bedload transport increases with the external stress faster than on horizontal beds, the more so as the longitudinal and lateral slope increase. Also note

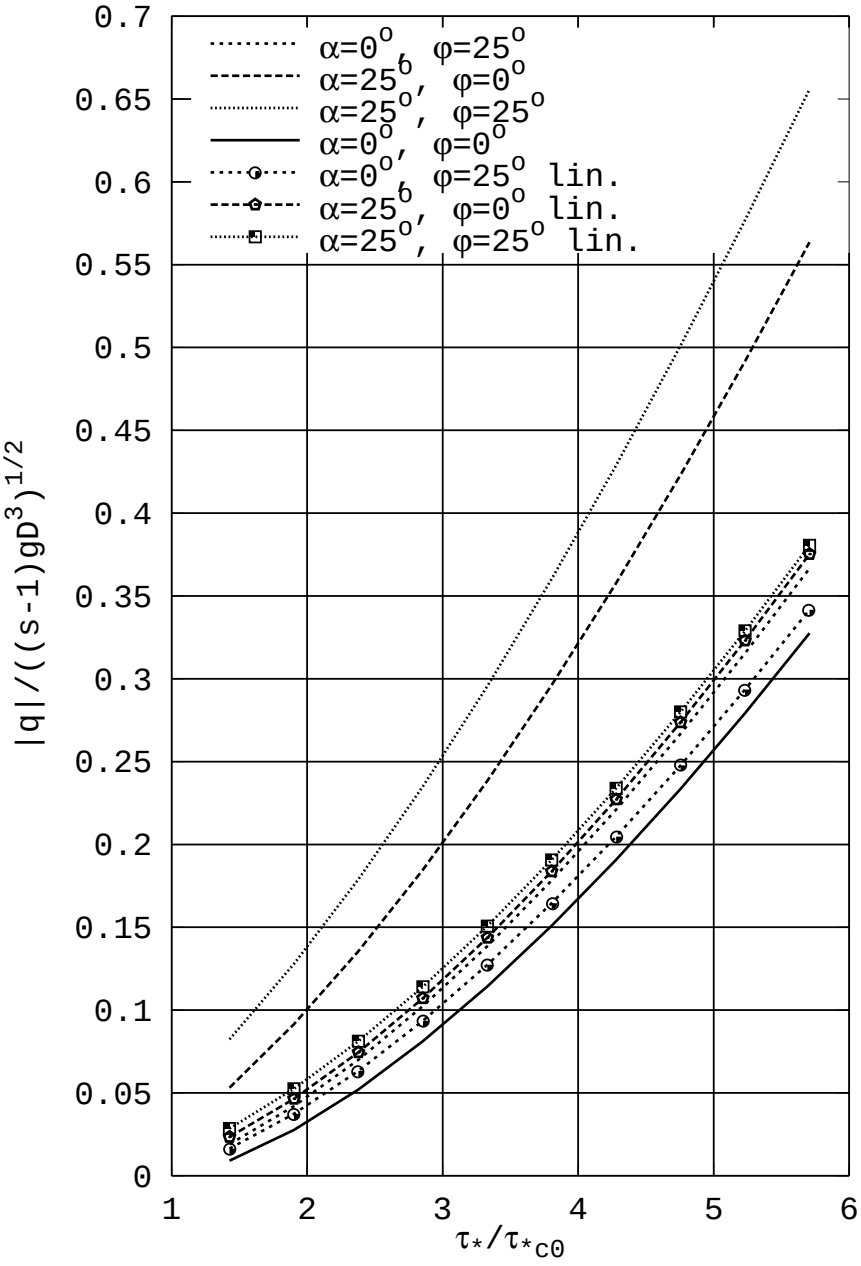

Figure 4.9: *The modulus of the bedload transport vector is plotted versus the external Shields stress for given values of the longitudinal and lateral inclination angles and compared with the results of the linearized formulation* ($\phi = 40°, c_L/c_D = 1.25, c_D = 0.4, \tau_{*c0} = 0.032, f_p = 11.5, \mu_d = 0.6$).

that the vectorial nature of the relationship which gives the residual stress vector (equation 4.28) implies that, for given external stress, the modulus of the residual stress increases as the lateral bedslope increases, leading to increasing values of the bedload transport rate, as expected on physical ground.

4.6 Discussion and conclusions

The main conclusion of the present paper is an attempt to provide a conclusive answer to the longdated debate on the validity of Bagnolds hypothesis concerning the residual stress acting on the bed interface when bedload particles are set in a saltating motion under equilibrium conditions at low Shields stress. Essentially, we have shown that, if the bed interface is sloping rather than horizontal, for relatively small lateral slopes the applied external stress cannot be reduced to the critical value no matter how large is the concentration of saltating particles. In physical terms, one can state that on a sufficiently sloping bed it is the downslope component of gravity which supports particle motion which, then, needs to drain less momentum from the fluid phase.

Hence, one is led to the conclusion that Bagnold's hypothesis is an unnecessarily severe constraint. On the other hand, our reinterpretation of Fernandez Luque and van Beek's (1976) results (see equation (4.50) and fig. 4.7), confirms that the residual stress in the experiments of the above authors was invariably smaller than the available applied external stress. A similar, though not identical, conclusion was reached by Fernandez Luque and van Beek (1976, sect. 3.5). The latter authors calculated the reduction in fluid shear stress due to the bed load by evaluating the average transfer of momentum by the particle to the bed surface, a calculation which relied on an estimate of the average time required for a particle to cover the average saltation length. Such length was taken by the above authors as a constant multiple of particle diameter. On the contrary, measurements of Niño et al. (1994) suggest that the saltation length increases linearly with the excess applied stress. We now show that the estimate of the reduction of fluid shear stress given by Fernandez Luque and van Beek (1976) contradicts the results obtained by the same authors for the dependence of the average particle speed on the excess external stress. In fact, if the reduction of fluid stress is calculated using equation (11) of Fernandez Luque and van Beek (1976) and substituted into the right hand side of our equation (4.19), one readily derives the following relationship for

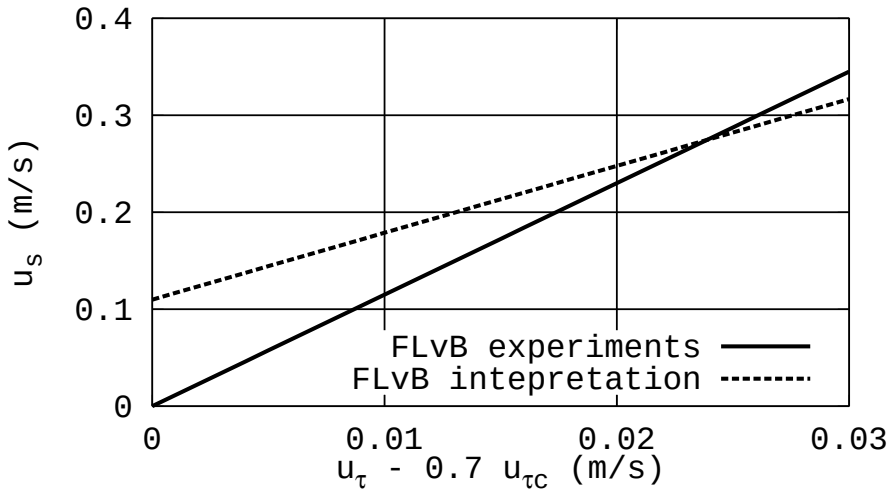

Figure 4.10: *Average particle velocity as from the experiments and the interpretation of Fernandez Luque & van Beque (1976). (*$\phi = 40°, c_D = 0.4, c_L/c_D = 1.25, \tau_{*c0} = 0.032, \mu_d = 0.6, D = 1mm$*).*

the average particle speed:

$$\hat{V_p} = \Omega f_p \sqrt{\tau_*} \,, \tag{4.58}$$

where Ω is the following parameter:

$$\Omega = \frac{1}{1 + 0.238 \frac{(s+c_M)^{1/2}}{\sqrt{c_D}}} \,, \tag{4.59}$$

having denoted by c_M the added mass coefficient for a sphere ($c_M = 0.5$). The relationship (4.58) is compared in figure 10 with that proposed by Fernandez Luque and van Beek (1976) as appropriate to interpret their experimental observations for the average particle speed. The discrepance between the two relationships can be easily removed provided the average saltation length is allowed to depend linearly on the excess applied stress.

Various limitations of the present model need be mentioned.

Firstly, the evaluation of the average particle speed relies on an average dynamic balance which neglects the integrated effect of turbulent fluctuations, added mass effects and shear induced horizontal buoyancy. Moreover, the

evaluation of the average drag force acting on particles employs a distribution of fluid speed which is assumed to be unaffected by the presence of particles. Improvements in this respect can be made by resorting to saltation models of the kind employed by Wiberg and Smith (1985), Sekine and Parker (1992) or Niño and García (1994). However, note that all these models need employ some empirical assumption concerning the interaction of saltating particles with the immobile bed (a hydrodynamical rebound rather than a collision).

Moreover, as the Shields stress increases, the concentration of saltating particles also increases, which leads to enhancing the effect of particle interactions, both hydrodynamical and possibly collisional, a shortcoming present in virtually all the theoretical models of bedload transport formulated so far.

While such limitations are likely to become crucial at fairly large Shields stresses, one may reasonably expect that they do not invalidate the basic argument of the present contribution at the relatively small values of the Shields stress considered herein.

Finally, the assumption that a linear relationship exists between the concentration of saltating particles and the excess residual stress will definitely require further substantiation. Hence, the refined experimental observations which have been made possible by the latest technological developments are definitely called for. At the present stage, however, it appears that the theoretical framework built on the basis of the above assumption, besides being based on the accurate observations of Fernandez Luque and van Beek (1976), has allowed us to remove in a consistent fashion the contradictions arising from the use of Bagnold's hypothesis.

References

Auton, T.R., The lift force on a spherical body in a rotational flow, *J. Fluid. Mech.*, 183, 199 - 218, 1987.

Auton, T.R., Hunt, J.C.R. & Prud'homme, M., The force exerted on a body in inviscid unsteady non-uniform rotational flow, *J. Fluid Mech.*, 197, 241-257, 1988.

Chepil, W.S., The Use of Evenly Spaced Hemispheres to Evaluate Aerodynamic Forces on a Soil Surface, *Transactions, American Geophysical Union*, 39, No. 3, 1958.

Ashida, K. & Michiue, M., Study on hydraulic resistance and bedload transport rate in alluvial streams, *Transactions, Japan Society of Civil Engineering*, 206, 59-69, 1972.

Bagnold, R. A., The flow of cohesionless grains in fluids *Philos. Trans. R. Soc. London A*, 249, 235-297, 1956.

Drake, T.G., Shreve, R.L., Dietrich, W.E., Whiting, P.J. & Leopold, L.B., Bedload transport of fine gravel observed by motion picture photography, *J. Fluid. Mech.*, 192, 193-217, 1988.

Engelund, F. & Fredsøe, J., A sediment transport model for straight alluvial channels, *Nordic Hydrology*, 7, 293-306, 1976.

Fernandez Luque, R. & van Beek, R., Erosion and transport of bed sediment, *J. of Hydraulic Research*, 14(2), 127-144, 1976.

Heathershaw, A.D. & Thorne, P.D., Sea-bed noises reveal role of turbulent bursting phenomenon in sediment transport by tidal currents, *Nature*, 316, 339-432, 1985.

Ikeda, S., Incipient motion of sand particles on side slopes, *Hydraul. Div. Am. Soc. Civ. Eng.*, 108(HY1), 95-114, 1982.

Kovacs, P. & Parker, G., A new vectorial bedload formulation and its application to the time evolution of straight river channels, J. Fluid Mech., 267, 153-183, 1994.

Nelson, J.J., Alving, A.E. & Joseph, D.D., Boundary layer flow of air over water on a flat plate, *J. Fluid. Mech.*, 284, 159 - 169, 1995.

Niño, Y., García, R. & Ayala L., Gravel saltation 1. Experiments, *Water Res. Res.*, 30(6), 1907-1914, 1994.

Niño, Y. & García, R., Gravel saltation 2. Modeling, *Water Res. Res.*, 30(6), 1915-1924, 1994.

Parker, G. & Andrews E.D., Sorting of bed load sediment by flow in meander bends, *Wat. Res. Res.*, 21(9), 1361-1373, 1985.

Sekine, M. & Kikkawa, M., Mechanics of saltating grains. II, *J. Hydr. Eng.*, 118(4), 536-558, 1992.

Sekine, M. & Parker, G., Bed-load transport on transverse slope. I, *J. Hydr. Eng.*, 118(4), 513-535, 1992.

Thorne, P.D., Williams, J.J. & Heathershaw, A.D., In situ acoustic measurements of marine gravel threshold and transport, *Sedimentology*, 36, 61-74, 1989.

Wiberg, P. L. & Smith, J. D., A theoretical model for saltating grains in water Mechanics of saltating grains. II, *J. Geophys. Res.*, 90(C4), 7341-7354, 1985.

Ringraziamenti

Ringrazio il *Maestro* Giovanni Seminara che mi ha costantemente seguito durante il corso di dottorato con passione ed entusiasmo. Lo ringrazio anche per avermi trasmesso un po' del suo 'fuoco'.

Sono grato al prof. Giampaolo Di Silvio per aver acconsentito a leggere questo lavoro e per gli interessanti spunti di riflessione fornitimi.

Ringrazio tutti gli studiosi che in questi anni mi hanno messo a parte della loro esperienza e conoscenza, in particolare Peter Ashmore, Marco Colombini, Stefano Lanzoni, Chris Paola, Gary Parker e Marco Tubino.

Esprimo la mia gratitudine a tutto il personale del Dipartimento di Ingegneria Ambientale dell'Università di Genova per avermi aiutato nello sviluppo di questo lavoro, in particolare: Tina D'Agostino, Rosella Bracco, Marco Galiani, Maria Incerti, Angela Ioppolo, Domenico Mazzeo, Franco Porcile, Gianni Ruà e Luigi Stagi.

Un particolare grazie a Bianca, Alessandro, Michele, Miki e Nunzio per il loro aiuto e la disponibilità dimostratami.

Ringrazio Maria Paganelli, Nicoletta Tambroni e Caterina Zucca per la collaborazione offertami durante l'attività sperimentale.

Un ringraziamento speciale a Veronica, Guido e Rodolfo con i quali ho condiviso il periodo del dottorato. Grazie anche a loro questi anni sono trascorsi in un'atmosfera piacevole.

Sono molto grato a Giulio per il suo aiuto informatico.

Desidero infine ringraziare il Dipartimento di Ingegneria Civile dell'Università di Firenze ed in particolare i proff. Ignazio Becchi e Enio Paris per avermi

permesso di svolgere gli ultimi mesi del corso di dottorato presso l'Università di Genova.